# Probing stellar wind properties in Cygnus X-1 through X-ray variability


Eleonora Veronica Lai

under the supervision of:

**Dr. hab. Barbara De Marco**


A thesis submitted in fulfilment of the requirements
for the degree of Doctor of Philosophy



**Nicolaus Copernicus Astronomical Center**
**of the Polish Academy of Science**

*To the Marias of my life*

# Acknowledgments

During these years, I met a lot of people who enriched my path making my journey less difficult. Thanks for entrusting me a piece of your hearts.

Firstly, I would like to sincerely thank my supervisor Dr. Barbara De Marco for helping me become the scientist I am today. Without her knowledge and guidance, I could have not managed to get to this point in my carrier.

I would like to thank all scientists at CAMK and, in particular, a few of them. Thank you, Agata, for being there in particular in the last part of my stay in Poland, comforting me and giving me a smile when I needed it the most.
Andrzej, thank you for your help, for the science you taught me and for the time spent together in different conferences with Antonii too.
Thanks, Alex and Piotr, for the precious advices you offered me.

Thanks to all the staff at CAMK, for always comforting me, helping me, and understanding me. In particular thanks to Barbara, Kasia, Dominika, Anna, Jadwiga, Dorota, Piotr and Tomek. Thank you for always smiling at me and telling me that my Polish was good.

Thanks to my advisors at OAC INAF, Matteo and Maura, who always encouraged me in finishing my studies and gave me the time to do so.

A special thanks to Marco, Lorenzo, Ola, André, Amedeo, Riano, Sylwia, Giovanni, Matteo, Ruchi, Saikruba, Dominik, Deepika, Maitrayee, Biswaraj, Parikshit, Thatagata, Alex, Samaresh, Jonas, Marius, Ola, Quentin, Miriam, Jamerson, Nicolas, Ayush, Tilak, Tom, Hilal, Ganesh, Ngan. Thank you for accepting me as your friend and for always being there to listen to me.

To all my friends from Sardinia, and in particular, Marco, Mauro, Alelai and Davide for always asking and listening to my stories from Poland. Special thanks to Ilaria, Monica and Valeria for always encouraging me in these years. Thank

you for being with me despite the distance. Thank you to Franco and Alessandro who have always been present since day one.

To the love of my life, my husband Matteo. We lived this challenge together, and we managed to be each other's strength during a pandemic and a war next door. Without you, I could not survive this experience. Thank you for always believing in me and making me stronger. Thank you for encouraging me and always staying by my side. You are my other half. I love you.

Thanks to my mother Lisel Maria, my other supervisor. The emotions I could not manage to stop, you filtered them out. You made me calm when I was angry, you encouraged me when I had no hope, and you brought me back when I got lost.

Thanks to my father Luigi, my first fan. You made me laugh although I was crying 2000 km away from you. You supported me, understood me as nobody else did.

Thanks to my brother Gian Luca, my personal coach. Leaving you in Sardinia was one of the most difficult things to do in my life, but your "when are you coming back?" made me feel less distant.

To Patricia, Bruno, Vanessa, Giorgio, Monia, Simone, Elena and Giovanni. Thank you for always supporting me whenever I had a bad time and listening to my stories every time. You were the ones sharing the weight of my heavy luggage.

To conclude, I would like to thank Vania and my other cousins, my aunts and uncles who were present in the toughest times, and my grandmother Nina who listened to me every time I came back to Sardinia.
Thanks to my grandparents Luigi, Attilio and Maria who left this life before I could finish this journey but always believed in me and loved me.

Nonna, indeed Poland was "a illargu meda" but I managed to come back.

Grazie.

# Abstract

The project described in this thesis focuses on the study of the stellar wind X-ray variability in the high mass X-ray binary system Cygnus X-1. The Cygnus X-1 system hosts a stellar-mass black hole ($\sim 21 M_{\odot}$) persistently accreting from a blue supergiant companion star, HDE 226868, via a strong stellar wind. Stellar winds are highly perturbed and inhomogeneous large scale structures, characterised by the formation of overdense regions or clumps. Clumps crossing our line-of-sight to the X-ray source cause absorption dips in the X-ray light curves. This effect is strongest at superior conjunction, when the companion star lies between the observer and the X-ray source. As a consequence, the X-ray spectral-timing properties of Cygnus X-1 are expected to be highly affected by the stellar wind. Moreover, the observed spectral variability is a diagnostic of the intrinsic physical properties of the structured stellar wind. Due to the intermediate orbital inclination ($i \sim 27°$) of the Cygnus X-1 binary system, X-ray variability induced by the stellar wind can be more easily probed, as the line-of-sight to the X-ray source crosses deep layers of the wind, reaching close to the companion's star photosphere. Therefore, Cygnus X-1 is one of the best laboratories to investigate such winds.

In our first work, we performed a X-ray spectral-timing analysis of the CHOCBOX XMM-Newton campaign, a long monitoring covering about one and a half orbits of the system during its hard spectral state. The unprecedented monitoring caught two consecutive passages at superior conjunction. We found that the presence of the stellar wind strongly modifies the observed variability power spectral density of the X-ray source, within all the probed energy ranges ($0.3 - 10\,\mathrm{keV}$). In particular, the low-frequency ($\lesssim 1$ Hz, corresponding to timescales longer than 1 s) variability power is enhanced. We ascribe this enhancement to variability of the column density of the stellar wind, caused by the passage of clumps along the line-of-sight. Assuming a terminal velocity of $v_{\infty} = 2400\,\mathrm{km\,s^{-1}}$ of the stellar wind, we were able to estimate the characteristic radial size of the clumps to be $l \sim 0.5$–$1.5 \times 10^{-4} R_{*}$. Given the very short timescales probed with our analysis, this should represent an estimate of the size of the smallest clumps.

At higher frequencies ($\gtrsim 1$ Hz, i.e. timescales shorter than 1 s) the wind tends to suppress the otherwise high variability power of the X-ray source. We interpret

this suppression as due to large scale scattering of the emitted X-ray photons, which smears out the intrinsic fast variability of the X-ray source. The data suggest this scattering to occur in a medium optically thicker than the wind ($\tau \sim 0.5 - 1$), possibly an accretion bulge formed at the impact zone of the stellar wind with the outer edge of the accretion disc. Finally, we found that non-linear variability of the absorbing gas causes a decrease of coherence between soft and hard band light curves. In addition, a long low frequency soft lag was observed during the first passage at superior conjunction. Both these features likely represent the spectral-timing signatures of reprocessing/recombination within the wind.

In our second work, we focused on the first and most absorbed observation of the CHOCBOX campaign, covering the first passage at superior conjunction. Our aim was to analyse the short timescale spectral variability of the stellar wind and constrain its physical properties. We made use of colour-colour diagrams in order to analyse the time-resolved spectral behaviour of the source. We fitted the colour-colour diagrams with different models, modelling the wind as a partial covering gas, and testing different ionisation levels. We found that the best-fit model requires the wind to be stratified, with its ionisation parameter, $\log \xi$, decreasing as its column density, $N_{\rm H,w}$, increases. In particular, this kind of models can better reproduce the characteristic "nose-like" or "pointy" shape of the colour-colour tracks in the hard state. We thus investigated the temporal evolution of the colour-colour track around superior conjunction, by performing time-resolved fits of the diagram, over orbital phase steps of 0.024. Our fits indicate that the colour-colour diagram shape changes because of concurrent variations of the column density and covering factor of the stellar wind. We found evidence of a one-to-one correlation between the long term ($\gtrsim 11\,\mathrm{ks}$) and the rapid (10 s–11 ks) variations of the column density of the wind, which could have implications on how the clumps combine to form bigger structures. We finally compared our results to the predictions from the clumpy stellar wind model proposed by El Mellah et al. (2020). This resulted in an estimate of the wind mass loss rate of $\dot{M}_* \sim 7 \times 10^{-6}\ \mathrm{M_\odot\,yr^{-1}}$, and of the mass of a typical clump of $m_{cl} \sim 10^{17}\,\mathrm{g}$.

# Streszczenie

Projekt opisany w tej rozprawie skupia się na badaniu zmienności rentgenowskiej wiatru gwiazdowego w masywnym układzie podwójnym Cygnus X-1. Układ Cygnus X-1 zawiera masywną czarną dziurę pochodzenia gwiazdowego ($\sim 21\mathrm{M}_{\odot}$) stale akreującą materie ze swojego towarzysza, niebieskiego nadolbrzyma HDE 226868 poprzez wiatr gwiazdowy. Wiatry gwiazdowe to silnie zaburzone i niejednorodne struktury wielkoskalowe, tworzące charakterystyczne, nadmiernie gęste regiony i skupiska materii. Jeśli skupiska te przecinając naszą linię widzenia do źródła promieniowania rentgenowskiego, powodują absorpcyjne wgłębienia w krzywych blasku promieniowania rentgenowskiego. Efekt ten jest najsilniejszy w koniunkcji górnej, gdy towarzysząca gwiazda znajduje się między obserwatorem, a źródłem promieniowania rentgenowskiego. W konsekwencji oczekuje się, że wiatr gwiazdowy będzie silnie wpływał na właściwości widma rentgenowskiego Cygnusa X-1 w czasie. Ponadto obserwowana zmienność widma jest diagnostyką wewnętrznych właściwości fizycznych ustrukturyzowanego wiatru gwiazdowego. Ze względu na średnie nachylenie orbity ($i \sim 27^{\circ}$) układu podwójnego Cygnus X-1, zmienność rentgenowska wywołana przez wiatr gwiazdowy może być łatwiej zbadana, ponieważ linia widzenia źródła promieniowania rentgenowskiego przecina głębokie warstwy wiatru, docierające blisko fotosfery gwiazdy towarzyszącej. Dlatego Cygnus X-1 jest jednym z najlepszych laboratoriów do badania tego typu wiatrów.

W naszej pierwszej pracy przeprowadziliśmy analizę zmienności widma promieniowania X z długiego monitoringu kampanii obserwacyjnej CHOCBOX XMM-Newton, obejmującego około półtora orbity układu w twardym zakresie widma rentgenowskiego. Bezprecedensowy monitoring uchwycił dwa kolejne przejścia w koniunkcji górnej. Odkryliśmy, że obecność wiatru gwiazdowego silnie wpływa na obserwowaną zmienność gęstości widmowej mocy źródła promieni X, we wszystkich badanych zakresach energii (0.3–10 keV). W szczególności, moc zmienności w niskiej częstotliwości ($\lesssim 1$ Hz, odpowiadająca skalom czasowym dłuższym niż 1 s) jest zwiększona. Przypisujemy tę obserwację zmianie gęstości kolumnowej wiatru gwiazdowego, spowodowanej przejściem skupisk wzdłuż linii widzenia. Przyjmując prędkość końcową wiatru gwiazdowego równą $v_{\infty} = 2400\,\mathrm{km\,s^{-1}}$, byliśmy w stanie oszacować charakterystyczny rozmiar radialny skupisk na $l \sim 0.5$–$1.5 \times 10^{-4} R_{*}$.

Biorąc pod uwagę bardzo krótkie skale czasowe uwzględnione naszej analizie, powinno to odpowiadać rozmiarowi najmniejszych skupisk.

Przy wyższych częstotliwościach ($\gtrsim$ 1 Hz, tj. skalach czasowych krótszych niż 1 s) wiatr ma tendencję do tłumienia mocy zmienności źródła promieniowania rentgenowskiego (wysokiej w innych przypadkach). Tłumienie to interpretujemy jako spowodowane rozpraszaniem na dużą skalę emitowanych fotonów promieniowania rentgenowskiego, co rozmywa szybką wewnętrzną zmienność źródła. Dane sugerują, że rozpraszanie to występuje w ośrodku optycznie grubszym niż wiatr ($\tau \sim 0.5$–1), prawdopodobnie w wybrzuszeniu akrecyjnym utworzonym w strefie oddziaływania wiatru gwiazdowego z zewnętrzną krawędzią dysku akrecyjnego. W końcu zauważyliśmy, że nieliniowa zmienność absorbującego gazu powoduje zmniejszenie spójności pomiędzy krzywymi blasku w paśmie promieniowania rentgenowskiego miękkiego i twardego. Ponadto zaobserwowaliśmy długie, opóźnienie w niskiej częstotliwości dla pasma miękkiego podczas pierwszego przejścia w koniunkcji górnej. Obie te cechy zmiany widma prawdopodobnie świadczą o rekombinacji w obrębie wiatru.

W naszej drugiej pracy skupiliśmy się na pierwszej obserwacji kampanii obserwacyjnej CHOCBOX obejmującej pierwsze przejście w koniunkcji górnej z największą absorbcją. Naszym celem była analiza krótkoterminowej zmienności widmowej wiatru gwiazdowego i określenie jego właściwości fizycznych. Wykorzystaliśmy tzw. diagramy kolor-kolor (z ang. color-color), aby przeanalizować zachowanie widmowe źródła w odstępach czasowych. Dopasowaliśmy diagramy kolor-kolor różnymi modelami, modelując wiatr jako częściowo pokrywający gaz i testując różne poziomy jonizacji. Odkryliśmy, że najlepszym dopasowaniem jest model wymagający, aby wiatr był rozwarstwiony, a jego parametr jonizacji $\log \xi$, zmniejszał się wraz ze wzrostem gęstości kolumnowej, $N_{\mathrm{H,w}}$. Tego rodzaju modele mogą lepiej odtworzyć charakterystyczny „nosowaty" lub „spiczasty" kształt ścieżki na diagramie kolor-kolor w stanie rentgenowskim twardym. Zbadaliśmy zatem ewolucję czasową ścieżki kolor-kolor wokół koniunkcji górnej, wykonując dopasowania diagramu z rozdzielczością czasową w krokach fazy orbitalnej wynoszących 0,024. Nasze dopasowania wskazują, że kształt diagramu kolor-kolor zmienia się z powodu równoczesnych zmian gęstości kolumnowej i współczynnika pokrycia wiatru gwiazdowego. Znaleźliśmy dowody na korelację jeden do jednego między długoterminowymi ($\gtrsim$ 11 ks) a szybkimi (10 s–11 ks) zmianami gęstości kolumnowej wiatru, co może mieć implikacje dla sposobu, w jaki skupiska łączą się, tworząc większe struktury. Na koniec porównaliśmy nasze wyniki z przewidywaniami z modelu skupionego wiatru gwiazdowego zaproponowanego przez El Mellah et al. (2020). Doprowadziło to do oszacowania tempa utraty masy w wiatrze $\dot{M}_* \sim 7 \times 10^{-6}$ $\mathrm{M}_\odot\,\mathrm{yr}^{-1}$, i masy typowego skupiska $m_{cl} \sim 10^{17}$ g.

# Contents

# List of Acronyms

| | |
|---|---|
| **BH** | Black Hole |
| **GR** | General Relativity |
| **ISCO** | Innermost Stable Circular Orbit |
| **NS** | Neutron Star |
| **XRB** | X-Ray Binary |
| **WD** | White Dwarf |
| **LMXB** | Low Mass X-ray Binary |
| **HMXB** | High Mass X-ray Binary |
| **BHXRB** | Black Hole X-ray Binary |
| **HID** | Hardness-Intensity Diagram |
| **QPO** | Quasi Periodic Oscillation |
| **PSD** | Power Spectrum |
| **rms** | root mean square |
| **HRD** | Hardness-rms Diagram |
| **LOS** | line-of-sight |
| **CHOCBOX** | Cyg X-1 Hard state Observations of a Complete Binary Orbit in X-rays |
| **XMM** | X-ray Multi-Mirror Mission |
| **ESA** | European Space Agency |

| | |
|---|---|
| **RGS** | Reflection Grating Spectrometers |
| **EPIC** | European Photon Imaging Cameras |
| **MOS** | Metal Oxide Semi-conductor |
| **OM** | Optical/UV Monitor |
| **FOV** | Field Of View |
| **FWHM** | Full-Width Half Maximum |
| **CCD** | Charge-Coupled Devices |
| **DFT** | Discrete Fourier Transform |
| **SAS** | Science Analysis Software |
| **CCF** | Current Calibration Files |
| **GTI** | Good Time Interval |
| **ARF** | Ancillary Response Files |
| **RMF** | Redistribution Matrix Files |
| **CTE** | Charge Transfer Efficiency |
| **NWA** | No Wind Absorption |
| **RDPHA** | Rate Dependent PHA |
| **ODF** | Observation Data Files |
| **PDCTI** | Rate Dependent CTI |
| **ISM** | Interstellar medium |
| **PDF** | Probability Density Function |
| **KDE** | Kernel Density Estimation |

# List of Figures

# List of Tables

# Chapter 1

# Introduction

## 1.1 Black holes

Black Holes (BH) are among the most intriguing objects in the Universe. They were first hypothesised in 1783 by the English philosopher and clergyman John Michel. In his essay he suggested that for a star of the same density as the Sun or higher, but with a diameter 500 times bigger, the gravitational attraction would be so strong and the escape velocity so high that the emitted light would be forced to return to the star (Michell, 1784). Few years later, the French astronomer, mathematician and physicist Pierre-Simon Laplace inferred that the light emitted from a star with the density of the Earth and a diameter 250000 bigger than the Sun would never reach the observer due to the extreme gravitational force, thus making it effectively invisible to us (Laplace, 1799). In the last century, the German-born physicist, Albert Einstein, turned the gravitational force into a geometrical property of the space-time with the introduction of General Relativity (GR, Einstein 1916). According to Einstein's theory, photons travelling close to a massive body would change their trajectory following the curvature of the space-time induced by that body. The more massive the body, the largest the curvature of the space-time around it. In 1916, the German mathematician and astrophysicist Karl Schwarzschild solved Einstein's GR equations for a non-rotating, uncharged, spherical distribution of mass (Schwarzschild, 1916). His solution predicted the existence of a boundary surface, the so-called "event horizon", within which the curvature of space-time is so high that the escape velocity exceeds the speed of light. As a consequence, no information can be transferred to an external observer from beyond the event horizon as not even light can escape the strong gravitational field. A BH is defined as an object so compact that its entire mass is contained within its event horizon.

In the Schwarzschild's solution the event horizon is defined as:

$$R_S = \frac{2GM}{c^2} \tag{1.1}$$

also called the Schwarzschild's radius, where G is the gravitational constant ($G = 6.67259 \times 10^{-8}\,\mathrm{cm^3\,g^{-1}s^{-2}}$), $c$ is the speed of light ($c = 2.99792458 \times 10^{10}\,\mathrm{cm\,s^{-1}}$) and $M$ the mass of the body. The more general definition of the radius of the event horizon, $R_h/R_g = 1 + \sqrt{1-a^2}$ (where $R_g = R_S/2 = GM/c^2$ is the gravitational radius), takes into account the spin of the BH, defined as a function of its angular momentum $J$ as $a = Jc/GM^2$ ($a = 0$ for a non-rotating BH, and $a = 1$ for a maximally-rotating BH, Thorne 1974). In addition to the event horizon, another important boundary is the innermost stable circular orbit (ISCO), beyond which no stable orbit can exist and matter is forced to spiral into the BH. The ISCO depends on the BH spin, such that for matter orbiting around a non-rotating BH it is located at $6R_g$, for matter co-rotating with a maximally spinning BH $R_{ISCO} = 1.23R_g$, while for retrograde orbits around a maximally spinning BH $R_{ISCO} = 9R_g$ (see figure 1, lower left panel of Matt 2006). BHs were also predicted by stellar evolution theories, as the end product of the collapse of massive stars. Indeed, neutron stars (NS) exceeding the Tolman-Oppenheimer-Volkoff limit of $\sim 1.5-3M_\odot$ (Oppenheimer and Volkoff, 1939; Tolman, 1939), cannot sustain their own weight and are forced to undergo further gravitational collapse, ultimately leading to the formation of a BH.

Given their physical properties, empirical evidences of the existence of BHs in our Universe turned out to be hard to find. Consequently, these objects remained just a theoretical idea for many years. Indeed, the first observational confirmation of the existence of BHs dates back to the early 70s, about two centuries after their first theoretical prediction. The Cygnus X-1 (Cyg X-1, hereafter) X-ray source (Bowyer et al., 1965) was the first source widely accepted to host a BH. The accurate location (Tananbaum et al., 1971; Rappaport et al., 1971; Miyamoto et al., 1971) led to the discovery of a radio source (Braes and Miley, 1971; Hjellming and Wade, 1971) associated with Cyg X-1 (Tananbaum et al., 1972) and close to the optical star HDE 226868. From the orbital parameters of the optical counterpart, it was possible to infer the mass of Cyg X-1 (Bolton, 1972) and identify the source as a BH.

Known astrophysical BHs cover a wide range of masses: from the small BHs ($\sim 10\,\mathrm{M_\odot}$) that form from the death of a massive star, to the supermassive BHs ($\sim 10^5 - 10^{10}\,\mathrm{M_\odot}$) thought to reside at the centre of almost every galaxy (Kormendy and Richstone, 1995). BHs are routinely discovered and studied via indirect methods, namely by looking at the way stars, gas, and radiation in their vicinity are affected by their presence. In particular, the availability of a sufficient gas reservoir close to the BH leads to the formation of a luminous accretion disc. Vis-

cous interactions within the disc allow angular momentum to be transferred out while matter slowly diffuses onto the BH (Shakura and Sunyaev, 1973). Actively accreting BH systems can persistently emit enormous amounts of radiation across the entire electromagnetic spectrum, up to hard X-rays (energies of hundreds of keV, e.g. Elvis et al. 1994) or higher. In particular, the X-ray radiation is thought to originate from the most compact, inner regions of the accretion flow (Fabian and Miniutti, 2005). Observations in this waveband allow us to study matter under the strongest gravitational pull, providing us with a unique view of the closest regions to a BH[1].

## 1.2 X-ray binaries

X-ray binaries (XRBs) are systems in which a primary, compact object and a secondary, companion (or donor) star orbit around a common centre of mass, with an active transfer of mass from the secondary to the primary which makes them luminous in X-rays. The compact object can be a BH, a NS or a white dwarf (WD). The secondary is an optically bright (usually main sequence) star where nuclear burning is still ongoing. To date, more than 500 X-ray binary systems have been discovered in the Milky Way (Avakyan et al. 2023; Neumann et al. 2023). XRBs are classified based on the nature of the compact object, and the characteristics of the companion star. Fig. 1.1 shows the three main classes and the corresponding subclassifications.

When the compact object is a BH or a NS, the main sub-classification is made as a function of the mass of the donor/companion star. This defines two subclasses, namely the Low Mass X-ray Binaries (LMXBs) and the High Mass X-ray Binaries (HMXBs).

LMXBs are old systems ($\sim 10^{10}$y), where the optical companion star is usually faint (i.e. $L_{opt}/L_x << 0.1$), has a mass $M_* \lesssim 1\mathrm{M}_\odot$, and a spectral class later than A. It can be a main sequence star, a sub-red or a red giant, but there are LMXBs in which also a WD can assume the role of the donor.

In LMXB the transfer of mass proceeds from the donor/companion star to the primary compact star via Roche lobe overflow. When the Roche lobe (the equipotential surface around the system bounding the material to the star) of the donor star is filled (either due to the evolution of the star or due to the shrinking of the orbital separation of the system), the donor's gas is funnelled through the inner Lagrangian point (see left panel in Fig. 1.2) towards the compact star. Because

[1]Despite a direct view of a BH has now been proved possible thanks to the high resolution images provided by the Event Horizon Telescope (Event Horizon Telescope Collaboration et al., 2019, 2022), the application of this technique is at the moment very limited to a bunch of nearby supermassive BHs (Martí-Vidal, 2023).

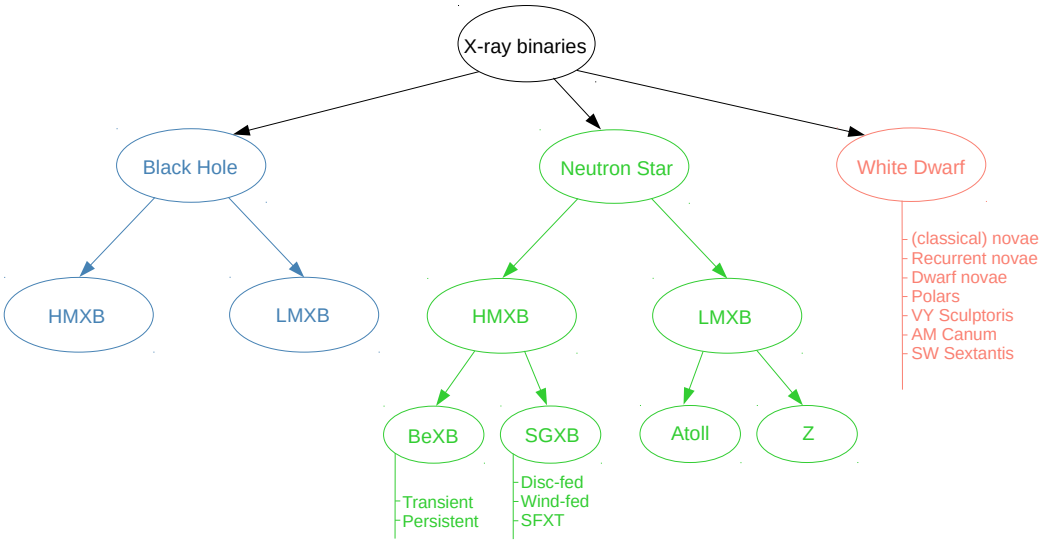


**Figure 1.1:** Classification of X-ray Binaries. Readapted from Reig (2011)

of conservation of angular momentum, the transferred material starts spiralling around the compact star forming an accretion disc, which, depending on the properties of the compact object (e.g. magnetic field), may or may not reach the ISCO. All known LMXBs are transient sources, showing luminous optical and X-ray outbursts (Dunn et al., 2010; Russell et al., 2018), characterised by a sudden increase of luminosity by several orders of magnitude within a few days, followed by a slower decay (typically over a period of months) before the system returns to quiescence. This behaviour is thought to be driven by a thermal-viscous instability in the disc (Meyer and Meyer-Hofmeister, 1981; Cannizzo et al., 1995; King and Ritter, 1998; Lasota, 2001) which leads to a more rapid transfer of mass onto the compact object and an increase of brightness. Throughout an outburst the mass transfer rate varies between $10^{-11}$ (during quiescence) and $10^{-8}\,\mathrm{M}_{\odot}\,\mathrm{y}^{-1}$ (Frank et al., 2002). Since the last census made in the early 2000 (Ritter and Kolb, 2003; Liu et al., 2007), the number of LMXBs in the sky drastically increased and nowadays, we count 348 LMXBs and candidates.

HMXBs are younger systems ($\sim 10^{7}$y) containing a massive donor star with $M_{*} \gtrsim 5\mathrm{M}_{\odot}$, of early type O or B (i.e. $L_{opt}/Lx > 1$). The canonical accretion channel in these systems is accretion via stellar winds. The strong stellar wind emitted from the companion star would fall into the Roche lobe of the compact object, directly feeding it (Bondi and Hoyle, 1944). Not having sufficient angular momentum, in most of the systems, the stellar wind material would not be able to

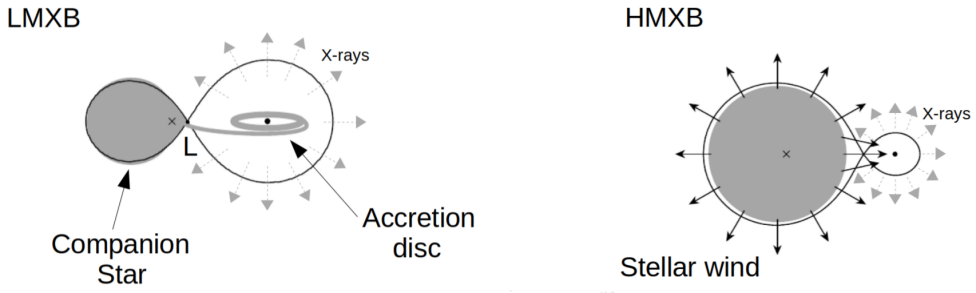


**Figure 1.2:** Scheme of the accretion processes in LMXBs and HMXBs. Readapted from Tauris and van den Heuvel (2006)

form an accretion disc (right panel in Fig. 1.2). For stellar wind fed systems, the mass loss is between $10^{-6}$ and $10^{-5}\,M_\odot\,y^{-1}$, with only the 0.01-0.1% transferred to the compact object (Frank et al., 2002). HMXBs are very bright in the X-ray sky and are usually persistent sources. In the latest catalogue (Neumann et al., 2023), only 169 XRBs were classified as HMXBs (not including sources in the Small and Large Magellanic Cloud).

Sources pertaining to the subclass of XRBs with a stellar BH as the primary are usually referred to as black hole X-ray binaries (BHXRBs). To date, less than 90 BHXRBs have been found in the Milky Way. More than 70 of them are LMXBs and only 6 are classified as HMXBs (Corral-Santana et al., 2016; Tetarenko et al., 2016; Neumann et al., 2023; Avakyan et al., 2023). The first BHXRBs were discovered in the 1970s (e.g. Tananbaum et al. 1972; Elvis et al. 1975). In the following sections, we will focus on BHXRBs, and describe their main X-ray spectral and timing characteristics.

## 1.3 The X-ray emission of BHXRBs

BHXRBs can emit radiation in the entire energy spectrum, from radio to gamma rays. In general, the primary emission in the observed X-ray spectrum of a BHXRB is characterised by a soft and a hard spectral component, whose relative contribution depends on the accretion state of the source (Sect. 1.4). While the soft component is represented by the thermal emission from the accretion disc, the hard component is generated by inverse Compton scattering processes in a cloud of hot electrons located close to the BH. Fig. 1.3 shows the main components contributing to the X-ray spectrum that are described in details in the following

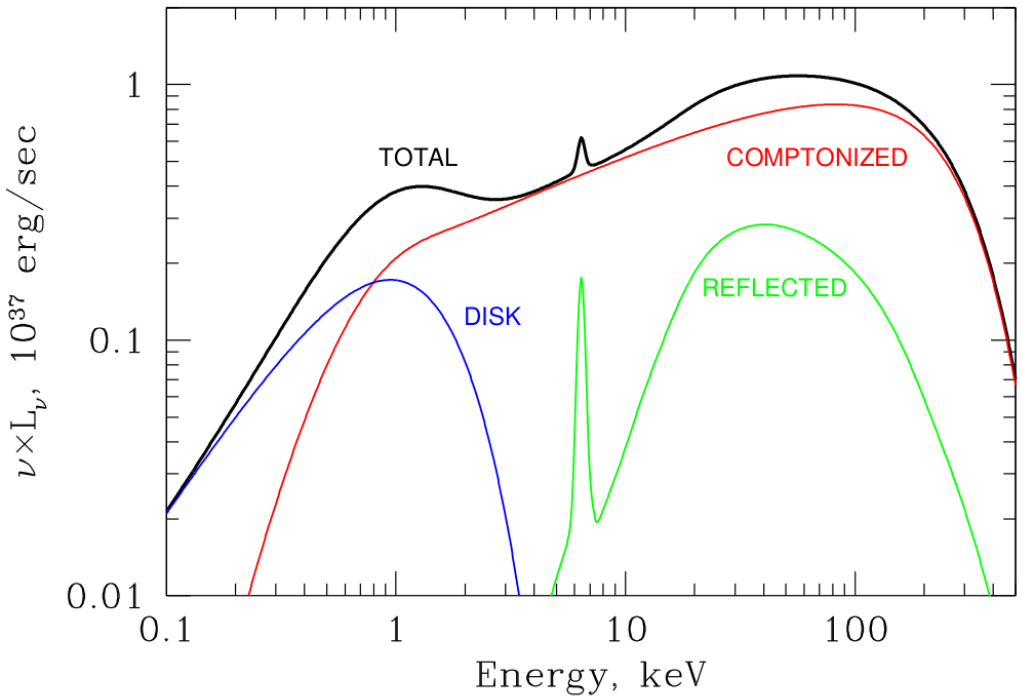


**Figure 1.3:** Main components characterising the X-ray spectrum of a BHXRB. From Gilfanov (2010).

sections.

### 1.3.1 The accretion disc

During accretion, the material ejected from the donor star starts rotating along Keplerian orbits around the BH. The accreting matter slowly spirals inwards, losing angular momentum due to the shear stress caused by the viscosity and turbulences in the gas (likely due to magneto-rotational instability, Balbus and Hawley 1991), and forming an accretion disc. In the canonical $\alpha$-disc model (Shakura and Sunyaev, 1973), the accretion disc is described as a geometrically thin ($H/R << 1$, where $H$ is the height of the accretion disc at a radius $R$) and optically thick ($\tau >> 1$) structure, generating thermal emission. At each radius $r = R/R_g$, the resulting emission is a blackbody spectrum with a characteristic temperature $T(r) \propto r^{-3/4}$. In its totality, the resulting accretion disc spectrum is a superposition of blackbody spectra, or a "multicolour disc blackbody". The peak in temperature corresponds to the temperature at the innermost radius of the accretion disc. This is due to the fact that, at smaller radii, gravitational effects

are stronger, generating more luminosity that can be dissipated in a smaller area, thus producing a net increase of temperature. This thermal emission describes the spectral component that dominates the soft band of the X-ray spectrum (in blue in Fig. 1.3) of a BHXRB (Davis et al., 2005). Its observed peak temperature ranges between $kT_{in} \lesssim 0.2$ keV and 1 keV between the least and the most luminous accretion states of an outburst (Sect. 1.4).

### 1.3.2 The Comptonisation component

The thermal emission from the accretion disc cannot explain the observed hard X-ray emission, extending to hundreds of keV in the spectrum of BHXRBs (in red in Fig. 1.3), therefore another spectral component is necessary. This emission is explained in terms of inverse Compton scattering of soft photons from the cold accretion disc in an optically thin ($\tau_C \sim 1$) cloud of hot (thermal, and possibly also non-thermal) electrons located in the vicinity of the BH (Sunyaev and Truemper, 1979; Sunyaev and Titarchuk, 1980). The thermal (Maxwellian) distribution of electrons in the hot cloud produces a smooth power law due to the superposition of multiple Compton scattering spectra. The observed X-ray flux density has the form $F(E) \propto E^{-\Gamma}$, where $\Gamma$ is the photon index parameter, which depends on the temperature and optical depth of the Comptonising medium. The observed $\Gamma$ typically ranges between 1.5 and 2.5, depending on the accretion state of the source (Sect. 1.4), even reaching values as high as $\sim 4$ in some high luminosity states. The thermal Comptonisation component shows a cut-off at high energies (Motta et al., 2009), which represents a diagnostic of the temperature of the thermal Comptonising electrons. In some cases the cut-off is not observed up to $\sim$1 MeV, suggesting significant contribution from a non-thermal population of electrons (Zdziarski et al., 2001). Despite being the dominant spectral component in some accretion states, the exact nature and geometry of the Comptonising region (usually refereed to as "corona", or "hot flow") is currently unknown (Poutanen et al., 2018). However, some viable proposed geometries imply that only a small fraction of seed photons from the disc can intercept the corona (at least in some, low luminosity accretion states). A solution to this problem invokes cyclo-synchrotron radiation from the hot flow itself to represent an additional source of seed photons (Veledina et al., 2013).

### 1.3.3 The disc reflection component

A fraction of the high-energy photons produced via inverse Compton scattering in the corona is re-emitted towards the disc, where they undergo further reprocessing. Here various radiative processes can take place, depending on the energy

of the impinging photons. At soft X-ray energies, photoelectric absorption dominates over electron scattering, thus producing a complex spectrum of absorption edges and emission lines. At hard X-ray energies electron scattering dominates, producing a characteristic smooth broad feature, the Compton hump, peaking at $\sim 30 - 50\,\mathrm{keV}$. The resulting reflection component is shown in Fig. 1.3 (green) and Fig. 1.4.

The disc reflection spectrum depends on several parameters of the system, including the ionisation state and density of the disc, the illumination profile, and the geometry of the disc and the corona (Ross and Fabian, 2005; García et al., 2015, 2016). The most prominent emission line in the disc reflection spectrum is the Fe K$\alpha$ fluorescence line at 6.4 keV for a neutral medium, but shifted at higher energies if the gas is ionised (Makishima, 1986). This intrinsically narrow line can be broadened by different effects. In a Newtonian scenario (i.e. the emitting material

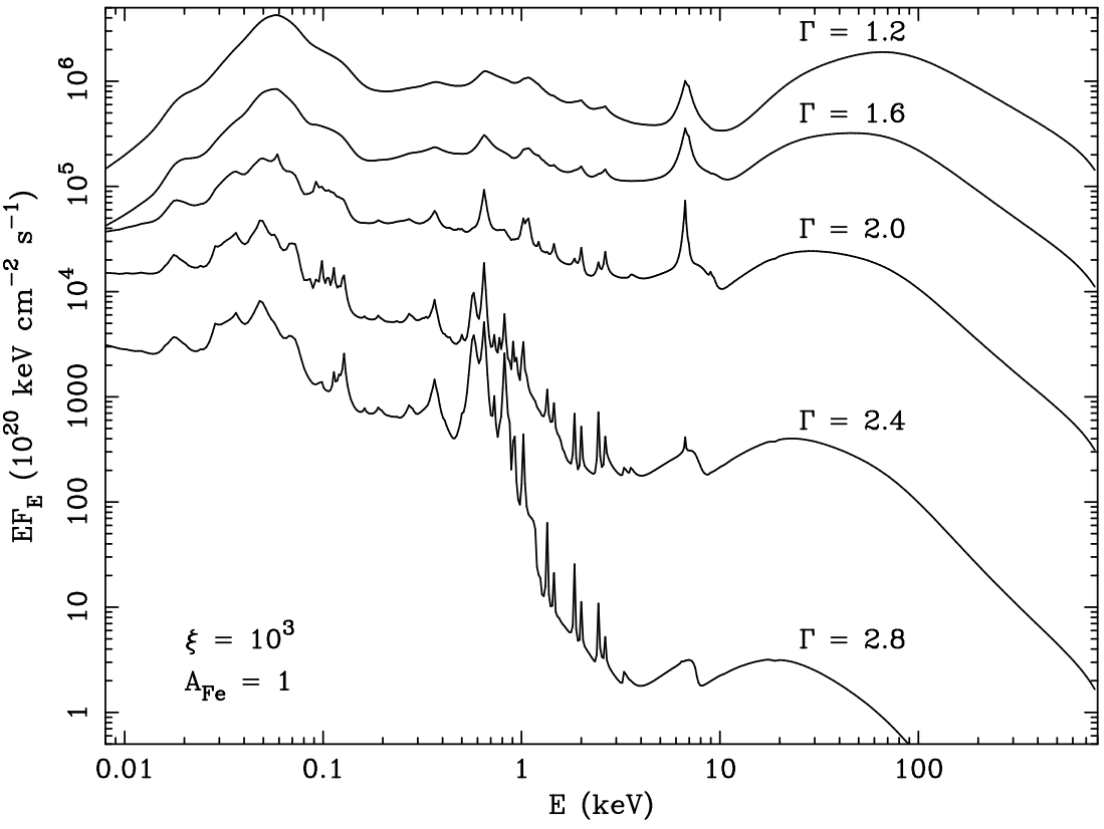


**Figure 1.4:** Disc reflection spectra for different values of the spectral index (as indicated in the labels). The disc has an ionisation parameter of $\xi = 10^3\,\mathrm{erg\,cm\,s^{-1}}$ and solar iron abundance. From Ross and Fabian (2005).

is moving at non relativistic velocities), the emission line shows a symmetric double peaked profile, as a consequence of Doppler effects. However, the vicinity to the BH further modifies the line profile as a consequence of relativistic effects. Indeed, for material orbiting within $\sim 10\ R_g$ from the BH, these effects become important (see figure 1 of Matt 2006). Transverse Doppler shift and beaming (due to special relativity) boost the emission from the blue peak of the line, while the gravitational redshift (due to GR) shifts the line to lower energies. This results in a skewed and broadened line profile (Fig. 1.5). This feature is considered a powerful diagnostic of the innermost regions of the accretion flow, as its shape strongly depends on several important parameters (including the BH spin and the disc truncation radius, e.g. Matt 2006).

## 1.4 Accretion states of BHXRBs

BHXRBs undergo quick transitions among different states, during which both the X-ray spectra (Homan and Belloni, 2005) and the X-ray timing (Belloni et al., 2005) properties of the source change dramatically. The observed changes are thought to be due to intrinsic variations of the physical properties of the accretion flow (Done et al., 2007), for this reason we refer to these states as "accretion states".

Two main accretion states were identified for Cyg X-1 in the '70s with the Uhuru satellite (Tananbaum et al., 1972). In less than one month, the source underwent a transition, showing a decrease of the soft X-ray flux ($2-6\,\mathrm{keV}$) by a factor of 4 and an increase in the high energy X-ray flux by a factor of 2. In 1975, also the transient BHXRB A 0620-00, discovered with the Ariel satellite, showed a similar spectral transition (Coe et al., 1976), suggesting that this duality-state was a common feature of BHXRBs. These two states were referred to as hard and soft states. The hard state is characterised by a thermal Comptonisation-dominated spectrum. The power law describing this component has a typical photon index $1.5 < \Gamma < 2$ in the $5-20\,\mathrm{keV}$ and peak emission at $60-100\,\mathrm{keV}$ (e.g. Joinet et al. 2008; Motta et al. 2009; Gilfanov 2010). The accretion disc is still present but is weaker and cooler than in the soft state, peaking at $\sim 0.2-0.3\,\mathrm{keV}$ (Done et al. 2007 for a review). The soft state shows a dominant contribution from the multicolour black body emission from the accretion disc, peaking at $\sim 1\,\mathrm{keV}$ (e.g. Gierliński and Done 2004). A hard power law tail with $\Gamma \geq 2$ is sometimes observed, extending to very high energies without any detected cut-off. This component might be related to Comptonisation in a non-thermal/hybrid plasma. More recent intensive monitoring of BHXRB systems, allowed additional accretion states to be identified.

The spectral evolution of a BHXRB is usually described in terms of variations of luminosity as a function of spectral hardness (i.e. ratio of fluxes between a hard and a soft energy band, Belloni 2010b) in a hardness-intensity diagram (HID, in

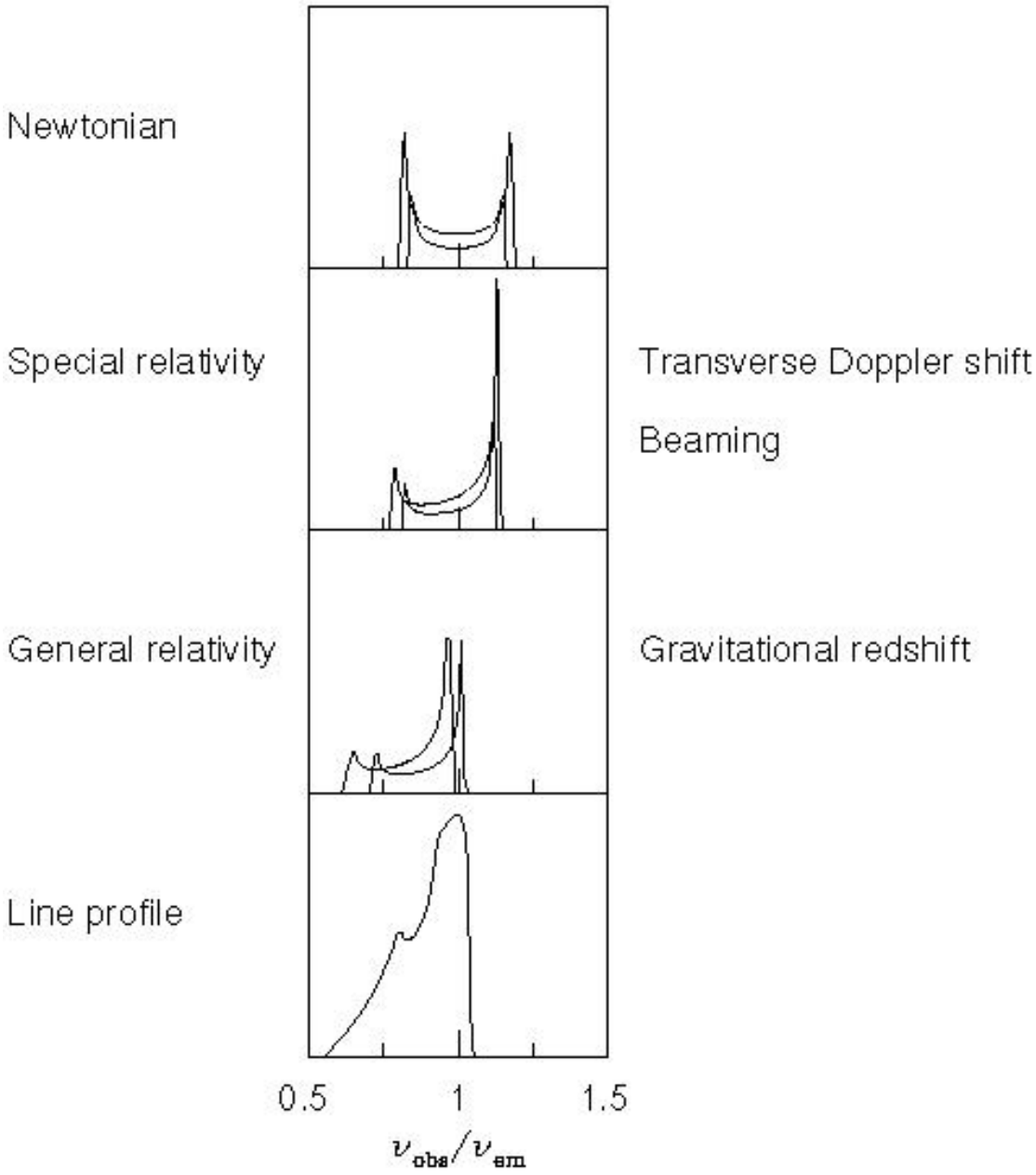


**Figure 1.5:** Distortions of the profile of an intrinsically narrow emission line due to relativistic effects. From top to bottom: line profile in the Newtonian case; special relativity effects (i.e. transverse Doppler shift and beaming) cause an increase in flux for the blue peak; general relativity effects (i.e. gravitational redshift) cause a shift to lower energies; the resulting profile considering the above-mentioned effects. From Fabian and Miniutti (2005).

Fig. 1.6, upper panel). This diagram results particularly useful to recognise different accretion states. During an outburst, transient BHXRBs are observed to evolve from a state of quiescence, characterised by luminosities of $L_X \sim 10^{30-34}\,\mathrm{erg\,s^{-1}}$, to a series of more luminous ($L_X \sim 10^{36-38}\,\mathrm{erg\,s^{-1}}$) accretion states, following a hysteresis cycle. This evolution results in a q-shaped path traversed in counterclockwise direction in the HID (e.g. Homan and Belloni 2005; Dunn et al. 2010; Belloni 2010b; Belloni and Motta 2016). Starting from a low luminosity hard state (right part of the HID, at higher spectral hardness in Fig. 1.6), over a period of weeks or months, the luminosity varies by three or four orders of magnitude, reaching its maximum for mild changes in hardness. As time progresses, the source goes through a series of intermediate states characterised by the presence of a disc and a steep ($\Gamma > 2$) power law component (horizontal, upper branch of the HID, Fig. 1.6) finally reaching the soft state. This transition has a typical duration of a few days (Homan et al., 2020). Once in the soft state (left part of the HID, at lower spectral hardness, Fig. 1.6), the X-ray luminosity varies by one or two orders of magnitude in a period of months. A consequent, final transition from the soft to hard state (lower horizontal branch of the HID in Fig. 1.6) characterised by a drop in luminosity and a sudden increase of spectral hardness marks the end of the outburst and the slow return to the final state of quiescence. On the other hand, persistent sources, such as Cyg X-1, are always observed to transition between the hard and soft state, populating one of the two transition branches of the HID with relatively minor changes in their luminosity (Fig. 1.7).

Another distinctive property of BHXRBs is the strong variability of the emitted X-ray flux, observed over a wide range of timescales (from tens to fractions of seconds). This variability is characterised by an aperiodic behaviour, whose characteristics (e.g. variability power, characteristic timescales) strongly change as a function of the accretion state (Belloni et al., 2005). In addition, in some accretion states quasi periodic oscillations (QPOs; Ingram and Motta 2019 for a review) emerge on top of the broad band aperiodic component. In BHXRBs, most of QPOs appear at frequencies between $\sim 0.01$ Hz and $\sim 10$ Hz, and have been classified in three types: A, B and C (Wijnands et al., 1999; Sobczak et al., 2000; Casella et al., 2005; Motta et al., 2015). While type–A QPOs are weak and broad, type–B and type–C are intense and narrow features. Depending on the accretion state, different types of QPOs may appear. The distribution of variability power (i.e. the power spectrum, PSD, Sect. 3.2.1) in the hard state shows a high level of aperiodic X-ray variability, with fractional root mean square (rms) variability of $30\% - 40\%$ (Muñoz-Darias et al. 2011; Heil et al. 2012). The power spectrum can be empirically decomposed in Lorentzian components of different widths and whose characteristic frequencies change as a function of the accretion state, typ-

ically shifting to higher values as the source softens (e.g. Nowak 2000; Belloni et al. 2002; Pottschmidt et al. 2003; Klein-Wolt and van der Klis 2008). At high hard state luminosities these sources can show strong QPOs, mostly of type–C, also shifting to higher frequencies as the spectral hardness decreases (Psaltis et al. 1999; Wijnands and van der Klis 1999). Type–C QPOs present high amplitude (up to 20% rms) and a narrow peak ($Q \gtrsim 8$, with $Q$ defined as the quality factor, i.e. ratio between the frequency of the QPO peak and its full width at half maximum) in the PSD (bottom panel in Fig. 1.8) appearing at frequencies 0.01–1 Hz. As the source moves towards the soft state the variability power decreases. During the transition, type–B QPOs may appear at frequecies of 5–6 Hz (but see also Motta et al. 2011), narrow features ($Q \gtrsim 6$) with a high amplitude (up to 5% rms, middle panel in Fig. 1.8). In the soft state, the level of fractional rms variability is very low ($1 - 5\%$, Muñoz-Darias et al. 2011; Heil et al. 2012), and appears as a weak steep component in the PSD. Rarely, weak QPOs can be detected, e.g. type–A QPOs, with a few percent rms and a broad ($Q \lesssim 3$) peak at frequencies of 6–8 Hz (upper panel in Fig. 1.8). Given the observed strong changes, X-ray variability can be also used as a tracer of the accretion state of the source. Model-independent approaches for tracing the accretion state through X-ray variability make use of the hardness-rms diagram (HRD, lower panel in Fig. 1.6, Muñoz-Darias et al. 2011; Heil et al. 2012) or the evolution of the ratios of total rms measured in different frequency bands, the so-called power-colours (Heil et al., 2015).

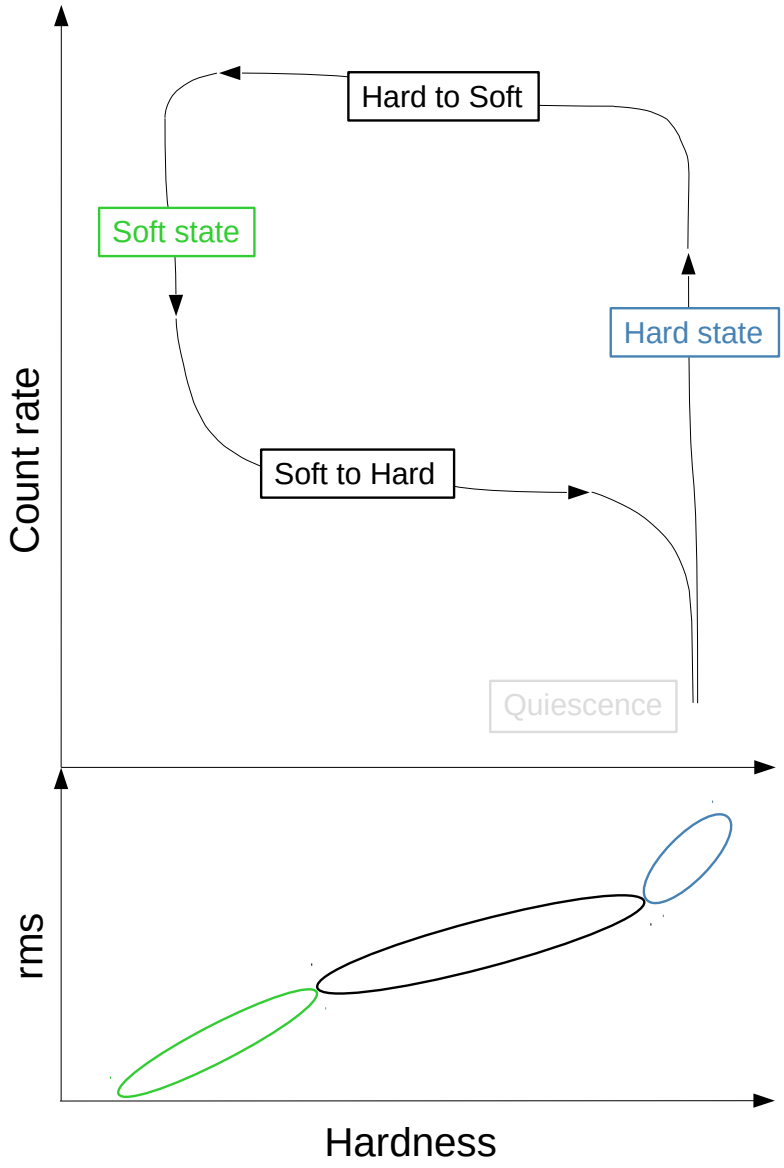


**Figure 1.6:** Schematic behaviour of the main states and transitions of a transient BHXRB in the hardness-intensity diagram (HID, top panel) and hardness-rms diagram (HRD, bottom panel). Readapted from Belloni (2010a).

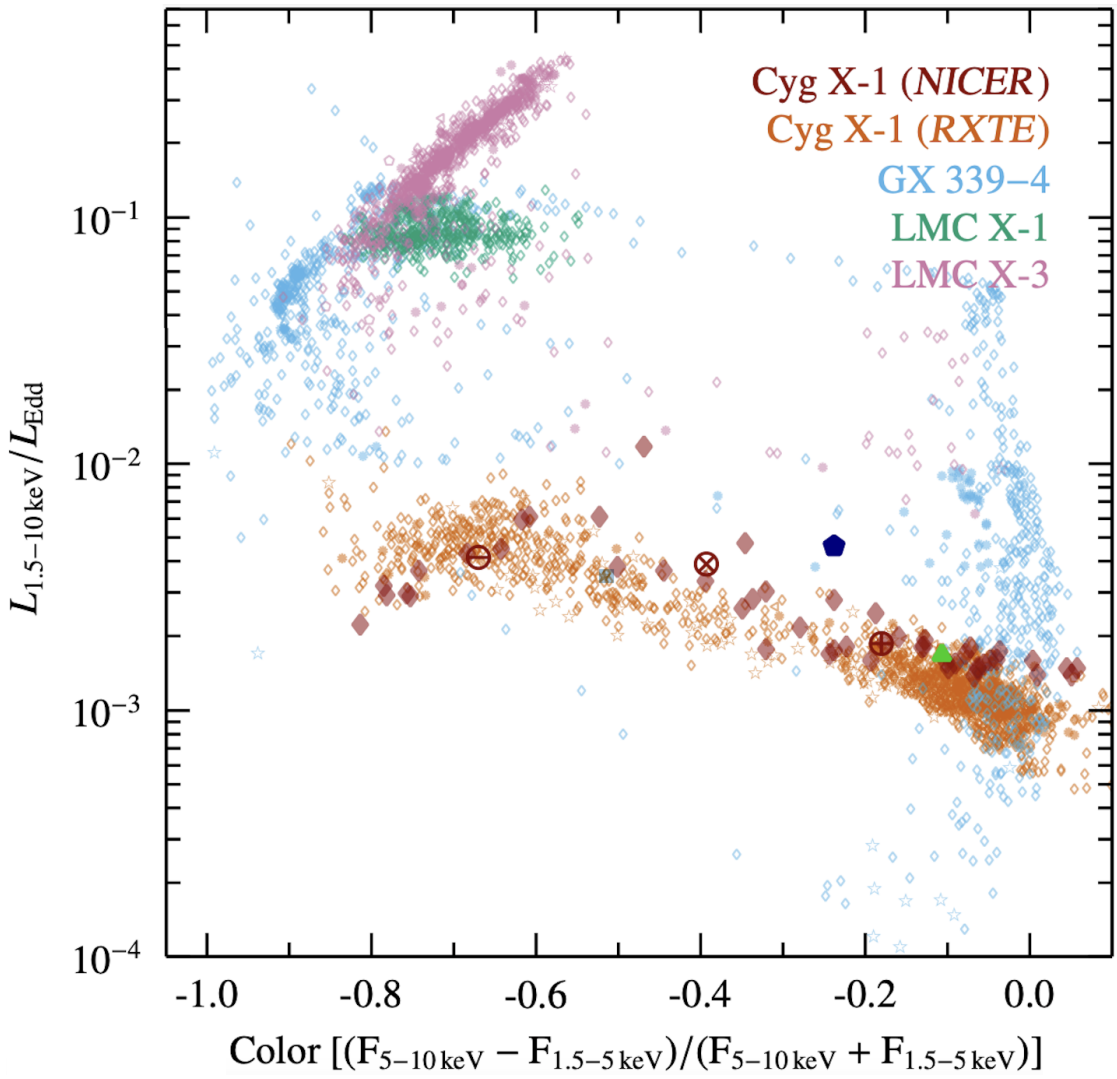


**Figure 1.7:** HID diagram of Cyg X-1 observed by *RXTE* and *NICER*, as compared to that of other BHXRBs from the *RXTE* archive. From König et al. (2024).

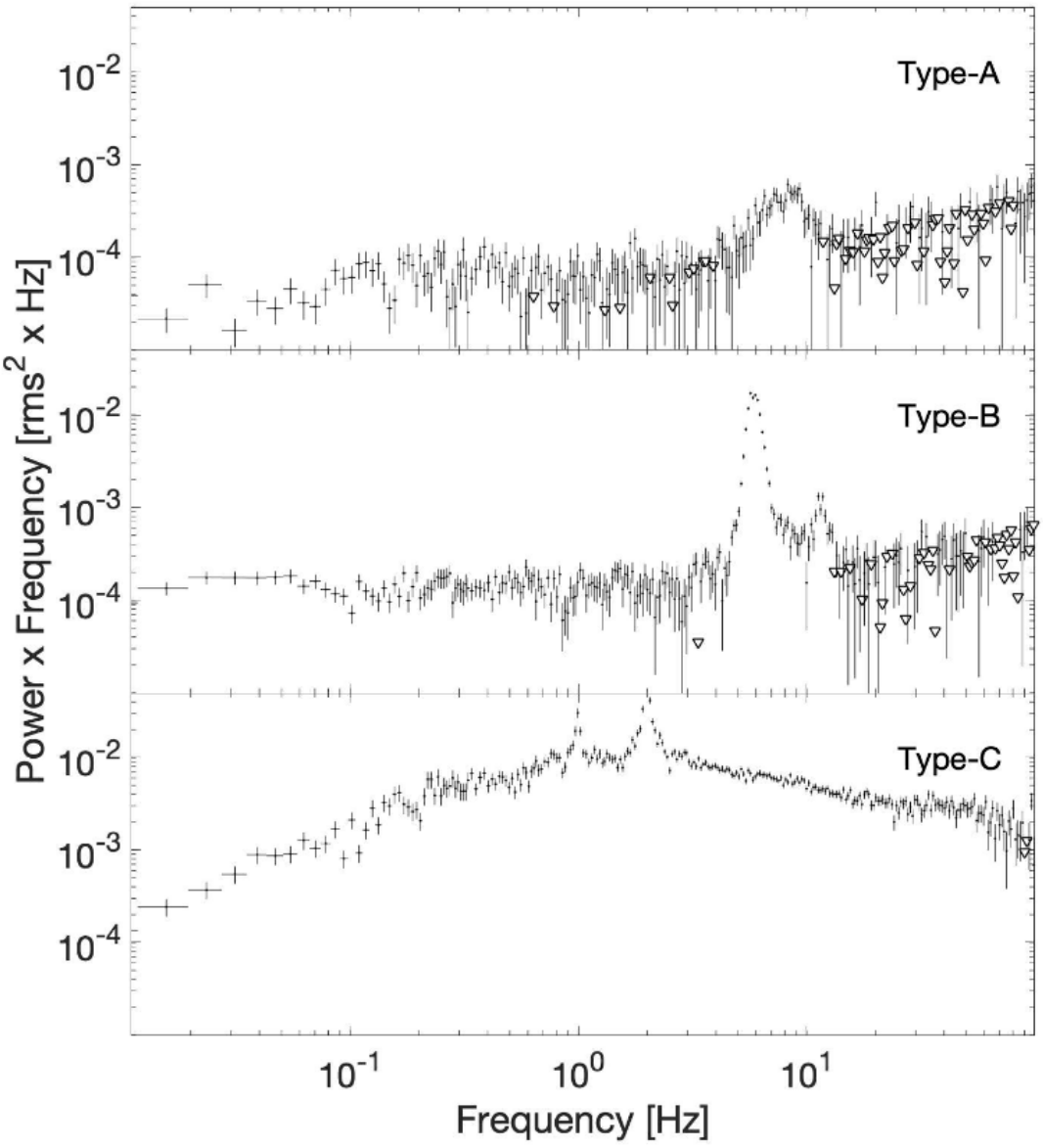


**Figure 1.8:** Examples of different types of QPOs. From top to bottom: QPOs from the sources XTE J1859+226 (type–A), GX 339-4 (type–B) and GX 339-4 (type–C). From Ingram and Motta (2019).

# Chapter 2

# The X-ray source: Cyg X-1

## 2.1 Discovery and history

The Cyg X-1–HDE 226868 system is one of the most studied BHXRBs. Cyg X-1 was one of the eight X-ray sources discovered by the Geiger counters on board the Aerobee rocket launched in New Mexico in 1964 (Bowyer et al. 1965) with the purpose of mapping the X-ray sky. In 1971, the correct location was determined thanks to the UHURU satellite (Tananbaum et al. 1971), an MIT rocket flight (Rappaport et al. 1971) and several Japanese balloon flights (Miyamoto et al. 1971). From these exact coordinates, a radio source was identified with Cyg X-1 by Braes and Miley (1971) and Hjellming and Wade (1971). The highly variable X-ray emission (on timescales as short as tens of milliseconds corresponding to light-travel time across $10^9$ cm) from Cyg X-1 suggested the source to be a compact object. The companion star HDE 226868 was identified in the optical band independently by Murdin and Webster (1971) and Bolton (1972), and found to coincide (within a 3 arcsec error, Fig. 2.1) with the faint and variable radio source associated with Cyg X-1. Its spectral classification as a O9.7 Iab supergiant variable star was inferred by Walborn in 1973. The identification of the companion star allowed the mass of the compact object to be estimated from the orbital parameters. Bolton (1972) estimated a mass of $6M_\odot$[1] for Cyg X-1 exceeding the limit mass for a NS (Sect. 1.1). This result gave strong evidence that the compact object in Cyg X-1 is indeed a BH.

[1]This value has been recently updated by Miller-Jones et al. 2021 with new astrometric data, see Sect. 2.2.

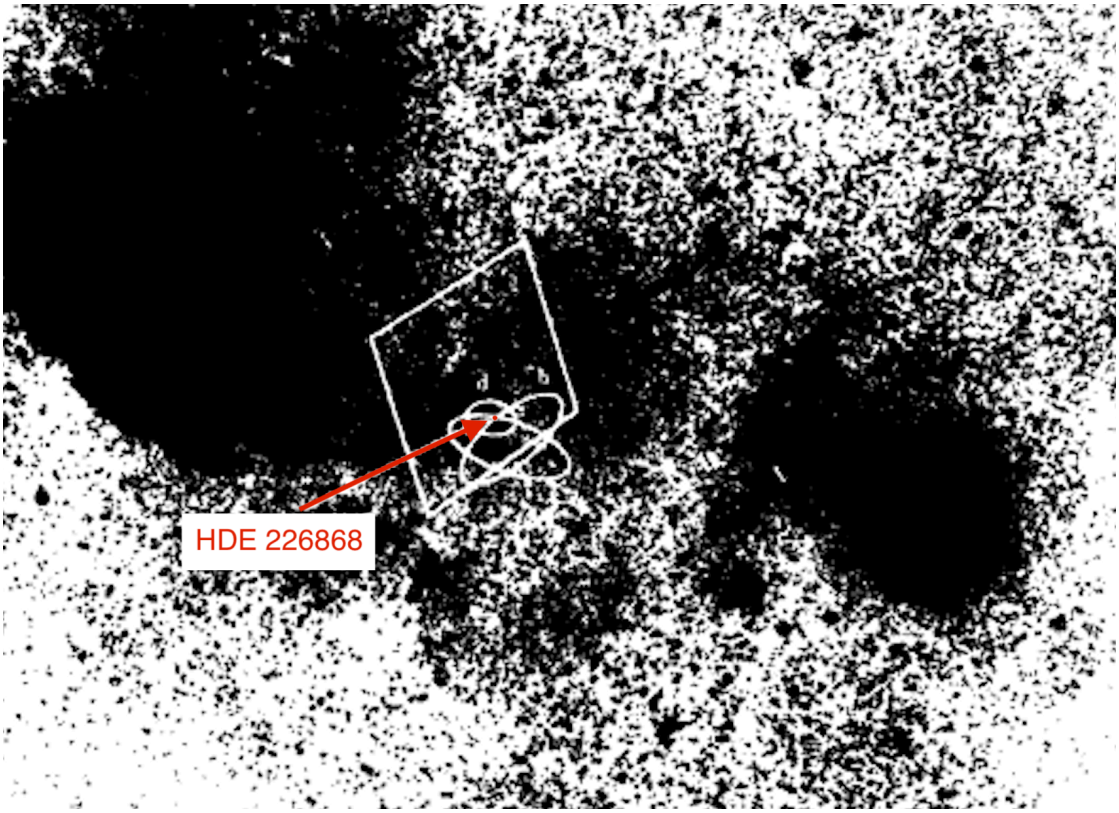


**Figure 2.1:** Location of HDE 226868 emitting close to Cyg X-1 obtained in 1971 (from Oda 1977, readapted).

## 2.2 The binary system

**Location:**
Cyg X-1 is located in the Cygnus constellation (Fig. 2.2). It is visible in the boreal hemisphere on the Milky Way's galactic plane, easily recognisable in the summer/autumn sky due to its "swan" shape, from which it takes the Latin name. Cyg X-1 is located at a distance of $2.22^{+0.18}_{-0.17}$ kpc (Miller-Jones et al. 2021), close to $\eta$ Cyg with a right ascension, RA, of $19^{\rm h}\ 58^{\rm min}\ 21.7^{\rm s}$ and a declination $\delta$ of $+35°12'06''$ (Liu et al. 2006).
**Orbital elements:**
The system has an orbital period of 5.599829(16) d (Gies et al. 2003), the orbit is nearly circular, with an estimated eccentricity of $e \sim 0.018$ and inclination $i \sim 27°$ (Miller-Jones et al. 2021). In addition, the source shows a superorbital period of 150 d (Brocksopp et al. 1999; Benlloch et al. 2004; Poutanen et al. 2008), which was observed to increase to twice this value from 2005 to 2010 (Zdziarski et al. 2011).
**The BH in Cyg X-1:**
The most updated estimates of the BH mass of Cyg X-1 report $M_{BH} = 21.2 \pm 2.2\,{\rm M}_\odot$, the highest value found for a BH after the extragalactic system M33 X-7 (Orosz et al. 2007; Miller-Jones et al. 2021). Recent estimates of the BH spin report $a > 0.9985$ (Zhao et al. 2021), although these estimates are highly model-dependent and lower values have been proposed (Zdziarski et al., 2024). The accretion disc around the BH, not usually present in HMXBs, is confirmed by the detection of a thermal disc blackbody component, as well as a reflection component (see Sect. 2.3, e.g. Ross and Fabian 2005; Gilfanov 2010).
**The companion star HDE 226868:**
The companion star HDE 226868 is a O9.7Iab supergiant (Bolton 1972). Through the years several attempts were made to constrain the mass of HDE 226868. Recently, Miller-Jones et al. (2021) constrained the distance of the system via radio astrometry. Combining radio and optical archival data, they infer the masses of the BH and its companion. For HDE 226868, they found a mass $M_* = 40.6^{+7.7}_{-7.1}\,{\rm M}_\odot$ and a radius $R_* = 22.3 \pm 1.8\,{\rm R}_\odot$. From its surface, strong and highly variable stellar winds are launched (see Sect. 2.5, e.g. Lucy and Solomon 1970; Castor et al. 1975; Owocki et al. 1988; Feldmeier et al. 1997).

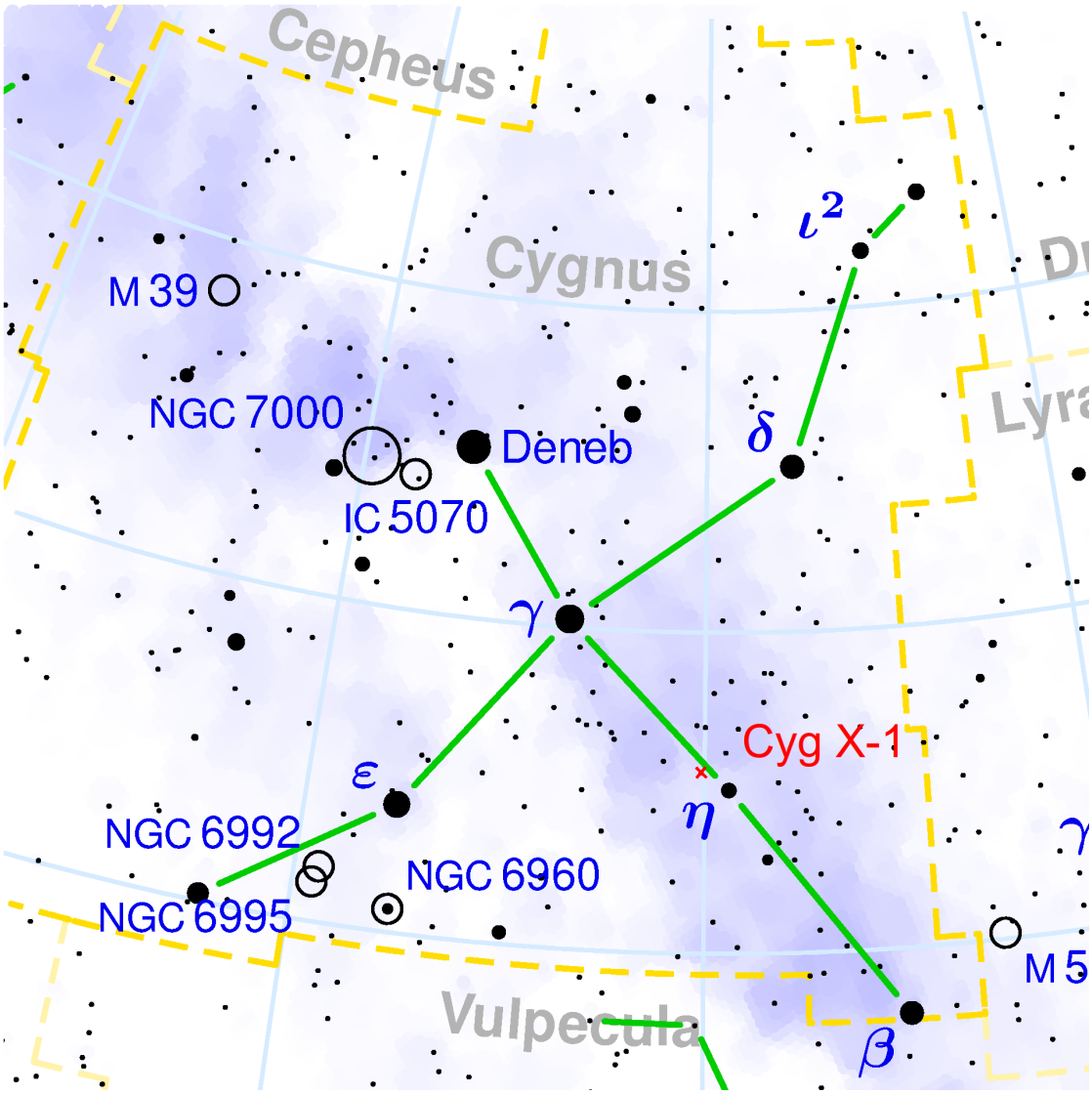


**Figure 2.2:** The Cygnus constellation and the position of Cyg X-1 (image by Copyright @2003 Torsten Bronger, readapted).

## 2.3 The X-ray spectrum of Cyg X-1

Cyg X-1 is visible from gamma (Zanin et al., 2016; Zdziarski et al., 2017), to radio wavelengths (Stirling et al., 2001). However, the X-ray band is where most of its power is emitted. As a matter of fact, Cyg X-1 has been for a long time classified as one of the brightest known X-ray galactic sources. In 1972, Tananbaum et al. (1972) identified a bimodal behaviour of the source: Cyg X-1 stays most of the time in the hard state, with rare transitions to the soft state.

In the hard state, the source reaches luminosities $L_x \sim 10^{37}\,\mathrm{erg\,s^{-1}}$ (e.g. Gierlinski et al. 1997). In this state, the peak of Cyg X-1 emission is at $\sim 100$–$200\,\mathrm{keV}$ (upper panel in Fig. 2.3, Gierlinski et al. 1997; Grove et al. 1998; Zdziarski et al. 1998; Wardziński et al. 2002), as commonly seen in BHXRBs. The corresponding dominant radiative process is thermal Comptonisation. Photons emitted in the accretion disc are scattered in a plasma (with optical depth $\tau_C \sim 1$, e.g. Gierlinski et al. 1997; Zdziarski et al. 1998; Frontera et al. 2001a,b; Zdziarski et al. 2002, 2003) of thermal electrons at a temperature of $kT_e \sim 50$–$100\,\mathrm{keV}$, with a power law shape of slope $\Gamma \lesssim 2$ (e.g. Grinberg et al. 2013; Basak et al. 2017; Zhou et al. 2022). Beyond the thermal-Compton spectrum, a weak hard tail is observed, possibly due to an hybrid (i.e. thermal and non-thermal) distribution of electrons (McConnell et al., 2000; Zdziarski et al., 2001; McConnell et al., 2002). Additionally, Compton reflection in the accretion disc is observed, producing an intense fluorescent Fe K $\alpha$ line (e.g. Gierlinski et al. 1997; Zdziarski et al. 1998; Di Salvo et al. 2001; Frontera et al. 2001a; Wardziński et al. 2002; Tomsick et al. 2014; Basak et al. 2017). The reflection component can be modified by relativistic effects (see Sect. 1.3.3, Di Salvo et al. 2001), particularly in the softer part of the hard state (Frontera et al., 2001a; Miller et al., 2002). The cold accretion disc in the hard state shows temperatures of $kT_{in} \sim 0.1$–$0.2\,\mathrm{keV}$ (e.g. Basak et al. 2017), thus dominates at soft energies. Cyg X-1 shows additional spectral curvature in the soft band, associated with a "soft excess" (Basak et al., 2017). This feature has been observed also in other BHXRBs (Zdziarski et al., 2001; Kubota et al., 2001), and has been ascribed to a warm coronal component, which hints at a spectral stratification of the Comptonising medium (Axelsson and Done, 2018).

The soft state of Cyg X-1 is characterised by slightly higher X-ray luminosities ($\sim 50-70\%$ above the hard state luminosity, Zhang et al. 1997). The X-ray spectrum in the soft state (bottom panel in Fig. 2.3) is described by the same spectral components observed in the hard state, but with different relative contribution to the total X-ray flux (Poutanen et al. 1997). The dominant component in the soft state is the thermal emission from the accretion disc, which is observed to be hotter than in the hard state ($kT_{in} \sim 0.4$–$1\,\mathrm{keV}$, Tomsick et al. 2014; Walton et al. 2016; Kushwaha et al. 2021). In the soft state, the Comptonisation component is ascribed to non-thermal electrons in a hybrid distribution peaking at $E \gtrsim 10\,\mathrm{keV}$

(e.g. Wilms et al. 2006), resulting in a much stronger hard tail than in the hard state (Gierliński et al. 1999; Zdziarski 2000; Zdziarski et al. 2002), and a power law slope of $\Gamma \gtrsim 2.5$ (Grinberg et al. 2013; Tomsick et al. 2014; Walton et al. 2016). A soft excess is also observed, and is ascribed to Compton scattering by the thermal electrons of the hybrid distribution. Intermediate states show spectral properties that are in between those characterising the hard and the soft state, like power law slopes of $\Gamma \sim 1.8 - 2.5$ (Grinberg et al. 2013; Tomsick et al. 2018) and disc temperature $kT_{in} \sim 0.3 - 0.4\,\mathrm{keV}$ (Tomsick et al. 2018). Although studying intermediate states is important in order to understand the mechanism behind state transitions, these states are short-lived, thus difficult to observe.

Cyg X-1 is a persistent system and shows somewhat different properties than transient BHXRBs. As described in Sect. 1.4, transient BHXRBs follow a clear observable hysteresis behaviour in the HID during an outburst. The upper panel of Fig. 2.4 shows the HID of Cyg X-1 (grey circles) observed by *RTXE*/PCA from February 1996 to October 2005, compared to the HID of the transient BHXRB GX 339–4 (black circles) with *RXTE*/PCA during the outburst in 2002/2003 and 2004/2005.

As clear from the plot, Cyg X-1 does not show hysteresis. The hard state branch, in the right part of the HID, is the most populated. Only a few observations populate the intermediate state branch, as expected from the fact that these states are short-lived. Occasional transitions to the soft state are observed, although Cyg X-1 never reaches states as soft as other BHXRBs. The lower panel of Fig. 2.4 shows a comparison of the HRD (see Sect. 1.4) of Cyg X-1 and GX 339–4. The same behaviour in terms of a decrease of fractional rms towards softer states is observed in the two sources, although Cyg X-1 does not appear to show the strong drop of fractional rms typical of transient BHXRBs when they evolve towards the softest states. However, the behaviour of Cyg X-1 at the lowest values of spectral hardness cannot be tested as it has never been observed in such states.

## 2.4 The X-ray variability properties

As all other BHXRBs, Cyg X-1 shows X-ray variability properties that strongly depend on the accretion state (Sect. 1.4) as well as on the energy band.
In the hard state, the PSD (Sect. 3.2.1) of Cyg X-1 shows aperiodic variability distributed over a broad range of temporal frequencies. Adopting the $\nu P(\nu)$ representation (Fig. 2.5), specific frequencies characterised by enhanced power can be easily identified (typically around $\sim$ 0.1 Hz and 1 Hz). This gives the PSD a distinctive humped shape (e.g. Nowak 2000; Pottschmidt et al. 2003; Axelsson and Done 2018). If described in terms of Lorentzians (Belloni et al., 2002), the multi-peaked noise PSD of Cyg X-1 in the hard state can be decomposed as the

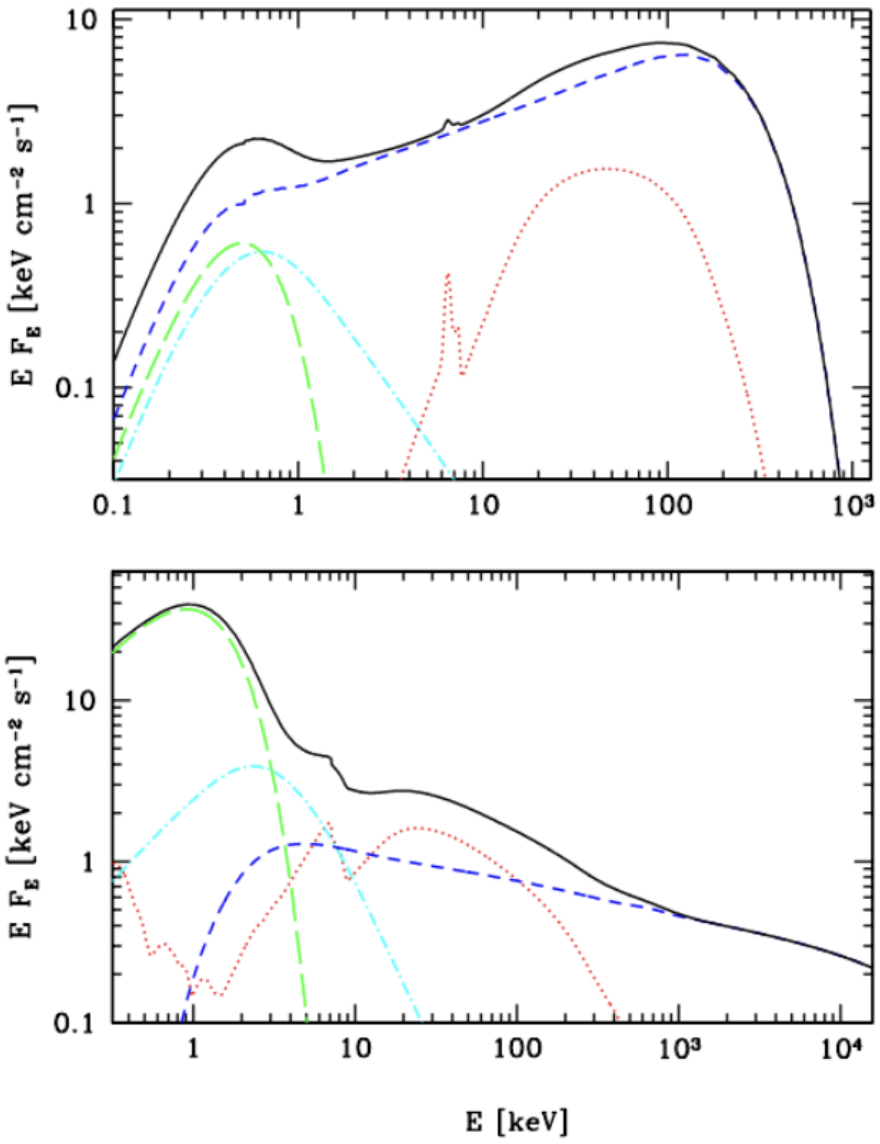


**Figure 2.3:** Main components characterising the X-ray spectrum of Cyg X-1 in the two spectral states. Upper panel: the hard state spectrum from an observation of *BeppoSAX* (Di Salvo et al. 2001). Bottom panel: the soft state spectrum from a multi-instrument observation of Cyg X-1 (McConnell et al. 2002). The total spectrum is shown in black. The blue dashed line represents the Comptonisation component. The red-dotted line represents the reflection component. The green long-dashed line represents the blackbody emission from the disc. The cyan dot-dashed curve represents the soft excess. Readapted from Zdziarski and Gierliński (2004).

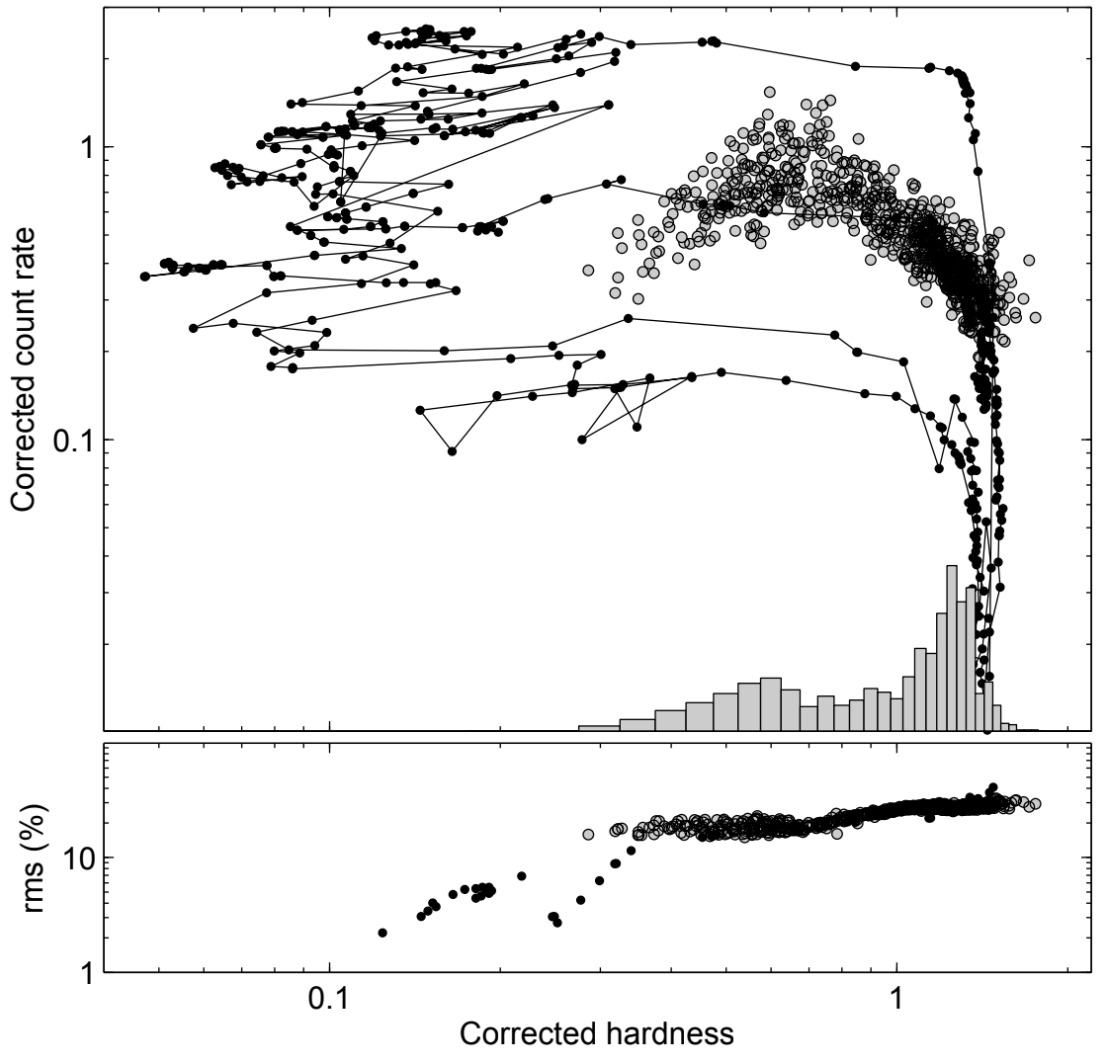


**Figure 2.4:** Upper panel: HID of 1065 Cyg X-1 *RXTE*/PCA observations ranging from February 1996 to October 2005 (grey shaded points) compared with the GX 339–4 monitorings of 2002/2003 and 2004/2005 (black points). Black points for GX 339–4 have been shifted to match the distance of Cyg X-1. The histogram shows the hardness values distribution. A second and softer peak is visible, correlated to the bend seen in the HID. However, no QPO (see Sect. 2.4) is found. Bottom panel: HRD of the same Cyg X-1 observations overplotted to a few observations of GX 339–4 from March 2002. From Belloni (2010a).

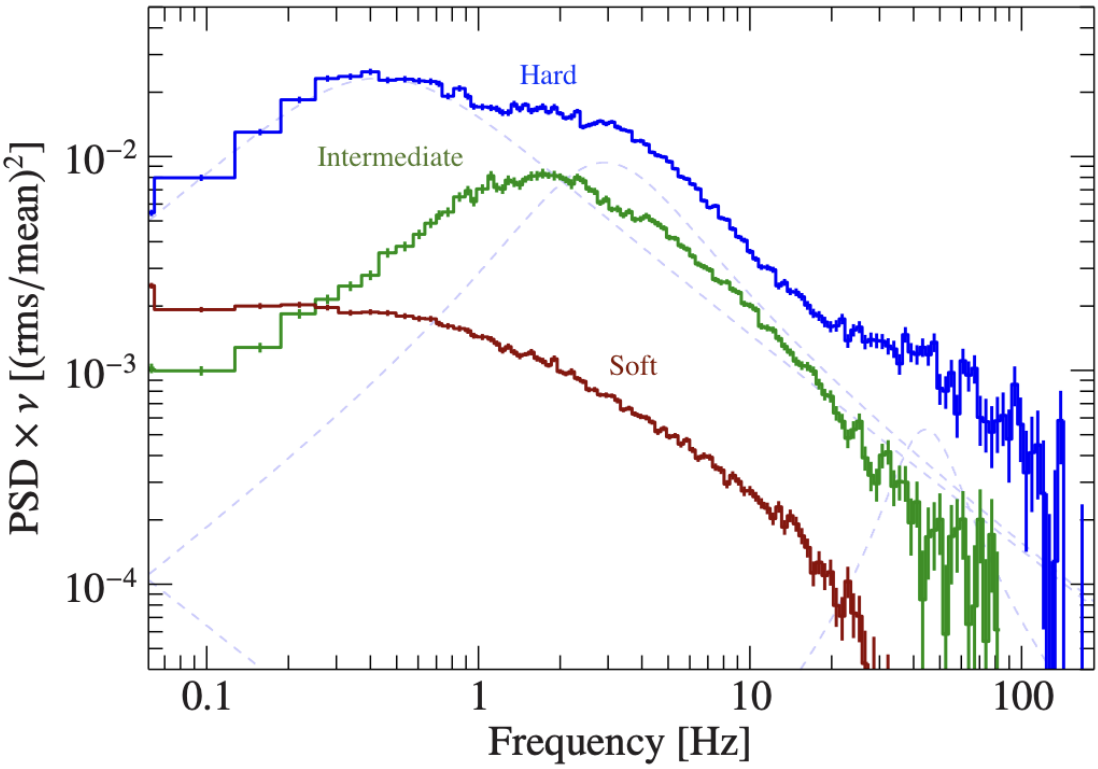


**Figure 2.5:** PSD of Cyg X-1 in the hard (blue), intermediate (green) and soft (brown) state for *NICER* observations (ID 2636010101, 0100320110 and 1100320122, respectively) in the 0.5–10 keV. Dashed lines represent the Lorentzian components. Readapted from König et al. (2024).

sum of up to four broad Lorentzian components (Nowak 2000; Pottschmidt et al. 2003; Palit et al. 2020; König et al. 2024), with a total fractional rms amplitude of about 30–35% between 0.001 and 100 Hz (Grinberg et al., 2014). When comparing disc-dominated bands with power law-dominated bands, the PSD reveals higher amplitude variability in the disc than in the power law component at low frequency ($\nu \lesssim 1$ Hz, König et al. 2024). On the contrary, at high frequencies the disc variability power drops.
Despite showing humps in its PSD, strong and narrow features that might be interpreted as a type–C QPOs are not clearly observed in Cyg X-1 contrary to the majority of the other BHXRBs (Motta et al., 2015).

As the source softens, the characteristic frequencies of the Lorentzian components in the PSD all shift to higher frequencies (Axelsson et al., 2005, 2006). When the source reaches its softest states the PSD can be described by a cut-off power law of slope $\nu^{-1}$, sometimes requiring the addition of a single broad Lorentzian at

high frequencies ($\gtrsim$ 3 Hz, Cui et al. 1997b,a; Axelsson et al. 2005, see Fig. 2.5). The total fractional rms amplitude drops to a few percent in the 0.5–3 keV band (Grinberg et al. 2014) while staying relatively high ($\sim$ 30%) at higher energies (Zhou et al. 2022). This behaviour is likely due to the increased contribution of the disc in the softer bands, which appears overall less variable than in harder states (Churazov et al., 2001), as also seen in other BHXRBs (De Marco et al., 2015b).

At $E > 1$ keV Cyg X-1 shows time lags of the harder bands with respect to the softer bands (both bands dominated by the Comptonisation component in the hard state) over all sampled frequencies, as also typical of other BHXRBs. The amplitude of the hard lags decreases as a function of temporal frequency as $\nu^{-\alpha}$ with $\alpha \sim 0.6$–$0.7$ (Nowak et al. 1999; Pottschmidt et al. 2000, panel b in Fig. 2.6). However, this trend is not smooth, but shows step-like features with characteristic frequencies apparently matching the frequencies of the Lorentzian components in the PSD (Nowak et al., 1999). Using XMM-Newton data, Uttley et al. (2011) showed that in the hard state, hard lags are also observed when correlating a soft band dominated by the disc, with a hard band dominated by the Comptonisation component. In the hard state a high level of linear correlation (i.e. coherence, Sect. 3.2.2, close to unity, Nowak et al. 1999) between all bands is generally observed, although a slight drop is sometimes seen at low temporal frequencies ($\nu \lesssim 0.1$ Hz, Fig. 2.7, Nowak et al. 1999). Higher complexities emerge when considering the lags and coherence between disc-dominated and power law-dominated bands. The hard lags strongly deviate from a $\nu^{-\alpha}$ profile, with a peaked feature appearing in the lag spectrum, and characterised by a sharp drop of coherence (König et al. 2024, Fig. 2.8). Intermediate states are characterised by an increase of the amplitude of the time lags measured between power law-dominated bands (Pottschmidt et al. 2000, panel a in Fig. 2.6), and a concurrent decrease of coherence (Grinberg et al. 2014). When the source reaches the soft state both the time lags and the coherence in power law-dominated bands return consistent with the values measured in the hard state (Pottschmidt et al. 2000; Grinberg et al. 2014). However, when considering a disc-dominated band versus a power law-dominated band, the observed variability in these two components appears highly incoherent (König et al., 2024), again pointing to a drastic change in the variability properties of the disc between hard and soft states.

## 2.5 The stellar wind

In the majority of HMXBs, the compact object directly accretes via the strong stellar wind emitted from the companion star surface (Bondi and Hoyle 1944, Sect. 1.2). Stellar winds of luminous and hot stars are composed of free elec-

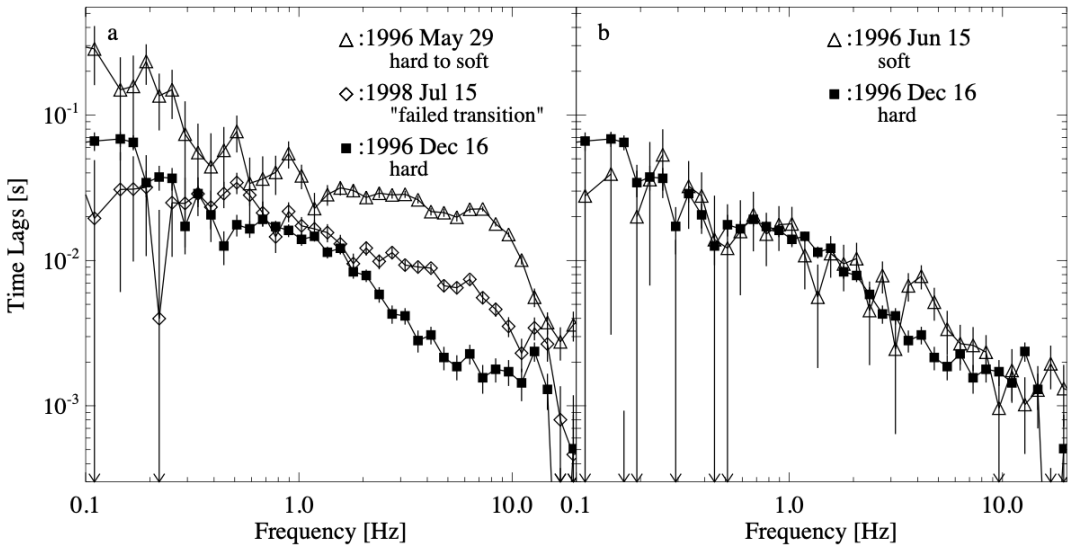


**Figure 2.6:** Time lags as a function of Fourier frequency of Cyg X-1 (8–13 keV relative to $\lesssim 4$ keV) for the *RXTE* monitoring campaign from 1996 to 1998 (Pottschmidt et al. 2000). Panel a: comparison of the lags for the soft to hard state transition. Panel b: comparison between the time lags in the hard and the soft spectral states. Taken from Pottschmidt et al. (2000).

trons, ionised hydrogen and other complex species of ionised atoms (Lamers and Cassinelli 1999). They are mainly driven by the transfer of momentum from the incident photons to the absorbing ions, which causes the ions to move away from the star. These winds are referred to as *line-driven* winds (hypothesised by Lucy and Solomon 1970 and theoretically described by Castor et al. 1975). The efficient launch of these winds requires high metallicity and a large number of incident photons, therefore they are expected to arise in the hottest O-like stars and in the cooler BA-supergiants due to their larger radii. Since these stars are hot and luminous, *line-driven* winds represent the standard model to describe accretion in HMXBs.

In *line-driven* winds, when a sufficiently energetic photon interacts with a heavy ion, it can excite a bound electron to a higher energy level. As a consequence, the photon gets absorbed. However, the electron can return to his original energy level, re-emitting the photon. The released kinetic energy is transferred to the heavy ion, generating a radiative acceleration in the stream. This mechanism can impart sufficient momentum to accelerate the stellar wind material, reaching terminal velocities up to 2500 km $s^{-1}$ (Martínez-Núñez et al. 2017). As a result, stellar winds are very fast and unstable (Lucy and Solomon 1970). Hydrodynamical simulations

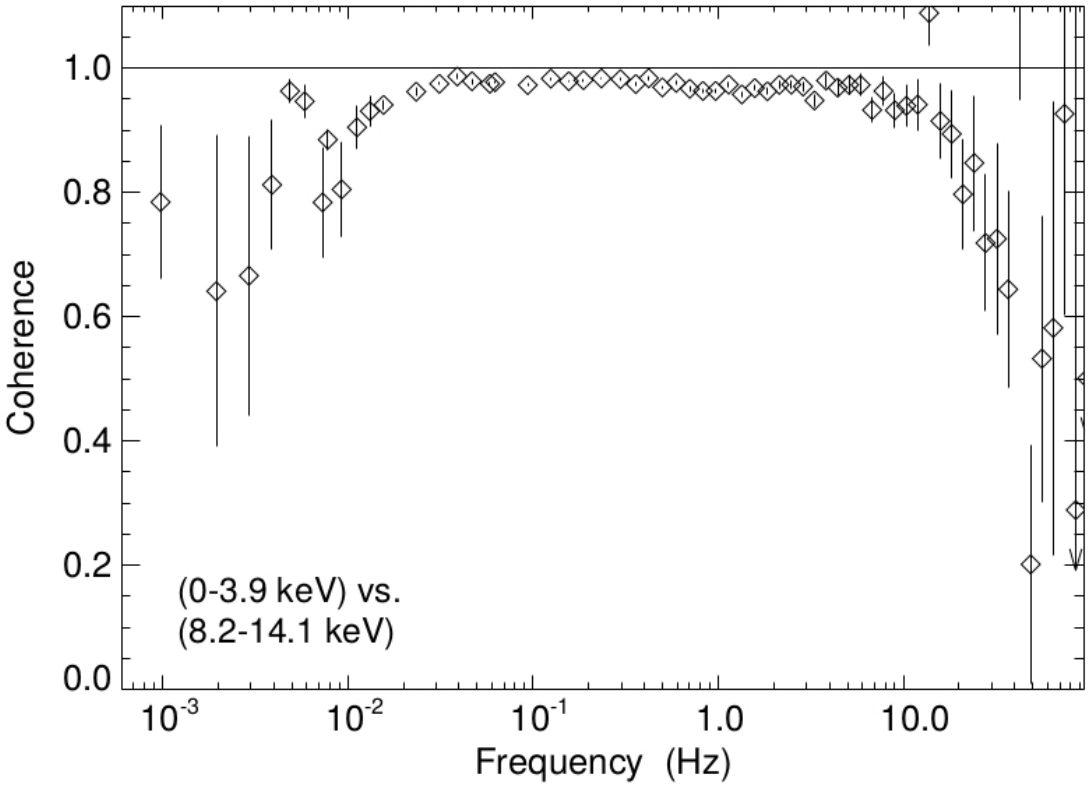


**Figure 2.7:** Intrinsic coherence versus frequency (8.2–14.1 keV relative to 0–3.9 keV) of Cyg X-1 in the hard state for the 1996 *RXTE* monitoring (Dove et al. 1999). From Nowak et al. (1999).

(Owocki et al. 1988; Feldmeier et al. 1997) showed that such instabilities can generate perturbations and create shocks able to enclose the wind material in highly-dense regions called clumps.
The inhomogeneous stellar wind strongly influences not only the estimates of the mass-loss rate (up to $10^{-5}\,M_{\odot}$ yr$^{-1}$, Puls et al. 2008; Martínez-Núñez et al. 2017), but also the spectral and timing properties of the X-ray source depending on the inclination of the system, the orbital phase of the compact object and the spectral state. To investigate the stellar wind properties, it is important that the X-ray source stays in its hard or intermediate spectral state. In fact, the X-ray emission in the soft state is strong enough to completely photoionise the wind, making it transparent to X-rays. The wind may be even getting suppressed in this way, because the radiative driving force of the UV photons from the donor star is reduced (given that the gas is transparent also to the UV radiation from the star).

In Cyg X-1, the centrifugal forces and the tidal interactions between the companion star and the BH make the wind asymmetric close to the binary axis, in-

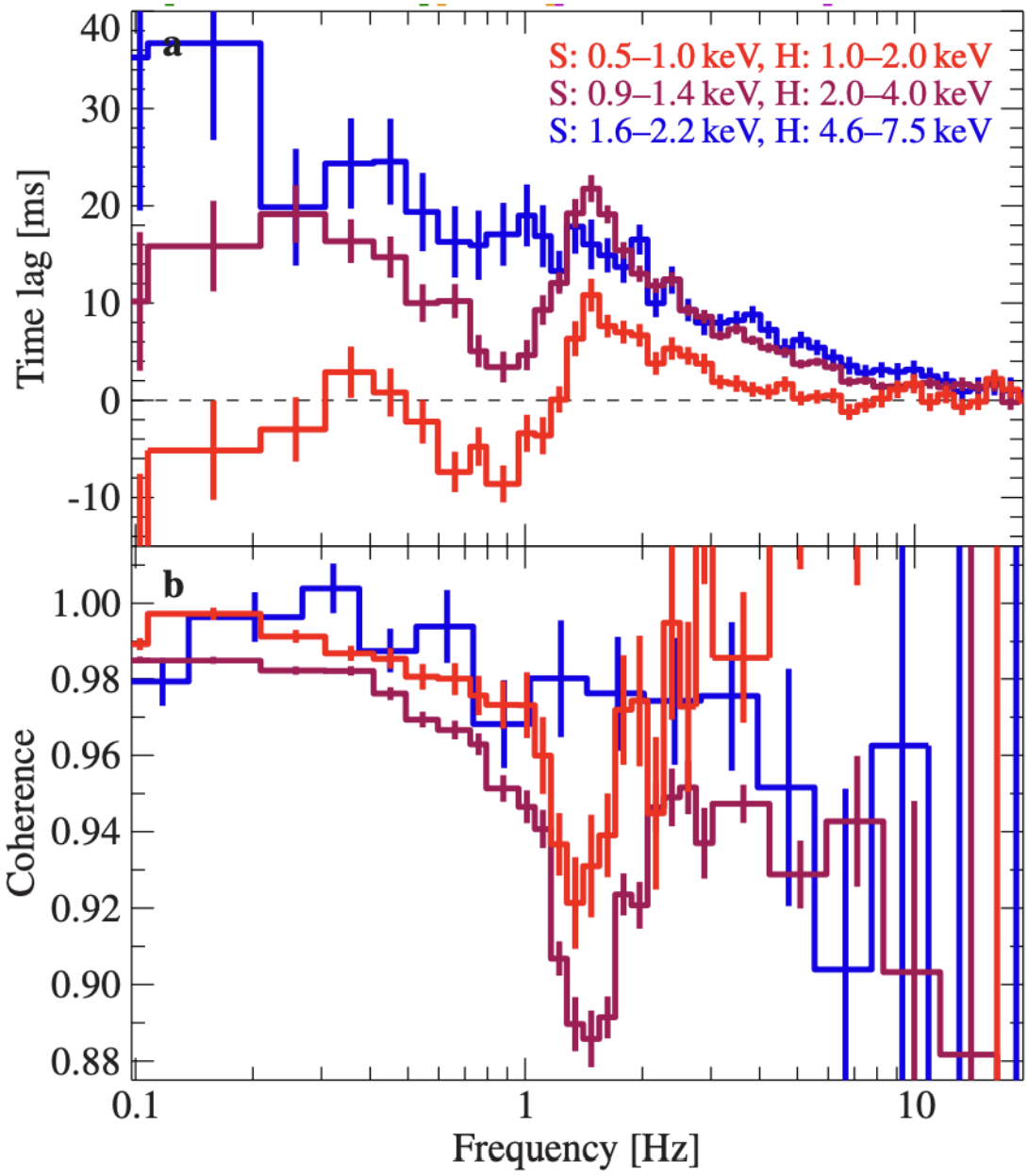


**Figure 2.8:** Time lags and intrinsic coherence vs frequency of Cyg X-1 during its hard state observed by *NICER* in 2017 (observation ID 2636010101) in different energy bands.

creasing its density and its mass loss rate (Friend and Castor, 1982). Since the Roche lobe of HDE 226868 is almost filled (Bolton, 1975; Gies and Bolton, 1986), with a Roche lobe filling factor $f_{RL} \sim 0.96$ (Miller-Jones et al., 2021), the stellar

wind starts to stream towards the BH, forming an extremely focussed wind component (Friend and Castor, 1982). The presence of this component is confirmed by the modulation of absorption and emission features along the orbit in the optical band (Gies et al., 2003). The focussed wind allows the formation of a small disc by which the accretion occurs. However, the presence of the accretion disc (see Sect. 1.3.1 and Sect. 2.3) in Cyg X-1 is an exception. In fact, wind accretion (Bondi and Hoyle, 1944) does not involve the presence of an accretion disc (Frank et al. 2002) around the compact object in the majority of HMXBs (e.g. Vela X-1, Blondin et al. 1991, and SCM X-1, Blondin 1994; Blondin and Woo 1995).

Cyg X-1 is one of the best X-ray source to investigate the stellar wind structure. In fact, due to the orbital inclination of the system ($i \sim 27°$, Miller-Jones et al. 2021), the line-of-sight (LOS) can intercept the clump forming region, likely located close to the HDE 226868's photosphere (El Mellah et al., 2020). This happens at superior conjunction ($\phi_{orb} = 0$). In this position, the companion star is the closest to the observer along the orbit, thus the BH is the farthest (see Li and Clark 1974 and references therein). Therefore, in these phases it is possible to probe deeper wind layers, where the clumps are smaller and slower. At inferior conjunction ($\phi_{orb} = 0.5$), the companion star is the farthest from the observer along the orbit, and the BH is the closest. Here, the LOS intercepts the external layers, when the wind has reached its terminal velocity and the clumps had the opportunity to grow to their maximal size. Therefore, depending on the position of the orbit also the X-ray photons undergo different levels of absorption depending on the amount and state of ionisation of wind material intercepting the LOS. Stellar wind absorption strongly affects the softest energy bands, at energies $E < 1\,\mathrm{keV}$ (Fig. 2.9), causing drops of X-ray flux, but it also shows milder effects at $E \sim 10\,\mathrm{keV}$, Grinberg et al. 2015; Hirsch et al. 2019). An immediate consequence of the presence of these winds is the presence of dipping events in the X-ray light curves as well as in the hardness ratios (i.e. ratios of count rates between a hard and a soft energy band) of the source, being more intense and frequent at superior conjunction (see Fig. 2.10, Bałucińska-Church et al. 2000; Hirsch et al. 2019).

## 2.6 Motivation of the thesis

In this thesis we present a comprehensive X-ray variability study of the stellar wind in Cyg X-1, with the aim of inferring the effects of the wind on the observed temporal properties of the X-ray source, and ultimately constraining the physical properties of the wind clumps (e.g. size, mass loss rate, etc.). Stellar winds are indeed an important and yet poorly understood component in this type of systems: not only can they significantly modify our view of the emission coming from the innermost regions of the accretion flow, but they are also expected to strongly

influence the evolution of both the donor star and the binary system (e.g. angular momentum loss through the wind can cause modifications of the orbit, possibly leading to merging events). Given that the absorption events induced by the passage of single wind clumps can be quite short ($\lesssim$1 ks), the use of standard time-resolved spectroscopic techniques is currently limited by the quality of available data. To deal with this limitation, before larger collective area detectors will become available, we explored alternative analysis approaches which make use of X-ray spectral-timing techniques and colour-colour diagrams. These techniques, as well as the data we used for the analysis (from an extensive monitoring campaign of Cyg X-1 performed with XMM-Newton) are described in detail in the following chapter. Results obtained from the application of these techniques are reported in Chapters 4 and 5.

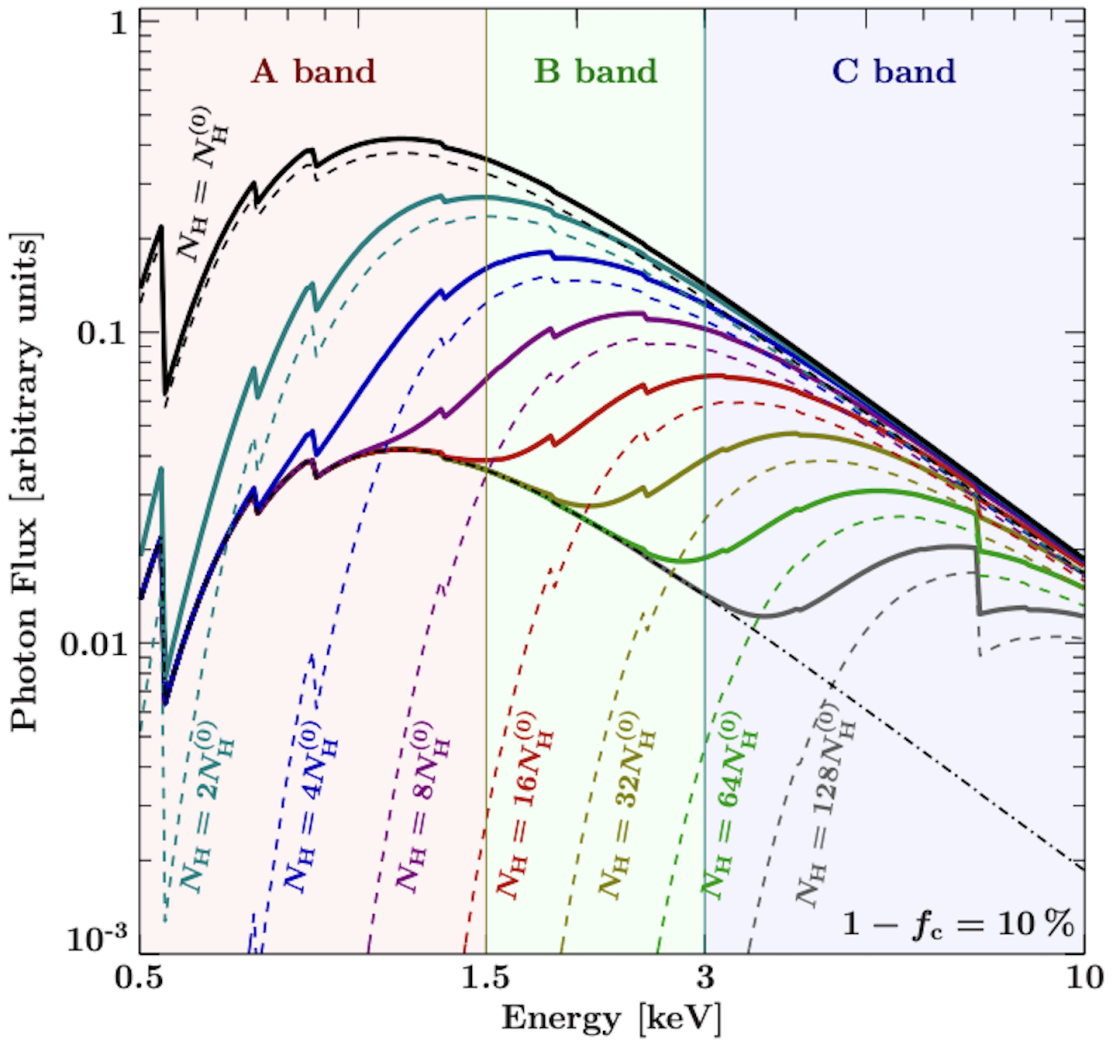


**Figure 2.9:** Effects of wind absorption on the spectrum of Cyg X-1, assuming a partial covering model. The spectra show the changes expected for increasing values of wind column density (with $N_H{}^{(0)} = 5.4 \times 10^{21} \mathrm{cm}^{-2}$, see Hanke et al. 2009) and constant coverage (90%). Bands A, B and C reported on top correspond to $0.5 - 1.5\,\mathrm{keV}$, $1.5 - 3\,\mathrm{keV}$ and $3 - 10\,\mathrm{keV}$, respectively. See Fig. 3.2 for the corresponding colour-colour diagram. From Hirsch et al. (2019).

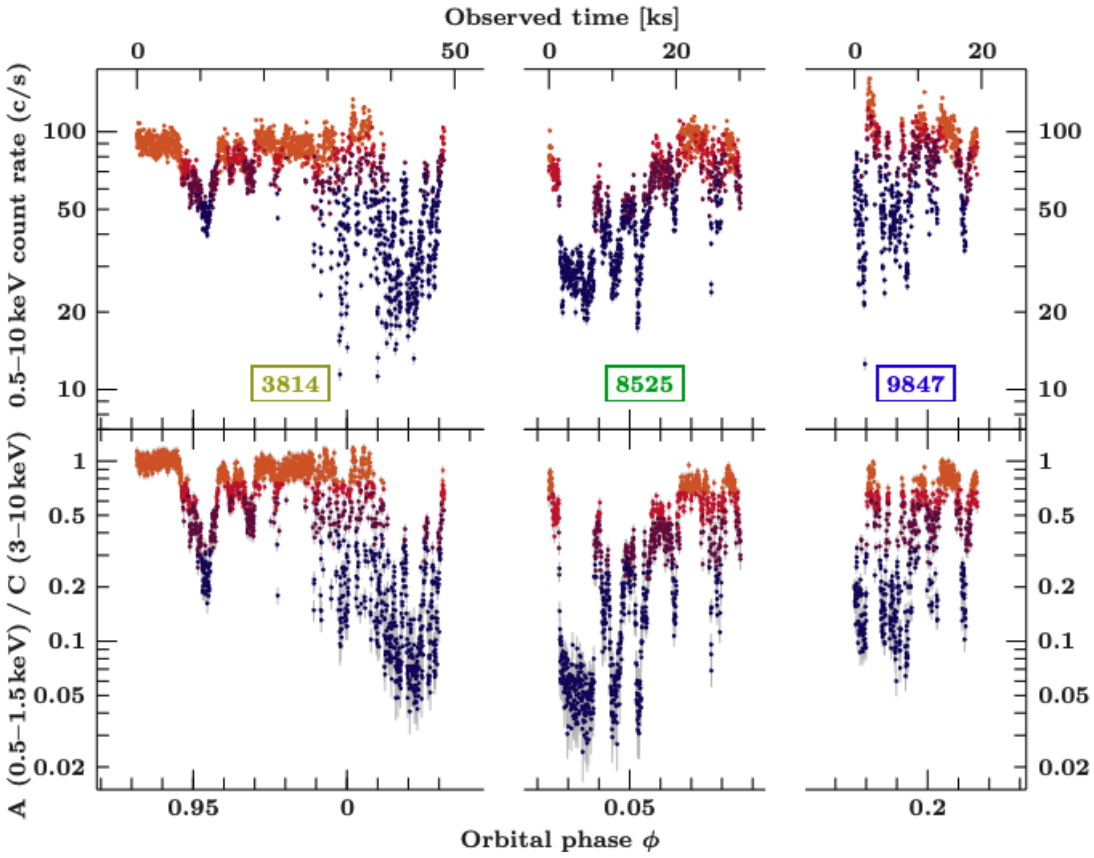


**Figure 2.10:** *Chandra* light curve of observations 3814, 8525 and 9847 of Cyg X-1 with time bins of 25 s in the 0.5–10 keV energy band (upper panel). Hardness, i.e. ratio between count rates in 3–10 keV and 0.5–1.5 keV energy bands (bottom panel). Shaded colours from orange to deep blue indicate different dipping stages (from non-dip to strong dip, accordingly to figure 3 of Hirsch et al. 2019). From Hirsch et al. (2019).

# Chapter 3

# The X-ray data and the analysis techniques

## 3.1 The *XMM-Newton* CHOCBOX monitoring

Cyg X-1 has been the target of a unique multi-wavelength campaign: the "Cyg X-1 Hard state Observations of a Complete Binary Orbit in X-rays" (CHOCBOX), covering energy ranges from radio to gamma rays, with the goal of studying all the physical components of the system, including the accretion disc, the corona, the stellar wind and the jet. The campaign was carried out between May and June 2016, when the source was in a hard state. Several instruments such as *XMM-Newton*, *NuSTAR*, *INTEGRAL* and ground based interferometers (including *NOEMA*, *VLA*, and *VLBA*) observed the source simultaneously. The source stayed in hard state for the entire campaign.

The main observatory of the CHOCBOX campaign is *XMM-Newton* (X-ray Multi-Mirror Mission, XMM 2024). The European Space Agency's (ESA) satellite was launched on December 10, 1999 by an Ariane 5 launcher in a highly elliptical, 40-degree orbit (with an apogee of 114000 km and a perigee of 7000 km).
*XMM-Newton* is composed of three X-ray telescopes consisting of 58 Wolter-I type grazing incidence mirrors, nested in a coaxial and co-focal configuration. The telescopes' focal length is of 7.5 m and the largest mirrors have a diameter of 70 cm. Two mirror modules are equipped with two Reflection Grating Spectrometers (RGS) which intercept half of the incident photons. The other half of the incident beam is focussed onto the two European Photon Imaging Cameras (EPIC) MOS (Metal Oxide Semi-conductor) cameras. The third module is focused directly onto the EPIC-pn camera. Additionally, *XMM-Newton* carries onboard an Optical/UV Monitor (OM) telescope positioned next to the X-ray mirror modules. The EPIC cameras are the primary instruments of *XMM-Newton*. They are able

to perform sensitive imaging over 30′ field of view (FOV) between 0.1 and 15 keV. With an angular resolution of 6″ full-width half maximum (FWHM), they reach a spectral resolution of $E/\delta E \sim$ 20–50. While the EPIC MOS cameras are composed of seven charge-coupled devices (CCD), each containing a matrix of $600 \times 600$ pixels, the EPIC-pn is an array of twelve CCDs made of $64 \times 200$ pixels each.
The two RGS, mounted below two of the mirror modules, have a spectral resolution $E/\delta E \sim$ 200–800 and deflect about half of the X-ray photons onto nine of the EPIC MOS CCDs. The OM telescope covers the 180–650 nm range over 17′ FOV, permitting observations of the X-ray targets also in the Optical and UV band.
Therefore, in total, *XMM-Newton* counts six instruments that can observe simultaneously. The CHOCBOX monitoring comprises observations of Cyg X-1 performed by the EPIC-pn camera in timing mode, offering the possibility to study bright sources at very high time resolution (i.e. $\sim 30\mu s$). Given its high throughput and high time resolution, data from the EPIC-pn instrument were used for the analysis presented in this thesis.

The *XMM-Newton* EPIC-pn camera observed Cyg X-1 between 2016 May 27 and June 2, for a total duration of 7.22 d (Uttley 2017). Therefore, the monitoring covers $\sim$ 1.5 orbits of the system. This unprecedent uninterrupted campaign covers two passages at superior conjunction.
The *XMM-Newton* monitoring is composed of four observations. The observation identification numbers (ObsIDs) are reported in Tab. 3.1 with the corresponding exposures. The orbital phase coverage of the monitoring are also reported in Tab. 3.1 and schematically shown in Fig. 3.1.

**Table 3.1:** Log of the CHOCBOX *XMM-Newton* EPIC-pn monitoring. The total exposure after regular data screening and the orbital phases $\phi$ covered for each observation. The bold-style digits of each ObsID identify each observation hereafter. Orbital phases were computed using the ephemeris reported in Gies et al. (2008).

| ObsID | Date (yyyy-mm-dd) | Total exposure (ks) | $\phi$ |
|---|---|---|---|
| 0745250**201** | 2016-05-27 | 92.9 | 0.82-0.06 |
| 0745250**501** | 2016-05-29 | 83.1 | 0.17-0.46 |
| 0745250**601** | 2016-05-31 | 76.7 | 0.53-0.79 |
| 0745250**701** | 2016-06-02 | 84.6 | 0.89-0.11 |

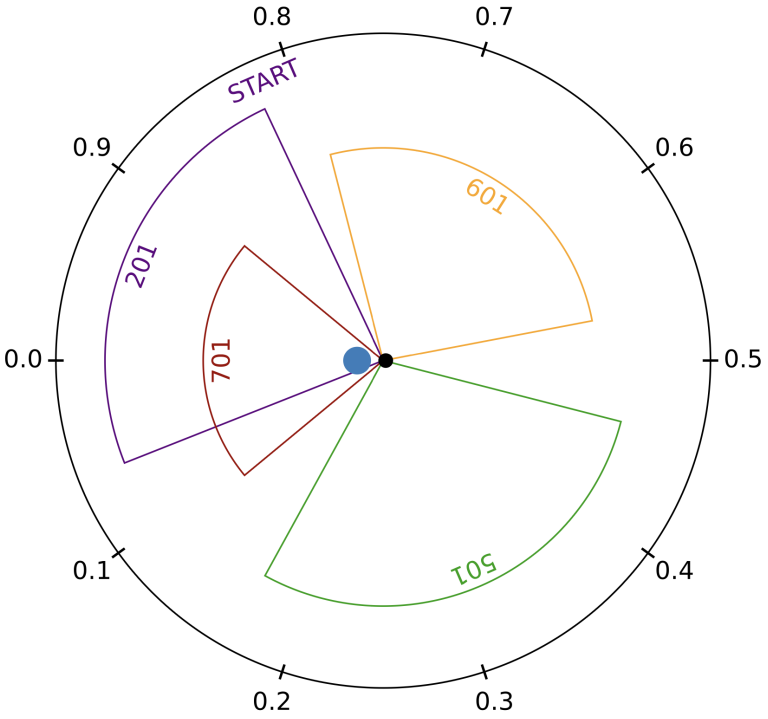


**Figure 3.1:** Orbital phase coverage of the *XMM-Newton* CHOCBOX monitoring. The four coloured arc labels correspond to the ObsIDs of each pointing (Tab. 3.1). The orbital phase $\phi_{\mathrm{orb}} = 0$ indicates the passage at superior conjunction. Inferior conjunction corresponds to orbital phase $\phi_{\mathrm{orb}} = 0.5$. The "START" indicates the starting orbital phase of the entire campaign at $\phi = 0.82$. Cyg X-1 and HDE 226868 are only schematically graphed, the Roche lobe was not considered in the representation.

## 3.2 Fourier timing techniques

X-ray variability is one of the defining properties of BH-accreting systems. As described in Sect. 1.4, X-ray variability is a powerful tracer of the accretion state of a BHXRB. Therefore, the study of X-ray variability is of the utmost importance in order to gain a complete understanding of the accretion process. Many tools are available to analyse flux time series (Belloni and Bhattacharya, 2022), but when it comes to single out variability on different timescales, thus produced at different distances from the BH, Fourier techniques turn out to be more handy. This thesis focuses on the study of the fastest (shorter than 10 s) X-ray variability of Cyg X-1, thus it will make use of a series of Fourier techniques, as described below. The outlined techniques have been implemented using Python. We made use of the main Python scientific libraries such as Numpy (van der Walt et al., 2011), Astropy (Astropy Collaboration et al., 2013) and SciPy (Virtanen et al., 2020) to compute the main Fourier products. In particular, we developed codes able to compute the PSD and the cross-spectral analysis products, as well as colour-colour diagrams. Particular SciPy classes were used to perform colour-colour diagram fits (Sect. 5.3.3). Additionally, with Python's library, Matplotlib (Hunter, 2007), we developed codes able to plot the results.

### 3.2.1 Power spectrum

The power spectrum, or PSD, measures the amount of variability power as a function of temporal frequency. For a discrete and evenly (at intervals $\Delta t$) sampled time series of fluxes $x_i$ measured at times $t_i$ (with $i = 1, 2, ..., N$), we can compute the Discrete Fourier Transform (DFT) $X_n$ as:

$$X_n = \sum_{k=0}^{N-1} x_k \exp(2\pi i n k/N) \tag{3.1}$$

where $f_n = n/T$ is the Fourier frequency (being $T$ the total duration of the time series, i.e. $T = N\Delta t$), and $n = 1, 2, ...N/2$. The minimum frequency is defined as $f_{min} = 1/T$ and the maximum frequency, namely the *Nyquist* frequency, as $f_{max} = 1/(2\Delta t)$. Note that the DFT is a complex number.
The modulus squared of the DFT defines the periodogram, which is an estimate of the PSD. Therefore, the power $P_n$ at a frequency $f_n$ is:

$$P_n = A\ |X_n|^2 = A\ X_n^* X_n \tag{3.2}$$

where the asterisk denotes the complex conjugate, and $A$ is a normalisation factor. Different normalisations can be used, depending on the type of information we want

to obtain (see Appendix A of Vaughan et al. 2003 for details). In this thesis we will make use of the *fractional* rms-squared normalisation (Belloni and Hasinger 1990), defined as:

$$A_{rms} = \frac{2\Delta t}{\overline{x}^2 N} \tag{3.3}$$

This normalisation yields the PSD in units of $(rms/mean)^2 \mathrm{Hz}^{-1}$, therefore integration of the PSD over a given frequency interval and extraction of the square root gives an estimate of the fractional contribution to variability ($F_{var}$) over the corresponding range of timescales.

Photon counting produces a Poisson noise contribution (white noise) which flattens the PSD at high frequencies. The normalisation of the Poisson noise contribution depends on the count rate. Assuming the *fractional* rms-squared normalisation the expected Poisson noise level for a time series of contiguous time bins and in the absence of deadtime[1] is:

$$P_{noise} = \frac{2(\overline{x} + \overline{b})}{\overline{x}^2} \tag{3.4}$$

where $\overline{b}$ is the mean background count rate, to be accounted for if the estimated background count rates have been subtracted from the time series. If the background has not been subtracted or is negligible, this reduces to $P_{noise} = 2/\overline{x}$. An alternative way to estimate the Poisson noise contribution in order to extract the intrinsic variability power of the source is by fitting a constant to the PSD at very high frequencies, in the region where the PSD flattens. The latter approach is the one used in this thesis.

The PSD calculated from a single light curve yields large statistical uncertainties (van der Klis, 1989; Vaughan et al., 2003). In order to reduce the errors and obtain a better estimate of the intrinsic PSD, the latter must be binned over a large number of light curve segments and/or frequencies. The resulting PSD in the frequency bin ${\nu_j}^2$ is given by:

$$\overline{P}(\nu_j) = \frac{1}{KM} \sum_{n=i}^{i+K-1} \sum_{m=1}^{M} P_{n,m} \tag{3.5}$$

where $M$ is the number of different light curve segments, and $K$ is the number frequencies within $\nu_j$. The scatter in the binned PSD decreases as:

$$\Delta\overline{P}(\nu_j) = \frac{\overline{P}(\nu_j)}{\sqrt{KM}} \tag{3.6}$$

[1]The fraction of the exposure during which the detector cannot register events.

[2]Note that the $\nu_j$ indicates the frequency bin, to be distinguished from the single frequencies $f_n$.

### 3.2.2 Cross-Spectral methods

The causal relationship between two time series (e.g. extracted in two energy bands dominated by different spectral components) can be estimated via cross-spectral analysis. Considering two light curves $x(t)$ and $y(t)$ in two different energy bands, and their DFTs $X_n$ and $Y_n$, the Fourier cross-spectrum between the two is defined as:

$$C_{XY,n} = X_n^* Y_n \tag{3.7}$$

Analogously to the PSD, the cross-spectrum must be averaged over $K$ Fourier frequencies in a given frequency bin (i.e. $\nu_j$) and over $M$ multiple light curve segments:

$$\overline{C}_{XY}(\nu_j) = \frac{1}{KM} \sum_{n=i}^{i+K-1} \sum_{m=1}^{M} C_{XY,n,m} \tag{3.8}$$

and normalised in the same way as the PSD (Sect. 3.2.1), only with the exception of dividing by $\overline{x}\,\overline{y}$ instead of $\overline{x}^2$, to obtain fractional rms-squared units.
The cross-spectrum is a complex quantity, whose argument gives the relative phase lag between the two time series (Uttley et al., 2014):

$$\phi(\nu_j) = \arg[\overline{C}_{XY}(\nu_j)]. \tag{3.9}$$

and defined in the interval $[-\pi, \pi]$. An estimate of the corresponding time lag is given by:

$$\delta t(\nu_j) = \frac{\phi(\nu_j)}{2\pi\nu_j} \tag{3.10}$$

In this thesis time lags are computed between softer and harder energy bands. We will adopt the convention according to which a positive lag indicates a time delay of the harder band variations with respect to the softer band variations (hard lag), and a negative lag indicates a time delay of the softer band variations with respect to the harder band variations (soft lag).

From the cross-spectrum, it is possible to obtain an estimate of the coherence, a measure of the degree of linear correlation between two light curves (Nowak et al. 1999). The coherence is defined as:

$$\gamma^2 = \frac{|\overline{C}_{XY}(\nu_j)|^2 - n^2}{\overline{P}_X(\nu_j)\overline{P}_Y(\nu_j)} \tag{3.11}$$

where the PSD and the cross-spectrum are normalised in the same way. The term $n^2$ in the numerator is a bias term, directly linked to the contribution of the Poisson noise level to the modulus-squared of the cross-spectrum[3]. Ingram (2019)

[3]The bias term is defined as $n^2 = [(\overline{P}_X(\nu_j) - P_{X,noise})P_{Y,noise} + (\overline{P}_Y(\nu_j) - P_{Y,noise})P_{X,noise} + P_{X,noise}P_{Y,noise}]/KM$ where $P_{noise}$ is the Poisson noise level affecting the particular light curve. See Vaughan and Nowak (1997) for further details on this term.

demonstrated that this term becomes negligible when averaging over $KM \gtrsim 500$. This condition always holds for the data considered in the presented analysis, thus the bias term was discarded.
By definition, the coherence can take only values comprised between 0 (for no coherent signals) and 1 (for fully coherent signals). The presence of Poisson noise has the effect of decreasing the coherence, so that the coherence of noisy data is always less than unity. However, the effect of Poisson noise can be corrected for and the *intrinsic* coherence (as opposed to the *raw* coherence of Eq. 3.11) can be estimated. Vaughan and Nowak (1997) provide recipes for estimating the value and uncertainty of the intrinsic coherence. In this thesis, their Eq. 8 is used to estimate the *intrinsic* coherence.

## 3.3 Colour-colour diagram

Colour-colour diagrams can be used for various purposes. For example, they are useful for classifying NS LMXBs into Z or Atoll sources (Hasinger and van der Klis, 1989). In this thesis, colour-colour diagrams are used to investigate the time-resolved spectral behaviour of Cyg X-1 and identify time intervals affected by the stellar wind.
The "colour" is defined as the ratio of count rates in two energy bands. The two axes of a colour-colour diagram each report a given colour. In general, a soft colour is defined as the ratio of the count rates in a soft and an intermediate energy band, while a hard colour is defined as the ratio between count rates in the same intermediate band and a hard energy band. The choice of the energy bands depends on the energy covered by the available data. Most studies of the stellar wind of Cyg X-1 have been performed using *Chandra* data (e.g. Hanke et al. 2008; Nowak et al. 2011; Hirsch et al. 2019. Being the twin mission of *Chandra*, *XMM-Newton* covers the same energies, thus it is possible to define the colours considering the same energy bands used in the literature. Colour-colour diagram shapes depend on the response matrix of the instrument. However, *XMM-Newton* and *Chandra* have a similar effective area, thus the difference would be negligible. In this thesis, the following energy bands will be used to extract colour-colour diagrams from the *XMM-Newton* data of Cyg X-1: $E = 0.5 - 1.5\,\mathrm{keV}$ (soft), $E = 1.5 - 3\,\mathrm{keV}$ (intermediate), and $E = 3 - 10\,\mathrm{keV}$ (hard).
In HMXBs the presence of absorption from the stellar wind gives the colour-colour diagrams a characteristic "nose" shape (e.g. Nowak et al. 2011; Grinberg et al. 2020). This shape is due to the occurrence of dipping events, which cause absorption of soft X-rays, and thus a hardening of the spectrum (see Fig. 2.9).
Fig. 3.2 shows the colour-colour diagram for an absorber partially covering the X-ray source. For different values of column density and covering factor, the

colour-colour diagram follows different trends, extending down to the lower-left region (low hard and soft colours) when covering factor is higher (e.g. 90%).

It is worth noting that the colour-colour diagram shows an overall "zig-zag" shape when including data from intermediate and soft states (König et al., 2024). In this representation of the time-resolved spectral behaviour of Cyg X-1 across different states, the hard state covers the lower track of the diagram (see Fig. 3.3).

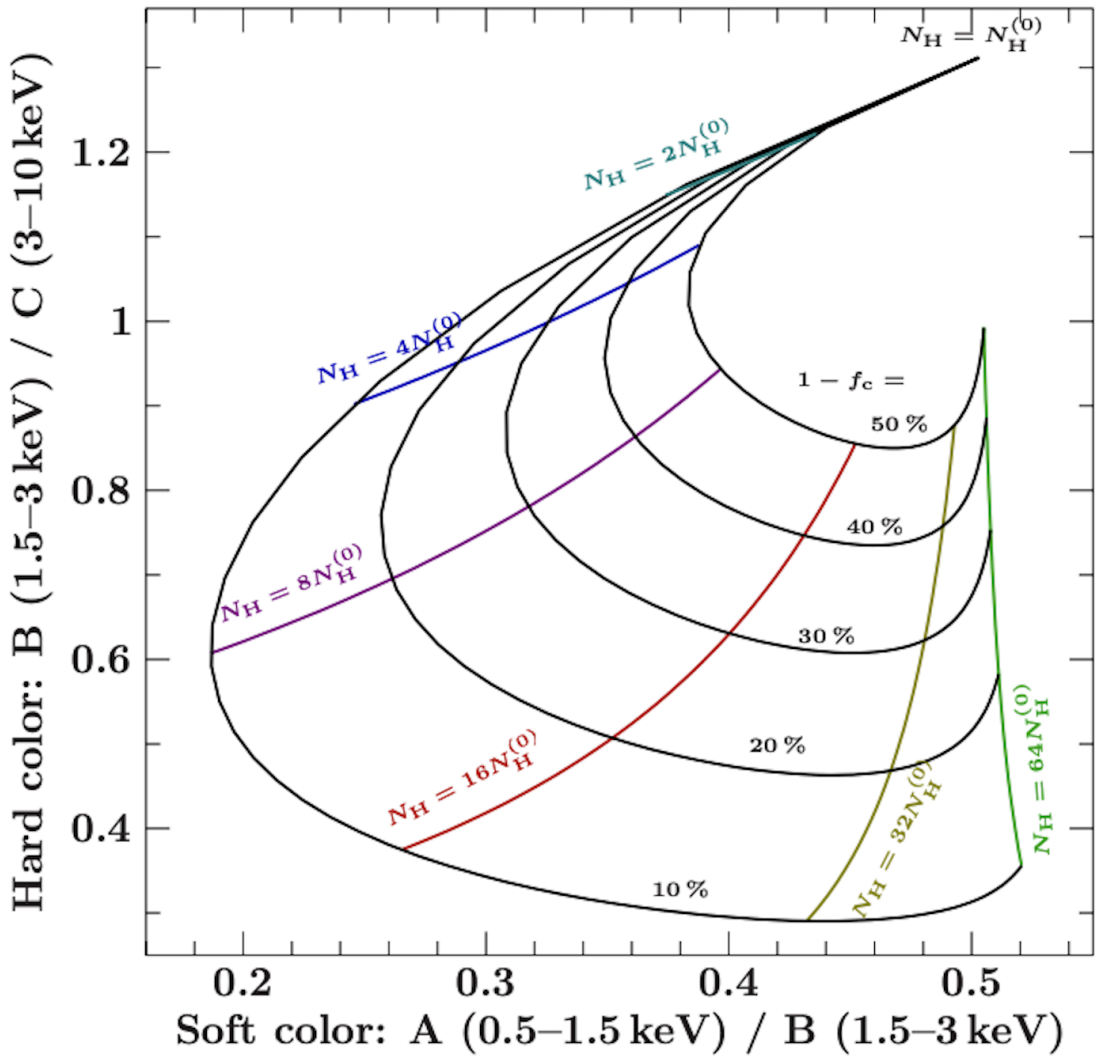


**Figure 3.2:** Colour-colour diagram tracks of a partial covering absorber (from 50% to 10% not covering the X-ray source) for different column density values starting from $N_H^{(0)} = 5.4 \times 10^{21} cm^{-2}$ (see Hanke et al. 2009). From Hirsch et al. (2019).

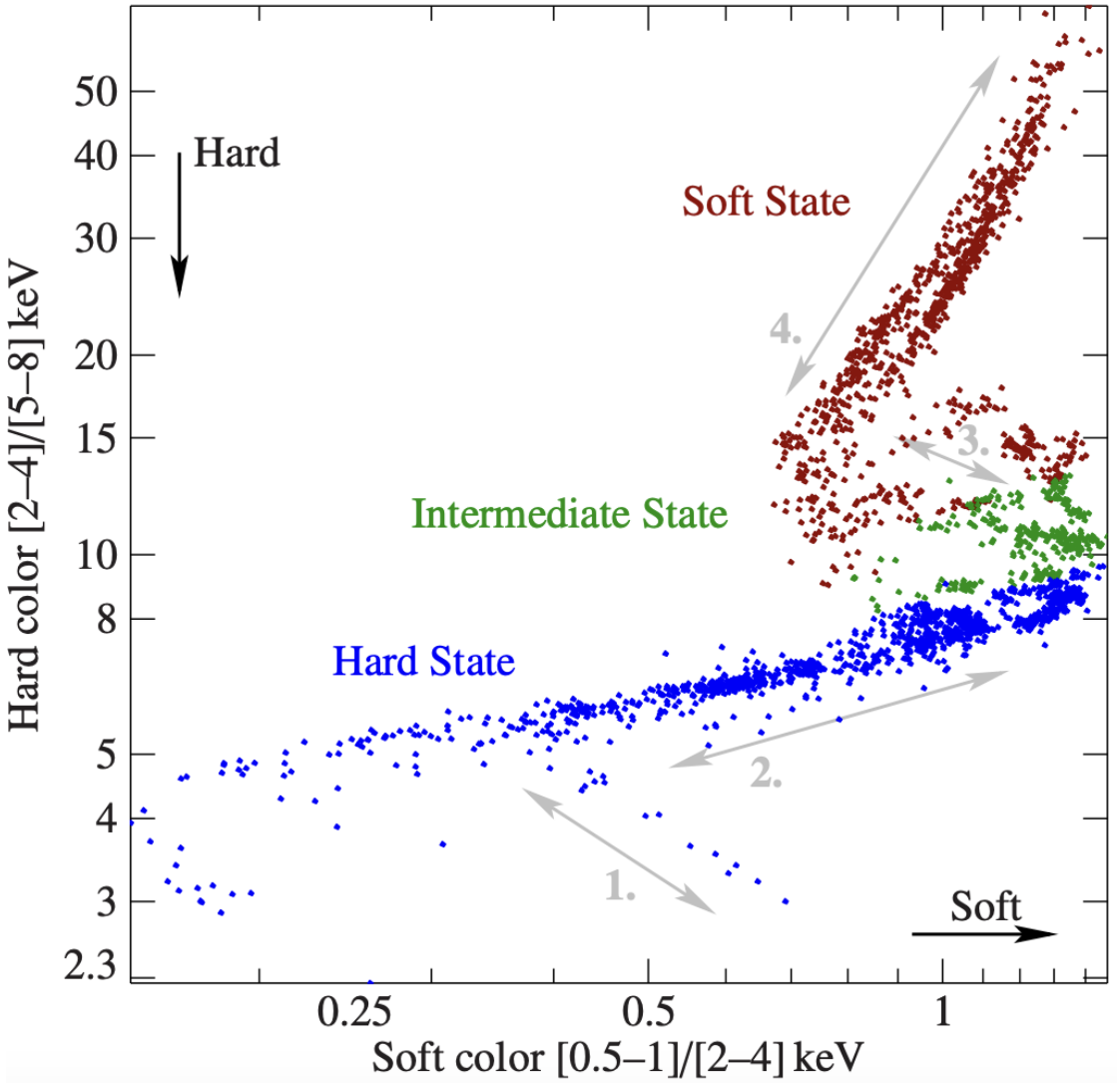


**Figure 3.3:** Colour-colour diagram of Cyg X-1 for different spectral states of the source. Grey arrows indicate the preferred paths followed by the source when transitioning. From König et al. (2024).

# Chapter 4

# A X-ray spectral-timing study of the stellar wind in the hard state of Cyg X-1

This chapter describes the study reported in the published paper "The X-ray spectral-timing contribution of the stellar wind in the hard state of Cyg X-1"[1] (Lai et al. 2022, Monthly Notices of the Royal Astronomical Society, Volume 512, Pages 2671–2685).

## 4.1 Introduction

The X-ray spectral and timing properties of BHXRBs dramatically change as the source transition between different accretion states (Sect. 1.4), likely as a consequence of major changes in the physical properties of the inner accretion flow (Gilfanov, 2010). Although the phenomenology of these states is well studied, the physics behind them is still largely debated. Cyg X-1 is amongst the best studied X-ray sources (Sect. 2.1), providing crucial information on the spectral and timing properties of BHXRBs as a class.

As commonly seen in BHXRBs, Cyg X-1 shows a complex frequency dependence of its variability power in the X-ray band during the hard state, drastically changing to a smoother dependence in the soft state (see Sect. 2.4, e.g. Nowak et al. 1999; Pottschmidt et al. 2000, 2003; Axelsson et al. 2005; Böck et al. 2011; Grinberg et al. 2014). Additionally, we regularly observe highly coherent hard ($E \gtrsim 1\,\mathrm{keV}$) and soft ($E \lesssim 1\,\mathrm{keV}$) X-ray band variations. Hard lags are associated with these variations, whereby hard photons are delayed with respect to the soft

[1] https://doi.org/10.1093/mnras/stac688

ones, with a delay of the order of 1% the variability timescale (e.g. Nowak et al., 1999; Grinberg et al., 2014).

An important additional component to consider when studying Cyg X-1 is the stellar wind (see Sect. 2.5 for a detailed description). The stellar wind significantly affects the observed X-ray spectrum via absorption. Moreover, the motion of stellar wind clumps across our LOS results in significant X-ray variability, as clearly seen in the light curves of the source (e.g. Hanke et al., 2008, 2009; Grinberg et al., 2015; Hirsch et al., 2019; Zhou et al., 2022; König et al., 2024). Therefore, it is plausible that the stellar wind can significantly influence the observed X-ray spectral-timing properties of the source (El Mellah et al., 2020). Since the timescales associated with wind variability have been shown to be of the order of minutes or shorter for the smallest clumps (Grinberg et al., 2017; Hirsch et al., 2019), this component may significantly affect the fast variability characteristics of the source. On the other hand, the X-ray spectral-timing signatures of the most wind-absorbed phases can be a powerful diagnostic of the physical properties of the absorbing gas (e.g. Grinberg et al., 2015; Silva et al., 2016; De Marco et al., 2020; El Mellah et al., 2020).

In this work, we analysed the *XMM-Newton* CHOCBOX monitoring (Sect. 3.1) with the main purpose of studying how the variable stellar wind in Cyg X-1 can modify the X-ray spectral-timing properties of the source during its hard state.

## 4.2 Data Reduction

We analysed all the four *XMM-Newton* observations of the CHOCBOX campaign (see Sect. 3.1). The observations were all acquired in timing mode. The total exposure is 572 ks before data screening (Tab. 3.1). We performed the data reduction using the *XMM-Newton* `Science Analysis Software` (`SAS`, version 16.9.0), following standard procedures and using calibration files (CCF) as of 2019 June. We extracted 1 s time-resolution light curves in the 10–15 keV energy band, where the response of the instrument drops, to identify and filter out time intervals affected by high particle background. However, no background flares were found in the entire data set. Nonetheless, the data are affected by telemetry drop-outs. These are periods characterised by a high count rate, producing buffer overflows. During these periods, photons cannot be collected, generating gaps in the data. For this reason, the resulting good time intervals (GTI), generated using the `SAS` task `tabgtigen`, are relatively short, with an average duration of 10 s.

We checked for the presence of pile-up running the `SAS` task `epatplot`. We extracted the source counts in the range RAWX = [30 : 46] and we found that some fraction of pile-up affects the data. To mitigate it, we excluded the central pixels, i.e. RAWX = [36 : 39].

Being the observation in timing mode, it is not possible to extract background events by selecting a source free region. On the other hand, it is not recommended to extract background counts from the outer columns (i.e. by selecting pixels which intercept the point spread function tails) because this would modify the source spectrum (Ng et al. 2010). However, the source is very bright, with an average count rate of $\sim$ 220 counts $s^{-1}$ in the 0.5–10 keV energy band. Therefore, any background contribution is expected to be negligible (e.g. Ng et al. 2010). In any case, the most absorbed periods (potentially more affected by the background) are excluded when performing the spectral analysis presented in this work. On the other hand, the background is not expected to contribute to the fast X-ray variability (e.g. Uttley et al. 2011; De Marco et al. 2017). Therefore, in this work we decided not to subtract the background.

We used the `SAS` tools `arfgen` and `rmfgen` to extract the ancillary response files (ARF) and the redistribution matrix files (RMF), respectively. We first generated an ARF for the full region (RAWX = [30 : 46]). We then subtracted out a second ARF generated for the excluded region (RAWX = [36 : 39]) using the `SAS` task `addarf` (Wilkinson and Uttley 2009). The spectra were rebinned to ensure a minimum of 20 counts in each energy bin in order to apply chi-squared statistics.

For bright sources such as Cyg X-1, the EPIC-pn charge transfer efficiency (CTE) can cause an offset of the energy scale of the data. To our knowledge, this effect is only partly accounted for by the CTE modelling implemented in `SAS`. However, this effect has been mitigated in our spectral analysis by excluding the 1.5–2.5 keV energy band (e.g. Sala et al. 2007). This effect does not affect the X-ray timing analysis, as we used broad energy bands. We performed spectral analysis using `Xspec` v12.10.1 (Arnaud, 1996), while for the spectral-timing analysis we implemented codes using Python v3.6.

### 4.2.1 Selection of the events less affected by wind absorption

The presence of a stellar wind produces variable absorption of the X-ray source emission (see Sect. 2.5) which depends on the relative position of the compact object and the companion star in the orbit. This manifests as dips in the X-ray light curve, with variable intensity and recurrence time, depending on the amount and distribution of the intervening absorbing gas.

We extracted *XMM-Newton* EPIC-pn light curves in a soft and a hard energy band (i.e. 0.5–1.5 keV and 3–10 keV respectively), with a time bin of 10 s (Fig. 4.1). The two passages at superior conjunction occur during observations 201 and 701 (marked by red vertical lines in Fig. 4.1). The soft band light curve (upper panel in Fig. 4.1) presents several dips, in particular close to superior conjunction. Their intensity appears reduced in the hard band light curve (middle panel in Fig. 4.1), as the wind is more transparent at these energies. This results in a net increase

of the spectral hardness, defined as the ratio between count rates in the hard and soft bands (bottom panel in Fig. 4.1). It is worth noting that, despite their strong presence close to superior conjunction, dips are anyway present throughout the entire monitoring.

Following the approach proposed by Nowak et al. (2011) and Hirsch et al. (2019), we selected events less affected by wind absorption. The method is based on tracking the time-resolved spectral behaviour of the source by building colour-colour diagrams (Sect. 3.3). Depending on the amount of the absorbing gas along the LOS, the source occupies a different position in the diagram (Grinberg et al., 2020). Since the absorbing column changes over time, the source moves through different regions of the diagram over relatively short timescales. Since our aim is to filter out even the shortest absorption events, we considered light curves in the soft (0.5–1.5 keV), intermediate (1.5–3 keV) and hard (3–10 keV) energy bands (defined in Sect. 3.3) with a time resolution of 10 s. The resulting colour-colour diagrams are displayed in Fig. 4.2.

The least absorbed intervals show up as data points characterised by high hard and soft colours in the diagrams (i.e. they populate the upper right-hand corner of the diagram, marked in green in Fig. 4.2). In order to select the least absorbed intervals, we set a hard colour threshold of $\geqslant 0.95$ and a soft colour threshold of $\geqslant 0.7$, and considered all the events falling into the region of the diagram defined by these thresholds. In order to justify the choice of these particular thresholds, we built the simple model considered in Hirsch et al. (2019), consisting of a power law with spectral index $\Gamma = 1.7$ modified by a partial covering neutral absorber (i.e. representing the stellar wind) and by Galactic absorption. The corresponding `Xspec` model is `tbnew` $\times$ `tbpcf` $\times$ `powerlaw`, with Galactic $N_H = 0.7 \times 10^{22}\,\mathrm{cm}^{-2}$ (HI4PI Collaboration et al., 2016; Basak et al., 2017) and `wilm` abundances (Wilms et al., 2000). By comparing this model to the observed colour-colour tracks, we found that the theoretical track that best covers the range of the hard and soft colours spanned by the data corresponds to a covering factor of $\sim$ 0.9. For this value of covering factor, the chosen hard and soft colour thresholds correspond to a wind column density of $\mathrm{N}_{H,w} \leq 1.08 \times 10^{22}\,\mathrm{cm}^{-2}$. It is important to notice that the theoretical tracks obtained from this simple model do not accurately describe the exact shape of the observed colour-colour curves (see Appendix A). This indicates the need for a more complex model for the absorbing wind component. This is not relevant for the analysis described in this chapter, however such an issue will be addressed in detail in Ch. 5.

The data set resulting from this filtering process will be hereafter referred to as "NWA" (standing for "no wind absorption"), in order to distinguish it from the "Total", i.e. the data set unfiltered from the absorption of the wind. It is worth noting that the chosen time resolution of the light curves used to calculate

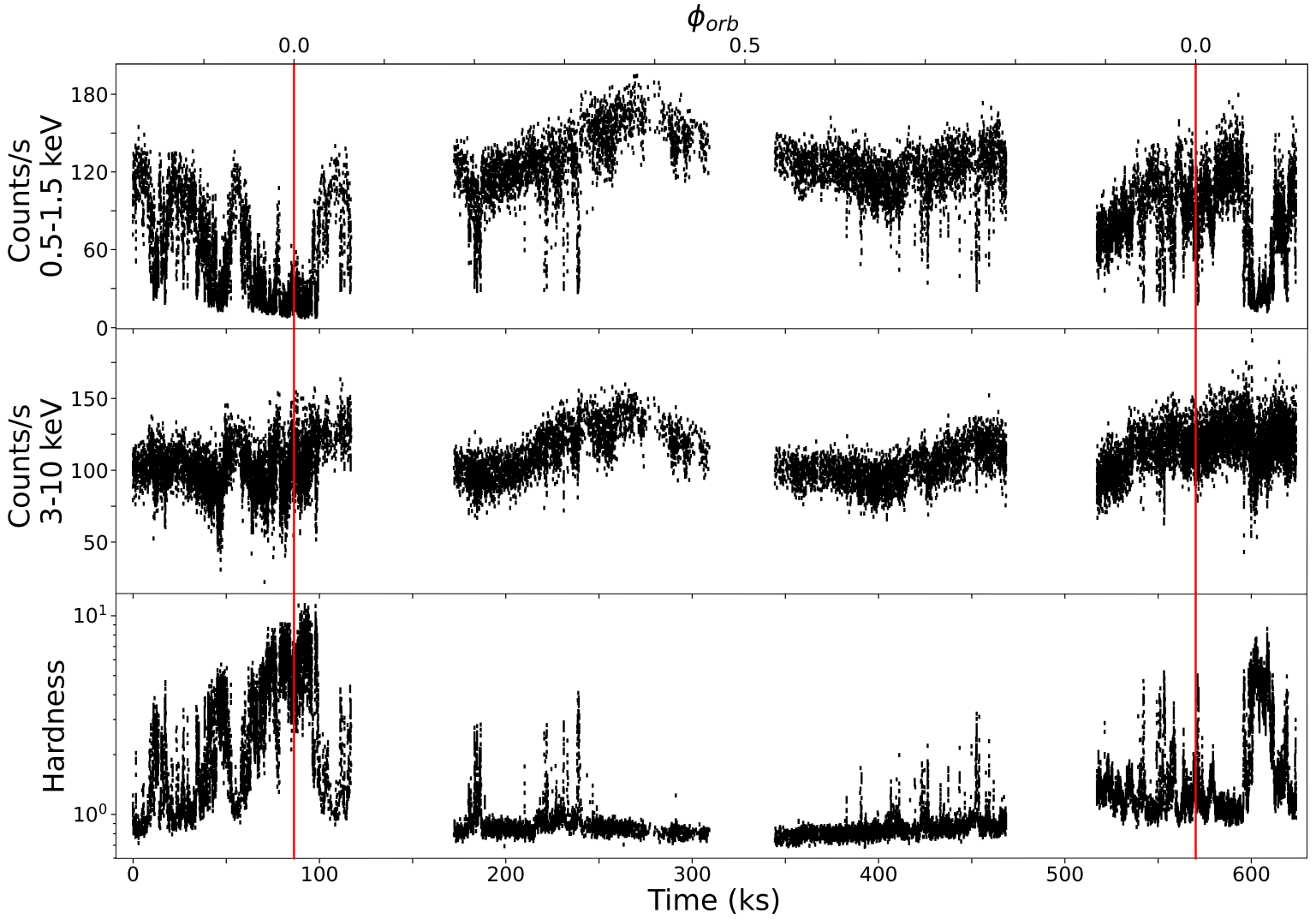


Figure 4.1: *XMM-Newton* EPIC-pn light curves of the CHOCBOX monitoring, comprising observations 201, 501, 601, and 701 (separated by gaps). The reference starting time of the campaign is 57535.9 MJD. The two red vertical lines at orbital phase $\phi = 0$ mark the two consecutive passages at superior conjunction. The soft band (0.5–1.5 keV) and hard band (3–10 keV) light curves are reported in the upper and middle panels, respectively. The bottom panel shows the 3–10 keV/0.5–1.5 keV hardness ratio.

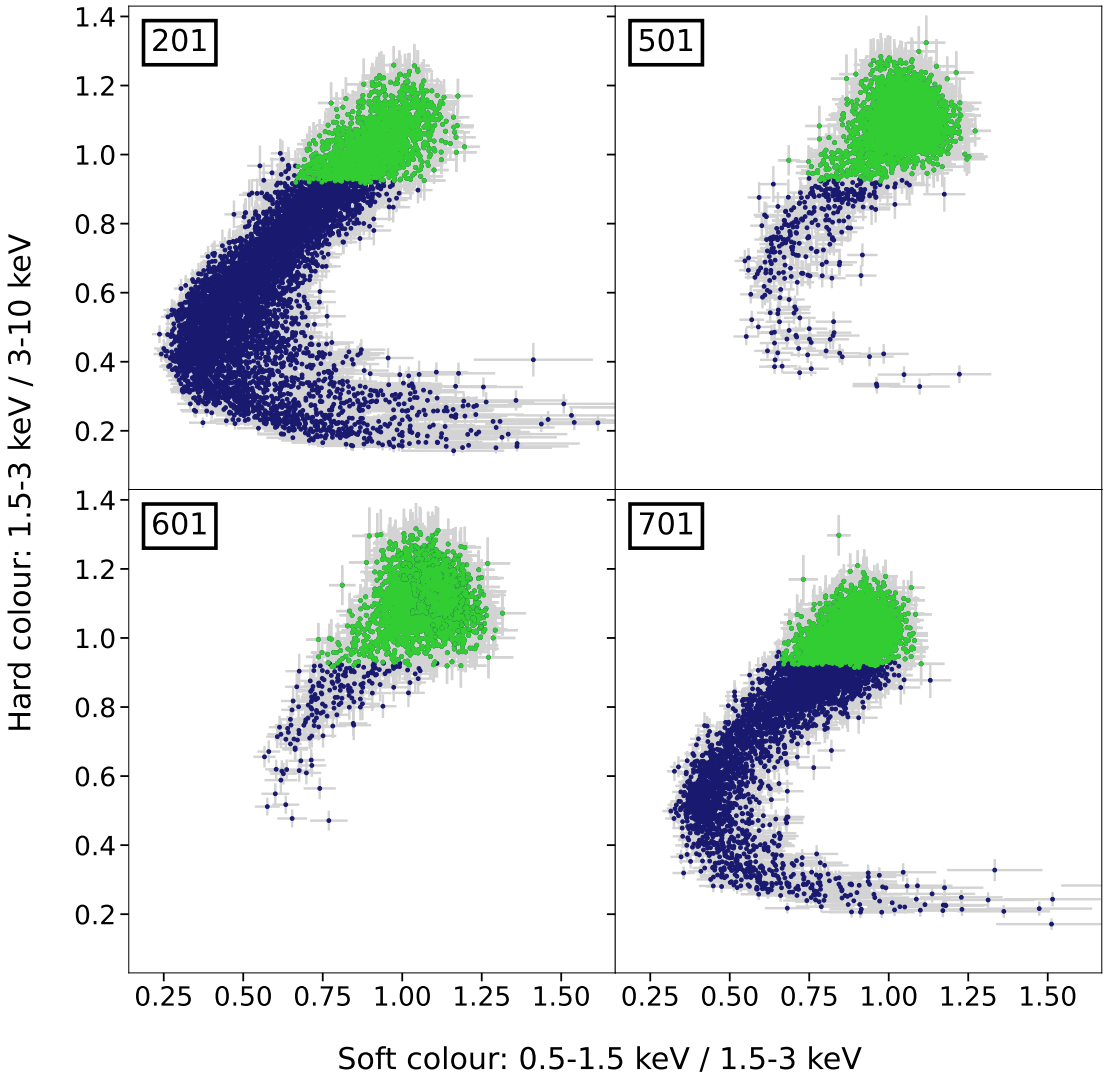


Figure 4.2: Colour-colour diagrams of each *XMM-Newton* observation of the CHOCBOX campaign. Hard and soft colours are calculated as the ratios of soft (0.5–1.5 keV) to intermediate (1.5–3 keV) and intermediate to hard (3–10 keV) energy bands, respectively. Each data point corresponds to a 10 s-long data segment. The green region selects data points less affected by wind absorption (i.e. with soft colours $\geqslant 0.7$ and hard colours $\geqslant 0.95$).

the colour-colour diagrams and the filtering procedure, guarantee a good filtering of strong wind absorption events lasting $\geqslant$ 10 s. However, this is insensitive to residual absorption due, for example, to wind clumps with a lower $N_{\rm H,w}$ and/or a lower covering factor moving faster across the LOS.

## 4.3 Power spectral analysis

We started by extracting the power spectrum of the NWA and the Total data sets of each observation to study the effects of the presence of the stellar wind on the X-ray variability of the source. We constructed power spectra in the three considered soft, intermediate, and hard energy bands (as defined in Sect. 3.3), using light curves with a time bin of 6 ms. We chunked each light curve into segments, each containing 1666 data points, with a length of 9.996 s. This allowed us to sample temporal frequencies in the range $\nu \sim 0.1$–83 Hz, thus corresponding to variability timescales of 0.1–10 s. Power spectra were calculated for each segment, and a mean power spectrum computed by averaging over all the power spectra of the single observations. We adopted the fractional rms normalisation (Sect. 3.2.1), in order to analyse the changes in the wind-modulated variability along the orbit. The Poisson noise contribution was estimated by fitting the power spectrum with a constant at $\nu > 25$ Hz, and subtracted out. The power spectrum was geometrically rebinned such that $\nu_{i+1} = 1.2\nu_i$.

Fig. 4.3 shows a comparison between the power spectra of the NWA and the Total data sets for the different *XMM-Newton* observations. For each observation, the power spectra are displayed for the soft, intermediate, and hard energy bands from left to right. It is evident that the presence of the stellar wind significantly contributes to changes in the X-ray variability properties of the source. The dominant effect is the smoothing out of the typical double-hump shape of the power spectrum of Cyg X-1 (see Sect. 2.4, Pottschmidt et al. 2003; Axelsson and Done 2018; Mahmoud and Done 2018a,b). This typically peaked shape is, however, recovered when considering the NWA power spectra, as well as for orbital phases of the source away from superior conjunction (i.e. during observations 501 and 601). Indeed, in both cases the X-ray emission of Cyg X-1 is less affected by wind absorption. Another effect of the wind is to reduce (by a factor of $\sim$ 2) the fractional variability at high frequencies ($\gtrsim 1$ Hz), and to increase it at low frequencies ($\lesssim 1$ Hz). This is most clearly seen in observation 201. However, the effects of the wind at $\lesssim 1$ Hz are more difficult to constrain given the limited bandpass.

A clear exception is observation 701: the power spectra of the NWA data set remain quite smooth as for the Total data set. We verified that this is caused by residual wind absorption not properly filtered out when considering the colour thresholds defined in Sect. 4.2.1. Indeed, when choosing a tighter threshold for

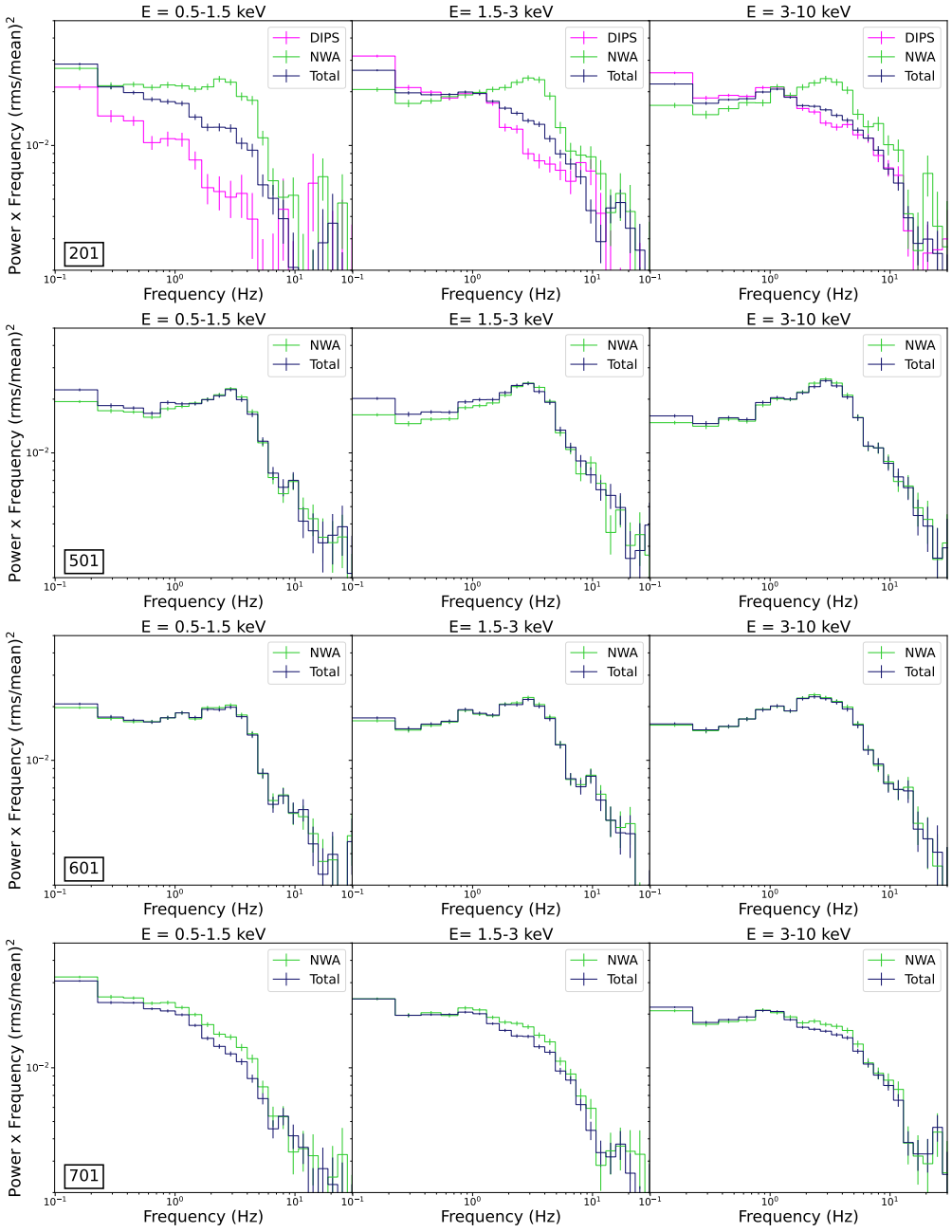


Figure 4.3: Power spectra of the Total (in blue) and the NWA (in green) data sets of each observation of the CHOCBOX monitoring. The power spectra were calculated in the soft (left panel), intermediate (middle panel) and hard (right panel) energy bands. For observation 201 (first row) we also show (in magenta) the power spectra obtained from the wind-dominated data set ("DIPS") defined in Sect. 4.5.

the hard and soft colours the double hump is resumed in the NWA data set (see Appendix B). The need for a different choice of colour threshold may indicate that the average properties of the stellar wind have changed between the two passages at superior conjunction. This is also suggested by the slightly different shapes of the colour-colour diagram during observations 201 and 701[2]. In order to better investigate changes in the properties of the stellar wind, a proper procedure for the modelling of the colour-colour diagrams should be defined. This issue will be addressed in Ch. 5.

The data set selection described in Appendix B for observation 701 significantly reduces the net exposure, thus reducing the S/N ratio for the spectral-timing analysis. Therefore, we decided to consistently use the same selection for the NWA time intervals for all observations (Sect. 4.2.1).

Finally, we note that the stellar wind affects the power spectrum not only in the soft and most absorbed energy band, but also at harder energies (at least up to 10 keV). This suggests rather high column densities in the deepest phases of the dips.

## 4.4 Cross-spectral analysis

Cross-spectral analysis gives us information on the causal relationship and the amount of correlated variability between two different energy bands (e.g. Nowak et al. 1999; Uttley et al. 2014), and consequently, between the spectral components that dominate those bands (Sect. 3.2.2). It is widely known that the hard state of BHXRBs is characterised by high levels of coherence between the primary Comptonisation component and the accretion disc over a broad range of timescales (e.g. Wilkinson and Uttley 2009). Additionally, on long timescales (i.e. $> 1$ s) the accretion disc is observed to lead the variations of the Comptonisation component. This has been interpreted in terms of mass accretion rate fluctuations propagating inwards from the disc through a spectrally inhomogeneous Comptonising region (Lyubarskii, 1997; Kotov et al., 2001; Arévalo and Uttley, 2006; Ingram and van der Klis, 2013; Mushtukov et al., 2018; Bollimpalli et al., 2020). On short timescales (i.e. $< 1$ s), for some sources, the disc is observed to respond to rapid hard X-ray variability (Uttley et al., 2011; De Marco et al., 2015a, 2021; Kara et al., 2019). This behaviour is ascribed to the thermal response of the disc to variable hard X-ray irradiation, i.e. thermal reverberation (e.g. Uttley et al. 2011; De Marco et al. 2017; Kara et al. 2019; Wang et al. 2020; De Marco et al. 2021).

[2]It is worth noting that such changes in the colour-colour diagram tracks may also be produced by intrinsic spectral changes of the X-ray source (see figure 2 of Grinberg et al. 2020). However, the mean spectral slope from our best-fit models appear consistent between these two observations (see Appendix C, Tab. C.1).

In this section, we examine the X-ray cross-spectral timing properties of Cyg X-1 to study the causal relationship between the primary Comptonisation component and the accretion disc, and constrain the effects of the wind on such properties. We first identified the energy bands dominated by the accretion disc and the Comptonisation component. To do so, we fitted the time-averaged spectra of the source. To minimise the stellar wind effects on the primary X-ray continuum, we extracted spectra considering only the NWA data sets. The spectra of each observation were fitted jointly. To avoid distortions due to electronic noise in timing mode (calibration file: XMM-CCF-REL-265; Guainazzi, Haberl & Saxton 2010[3]), we discarded data below 0.7 keV.

To fit the spectra, we used the model: `TBnew` × [`diskbb` + `nthComp` + `relxillCp`] in `Xspec`. The `diskbb` component describes the thermal emission from the accretion disc. The `nthcomp` component is used to model the soft excess in Cyg X-1, which has been ascribed to soft Comptonisation (Zdziarski et al. 1996; Życki et al. 1999). Although difficult to physically interpret (see Sect. 2.3), this component is necessary to model the spectra and obtain a reasonable fit (e.g. Zdziarski and Gierliński 2004; Basak et al. 2017). Finally, the `relxillCp` is used to model the hard Comptonisation component and its associated reflection spectrum (e.g. Dauser et al. 2014; García et al. 2015).

We forced the column density of the interstellar medium (ISM) and the inclination to be the same for all the spectra. For each single spectrum, we tied the seed photon temperature to the inner disc temperature. The high-energy cut-off of the hard Comptonisation component was fixed at 100 keV (Basak et al., 2017). To account for possible wind absorption residuals, we let the column density of the ISM free to vary. We found $N_H \sim 0.9 \times 10^{22}\,\mathrm{cm}^{-2}$, a value slightly higher than reported in Galactic neutral atomic hydrogen column density surveys (i.e. $N_H \sim 0.7 \times 10^{22}\,\mathrm{cm}^{-2}$, HI4PI Collaboration et al. 2016). Moreover, significant residuals are present in the range of energies $E = 1.5$–$2.5$ keV. Being close to the detector's absorption edges, these residuals are likely due to calibration issues. The fit significantly improves after ignoring this energy range, with a $\chi^2/dof = 11582/8268$. We found a spectral index of $\Gamma_H \sim 1.3$–$1.4$ for the hard Comptonisation component and an inner disc temperature of $kT_{in} \sim 0.17-0.2$ keV (see Tab. C.1)

In Fig. 4.4 we show the spectrum of each observation, the associated best-fitting model and its ratio to the data. We notice that the accretion disc dominates at energies $< 1$ keV, while the hard X-ray primary emission dominates the 2–10 keV energy range. Therefore, we selected the 0.3–1 keV and 2–10 keV energy bands for the computation of cross-spectra. We extracted light curves in the chosen energy bands with the same sampling parameters (i.e. time bin and segment length) used

[3] `https://www.cosmos.esa.int/web/xmm-newton/ccf-release-notes`

for the computation of the power spectra (Sect. 4.3). We extracted the cross-spectrum for each light curve segment, and averaged the cross-spectra within each single observation. We rebinned the cross-spectra to have a minimum number of 500 data points per frequency bin (see Sect. 3.2.2 and Ingram 2019). We repeated the procedure for the NWA and Total data sets of the four observations. We then computed the coherence (Sect. 4.4.1) and the time lags (Sect. 4.4.2) between the chosen energy bands.

### 4.4.1 Intrinsic coherence

The intrinsic coherence as a function of Fourier frequency (Sect. 3.2.2) computed between the 0.3–1 keV and 2–10 keV light curves is shown in Fig. 4.5 for the Total (blue points) and the NWA (green points) data sets.

Above $\sim$ 10 keV, a significant contribution from uncorrelated Poisson noise produces large uncertainties. For this reason, we limited our analysis to the frequencies less affected by Poisson noise (i.e. 1–10 Hz). We find that the intrinsic coherence of the Total data set significantly changes (between $\sim$ 0.6 and $\sim$ 0.9) among the different observations. We attribute this behaviour to the presence of the stellar wind. Indeed, observation 201 and 701, characterised by the strongest level of absorption, are those showing the lowest values of intrinsic coherence in the Total data set. On the other hand, the intrinsic coherence of the NWA data set is constant amongst all the observations reaching values as high as $\sim$ 0.95. This suggests that there are no significant changes of intrinsic coherence between variability in the two considered energy bands when considering the "bare" emission from the X-ray source, as commonly observed in Cyg X-1 in the hard state (Nowak et al., 1999; Pottschmidt et al., 2003; Grinberg et al., 2014).

### 4.4.2 Time lags

The time lags (Sect. 3.2.2) were computed using the same energy bands used to compute the intrinsic coherence in Sect. 4.4.1. The resulting time lags are shown in Fig. 4.6 for each observation, for the Total (blue points) and the NWA (green points) data sets.

We find that, at all frequencies, the lags amplitude is positive. This indicates that rapid variability in the 2–10 keV band is delayed with respect to the 0.3–1 keV energy band. Interestingly, there is no presence of a thermal reverberation lag at high frequencies (typically above 1 Hz) seen in other BHXRBs. Such lag would manifest as a negative delay, indicating that the disc dominated energy band (0.3–1 keV) responds to variability in the Comptonisation dominated energy band (2–10 keV).

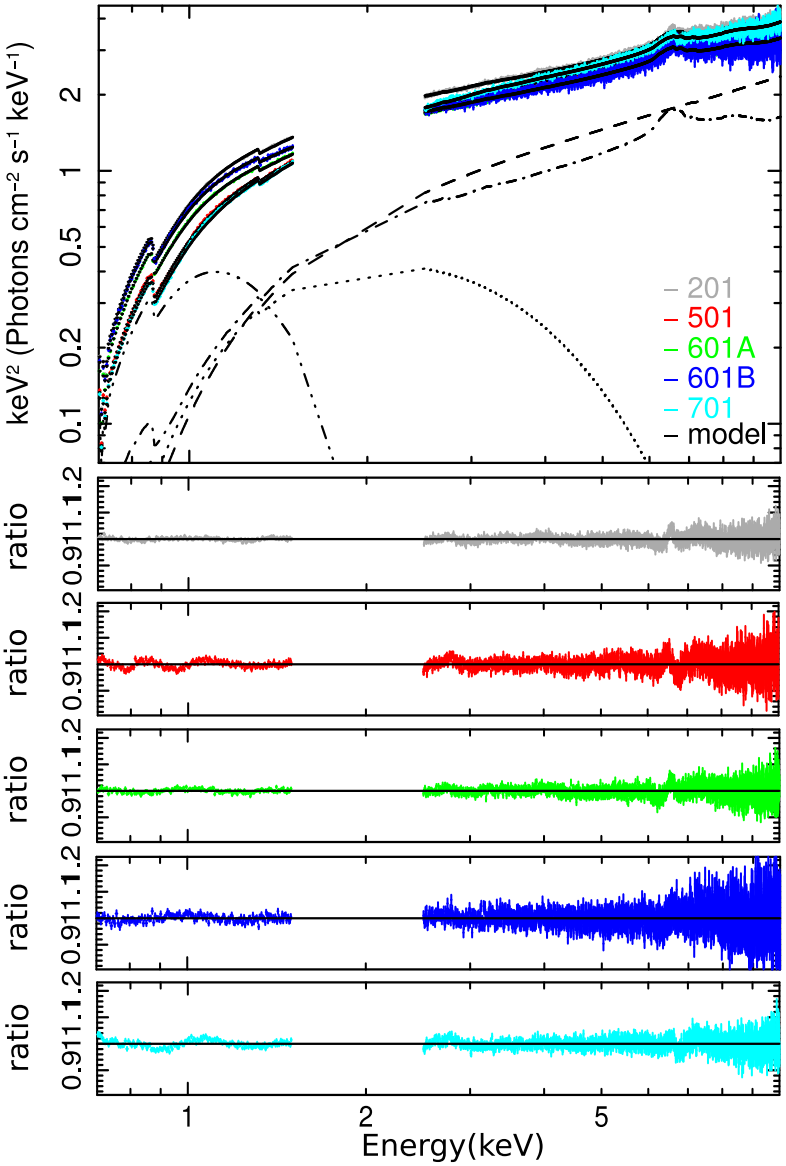


Figure 4.4: Best-fit models of the NWA time-averaged spectra jointly fitted for all observations. Observation 601 is split in two due to an observational gap in the data. The black, solid curve shows the best-fit model (`TBnew` × [`diskbb` + `nthComp` + `relxillCp`]). For clarity, in the upper panel we report the single best-fit components only for observation 201. The triple-dot-dashed curve shows the disc blackbody (`diskbb`), the dotted curve shows the soft excess (`nthComp`), the dashed curve shows the hard Comptonisation component (`relxillCp`, Comptonised part only), and the dot-dashed curve shows its reflection component (`relxillCp`, reflection part only). Large instrumental residuals are present in the range 1.5–2.5 keV, thus this range is excluded from the fit. The ratios of the data to the best-fit model are shown in the bottom panels for each spectrum separately.

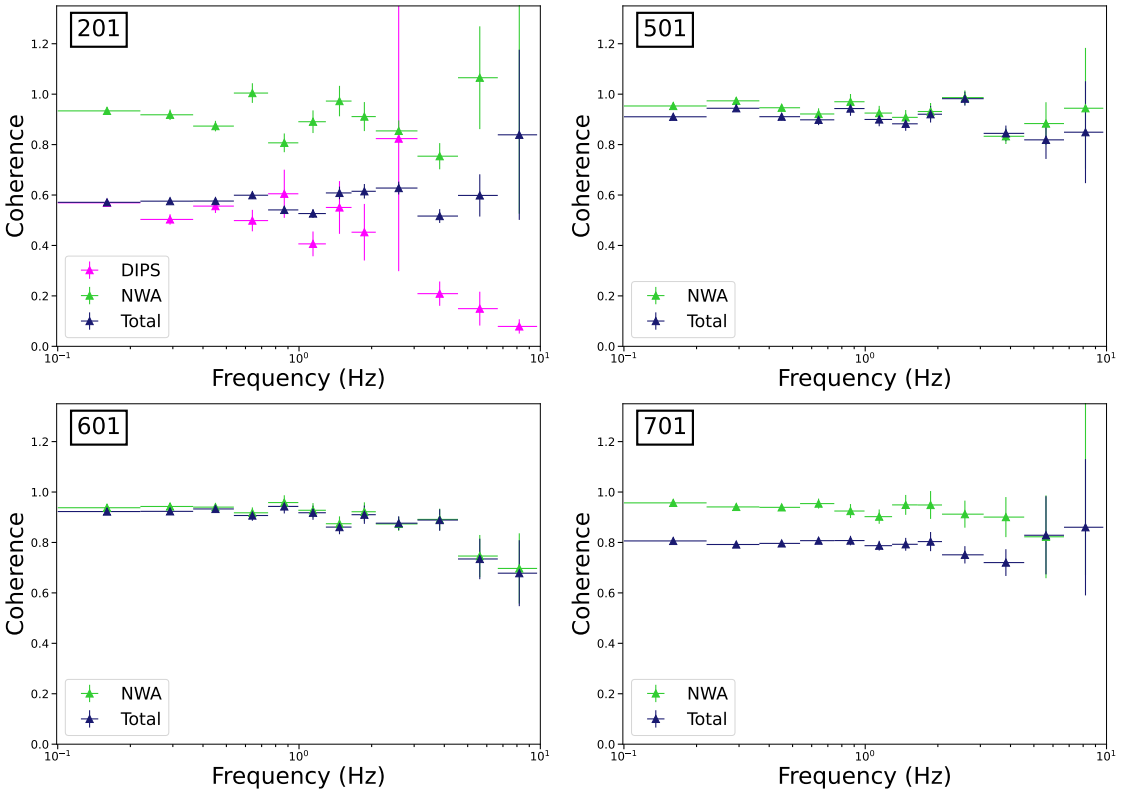


Figure 4.5: Intrinsic coherence as a function of Fourier frequency computed between the 2–10 keV and 0.3–1 keV energy bands, for the Total (in blue) and NWA (in green) data sets. The magenta data points shown for observation 201 correspond to the DIPS data set (as defined in Sect. 4.5).

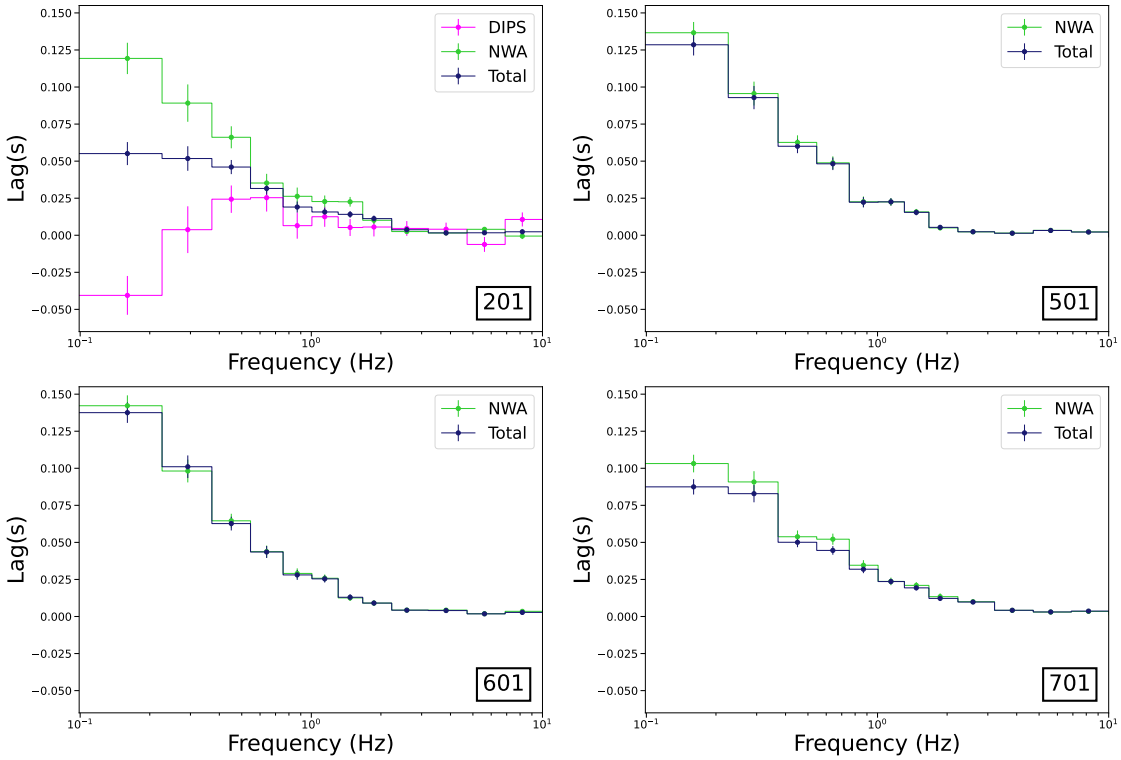


Figure 4.6: Time lags as a function of Fourier frequency computed between the 2–10 keV and 0.3–1 keV energy bands, for the Total (in blue) and NWA (in green) data sets. The magenta data points shown for observation 201 correspond to the DIPS data set (as defined in Sect. 4.5).

The detected low frequency hard lags are affected by the presence of the stellar wind. Indeed, the lag amplitude in the Total data set is slightly lower at low frequencies than in the NWA data set, during both observation 201 and (to a lesser degree) 701. After correcting for wind absorption effects (i.e. NWA data set in Fig. 4.6), the amplitude of the low-frequency hard lags increases, and appears to not show significant changes among the different observations[4].

[4]The slightly shorter amplitude of the hard lag in the NWA data set of observation 701 is likely related to the residual wind absorption also affecting the power spectrum, and discussed in Sect. 4.3 and Appendix B.

## 4.5 The X-ray spectral-timing properties of the stellar wind

The observed differences between the Total data sets and the NWA data sets invite to a deeper study of the spectral-timing signatures produced by the X-ray variability of the stellar wind. Therefore, we analysed time intervals strongly affected by wind absorption, i.e. the deeper phases of each dipping event (Fig. 4.1). In particular, we focused on observation 201, covering the first passage at superior conjunction. This choice is dictated by the fact that this observation displays the largest number of absorption dips in its light curve. As a matter of fact, the most absorbed regions of its colour-colour diagram are the most densely populated (Fig. 4.2).

We first analysed the dependence of the measured fractional rms on the amount of absorbing gas along the LOS. To this aim, we divided the colour-colour diagram into eight different regions. For a fixed value of the covering factor (Appendix A) these regions correspond to increasing values of the column density $N_{\rm H,w}$ (from A to H in Fig. 4.7). Following the same procedure as in Sect. 4.3, we calculated the power spectrum of the data for each selected region. Fig. 4.8 shows the power spectra (in squared fractional rms units) in the soft, intermediate, and hard energy bands. Significant differences can be observed at high and low frequencies as a function of the amount of intervening gas. In general, we observe a decrease of high frequency variability and an increase of low frequency variability power. For high values of $N_{\rm H,w}$ (i.e. regions D to H), we observe a suppression of the variability power at lower frequencies in the soft and intermediate energy bands (Fig. 4.8, upper and middle panel respectively). This indicates that, in the deepest region of the absorption dips, the low energy variability tends to be suppressed on all sampled time-scales.

We integrated the power spectra over two frequency intervals, i.e. 0.16–0.6 Hz and 2–5 Hz, to better visualise these trends. Fig. 4.9 shows the resulting fractional rms for the two frequency intervals and for each analysed energy band as a function of the selected region in the colour–colour diagram. The fractional rms in the 0.16–0.6 Hz frequency interval first increases up to $\sim$ 23–25%, and then decreases to $\sim$ 10–17% as the absorbing column increases. This change in the observed trend happens at high absorbing columns, but earlier in the colour-colour track (i.e. higher values of hard colour) for soft energy bands than for harder energy bands. In the soft energy band, the most affected by wind absorption, the highest/lowest values of maximum/minimum fractional rms are registered. On the other hand, in the hardest energy band, the decreasing fractional rms trend is not observed, but the fractional rms steadily increases, again suggesting that stellar wind absorption also affects this part of the spectrum. In the 2–5 Hz fre-

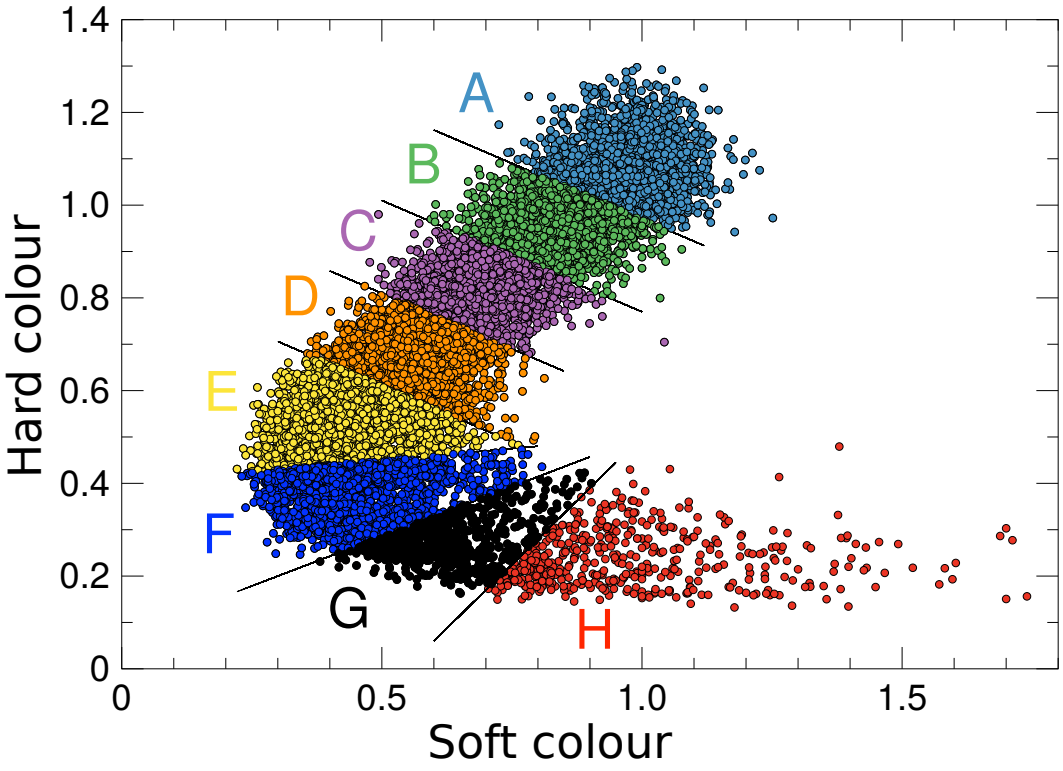


Figure 4.7: Colour-colour diagram of observation 201 showing the regions selected for the study of the power spectrum as a function of the amount of stellar wind absorption. The different regions (from A to H) correspond, for a constant value of the covering factor, to an increasing value of $N_{\mathrm{H,w}}$.

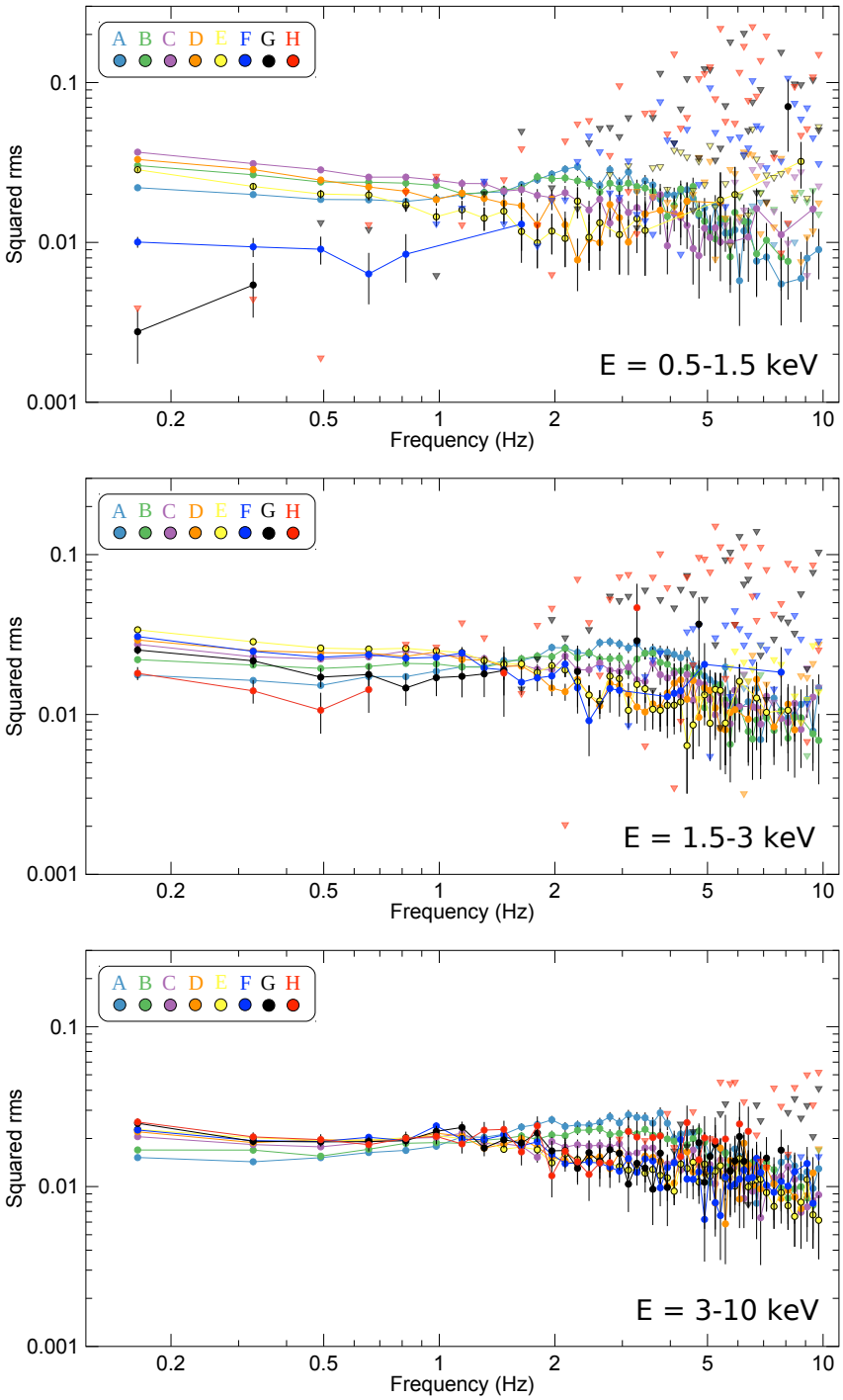


Figure 4.8: Power spectra for increasing values of wind column density. The data used are selected from the regions defined in Fig. 4.7 in the soft (upper panel), intermediate (middle panel) and hard (lower panel) energy bands. The triangles represent upper limits at $3\sigma$ confidence level.

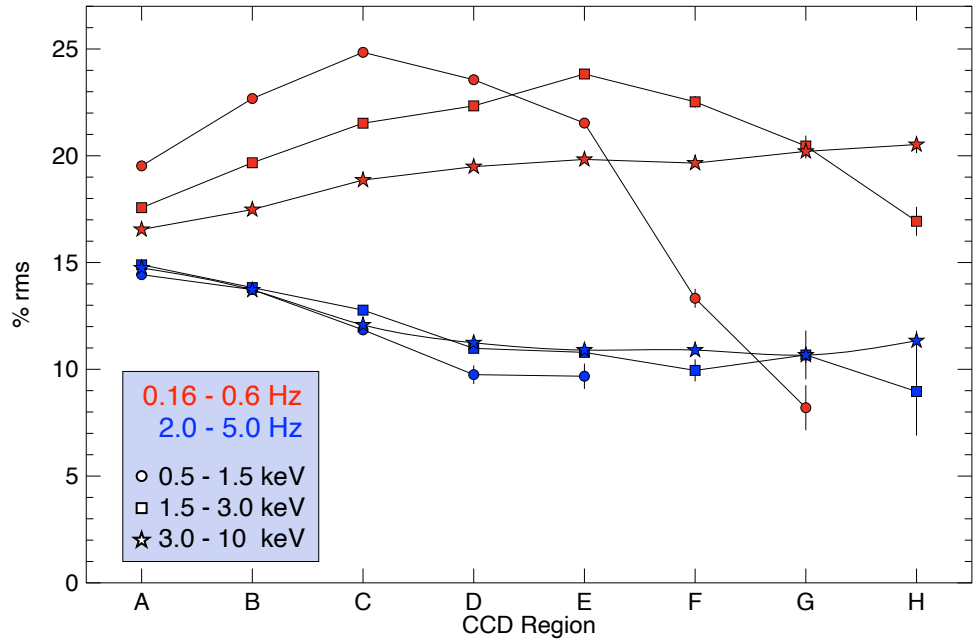


Figure 4.9: Fractional rms (in different energy and frequency bands) as a function of increasing absorption column (from A to H), as defined by the regions of the colour-colour diagram selected in Fig. 4.7.

quency interval the fractional rms shows a steadily decreasing trend (from $\sim 15\%$ to $\sim 12\%$) in every energy band, apparently reaching a plateau between region D to H. The increase of low frequency fractional rms can be ascribed to variability of the column density of the absorbing wind gas crossing the LOS to the X-ray source. On the other hand, the suppression of X-ray variability at high frequencies likely indicates the presence of additional scattering components. These aspects will be discussed in Sect. 4.6.

Finally, we focused on regions D trough H of Fig. 4.7, which select time intervals most affected by wind absorption (with hard colours $\leq 0.8$). We will refer to this data set as "DIPS". From these regions we extracted the intrinsic coherence and the time lags between the soft and the hard energy bands (as in Sects. 4.4.1 and 4.4.2). The resulting lags and coherence are overplotted in Figs. 4.5 and 4.6. A comparison with the results obtained from the Total and NWA data sets clearly demonstrates that the main cause of the low level of coherence and the decrease of hard lag amplitude during observation 201 is the presence of the stellar wind. Indeed, the DIPS data set is characterised by an overall low level of intrinsic coherence ($\lesssim 0.5$ and decreasing to 0 above 2 Hz), while a negative (soft) lag of a few tens of milliseconds dominates the lowest frequencies.

## 4.6 Discussion

Most of the studies on the stellar wind in Cyg X-1 are focused on how this component can modify the spectral properties of the X-ray source (e.g. Grinberg et al. 2015; Hirsch et al. 2019). Conversely, X-ray timing studies of Cyg X-1 focus on the X-ray source, while discarding the influence of the stellar wind on the observed X-ray variability properties of the source (e.g. Pottschmidt et al. 2003; Axelsson and Done 2018; Mahmoud and Done 2018a,b). Moreover, most of these studies are limited to $E \gtrsim 1$ keV. In this work, we demonstrated that the stellar wind strongly affects the observed X-ray variability of Cyg X-1, by modifying the observed levels of variability power, the amount of intrinsic coherence between softer and harder bands, and the amplitude of their relative lags. Moreover, the influence of the stellar wind on the observed X-ray variability strongly changes as a function of the orbital phase, due to the orbital modulation of the absorption.

### 4.6.1 Effects of the stellar wind on the X-ray variability power

We found that the observed X-ray variability power of the source is strongly influenced by the stellar wind in a complex way. We found a dependence on both

energy and timescales (see Sects. 4.3 and 4.5). We discuss the results separately, considering the low frequency and high frequency behaviour.

### X-ray variability power at low frequencies ($\lesssim 1$ Hz)

The effect of the variable X-ray absorption associated with the stellar wind is to increase the long-timescale (low-frequency) fractional rms of the source (see Figs. 4.3, 4.8 and 4.9). The excess of X-ray variability induced by the wind is observed at all considered energies, up to the highest (i.e. 3–10 keV). This result is in line with spectral studies which showed that the wind can modify the broad-band continuum up to $\sim 10$ keV (Grinberg et al., 2015).

Grinberg et al. (2015), considering a clumpy wind model, investigated the variability caused by the passage of clumps, of variable porosity (a measure of the mean free path among clumps) and size, as they cross our LOS. The main effect caused by these transits is an increase of the observed variability power due to variations of column density of the structured wind. An excess of X-ray variability could be seen only averaging over timescales as short as the duration of the passage of a single/small number of clumps. On longer timescales (lower frequencies), the wind-induced variability would be washed out as the result of averaging over many transits. Though the model assumes simplified conditions for the wind, it clearly shows how variations of the $N_{\rm H,w}$ can result in an increase of variability power as observed in the data we analysed (Figs. 4.3, 4.8 and 4.9). This implies that the timescales sampled in this work (i.e. 1–10 s) are sufficiently short to catch the transits of single clumps. Additionally, Grinberg et al. (2015) noted that in the model below (above) a certain timescale (temporal frequency) the stellar wind stops causing a further increase of the X-ray variability power. This timescale roughly corresponds to the time needed for a typical clump to transit the LOS and therefore can be used to infer a characteristic size of the clumps. Using our results, an estimate of this characteristic size can be obtained by considering the maximum frequency, $\nu_{max}$, at which excess variability power in the power spectrum of the Total data set is observed with respect to the NWA power spectrum. Assuming a terminal velocity $v_\infty = 2400\,{\rm km\,s^{-1}}$ (Grinberg et al., 2015), we find that the characteristic radial size of a clump is $l \sim 0.5$–$1.5\ \times 10^{-4} R_*$. The inferred range accounts for the different values of $\nu_{max}$ observed in the different observations. However, we note that this only represents an order of magnitude estimate because the clumps likely have a broad distribution of sizes (smaller clumps contributing more to the high frequency X-ray variability power). The larger values of $\sim 0.02$–$0.2\ R_*$, previously found by Hirsch et al. 2019, are probably due to the minimum sampled timescale of 25.5 s, which is longer than the range of timescales covered by the power spectra measured in our study.

In the most absorbed stages, corresponding to lower values of hard colour

(Fig. 4.7) and (for a given covering factor) to higher $N_{\rm H,w}$ (Fig. A.1), we found that the low-frequency X-ray variability power in softer bands starts to be significantly suppressed above a certain level of absorption (Fig. 4.9). To explain this decrease of low-frequency variability power during the dips, a possible and plausible mechanism is large-scale reprocessing/fluorescent scattering of soft band photons in the stellar wind. The differences in light travel time across the extended medium would strongly wash out the intrinsic flux variability of the X-ray source. In energy bands where the direct continuum is highly absorbed, this slowly variable or constant extended emission component from the wind would dominate. This would result in a net decrease of fractional rms at those energies. The higher the $N_{\rm H,w}$, the higher the energies at which this component dominates.

Additionally, we note that a similar effect could be produced in the ISM by scattering off dust layers. This would produce a soft spectrum due to the dependence of the dust scattering cross-section on energy (Predehl and Schmitt, 1995; Ling et al., 2009; Xiang et al., 2011). Nevertheless, this interpretation seems less plausible, given that the observed decrease of the fractional rms by a factor of $\sim 2$ observed in the dips in the softest energy band (Fig. 4.9) would imply quite a large scattering fraction.

### X-ray variability power at high frequencies ($\gtrsim 1\,$Hz)

Observations 201 and 701, covering the two consecutive passages at superior conjunction, are characterised by a strong suppression of high frequency variability, smoothing out the characteristic high frequency hump, a peaked feature in the power spectrum of the Cyg X-1 in the hard state (Sect. 2.4). This is clear when comparing the Total and the NWA data sets (Figs. 4.3 and B.1) as well as the DIPS data set from observation 201. Such a suppression is present at all energies, and it begins to occur at relatively low levels of wind absorption (Fig. 4.9). However, this behaviour cannot be ascribed to the stellar wind absorption. Indeed, as discussed in the previous section, variable absorption would result in an increase of fractional rms. On the other hand, a constant contribution from an absorption component would equally affect the flux from variable and constant components, thus, not causing changes in the fractional rms (which is the ratio between the variable and the total flux).

We therefore ascribe the suppression of high frequency variability power to some sort of scattering, and infer the optical depth of the putative scattering medium. Indeed, under this hypothesis, variability on timescales shorter (corresponding to high temporal frequencies in the power spectrum) than the light crossing time of the scattering medium will be significantly suppressed. The timescale/temporal frequency at which this happens is expected to increase/decrease as the optical depth $\tau_s$ increases (e.g. Zdziarski et al. 2010).

This behaviour has been previously seen in a number of sources (e.g. Belloni et al., 1991; Berger and van der Klis, 1994). In the case of the BHXRB Cyg X–3, the modelling of the power spectrum required the presence of a scattering medium optically thicker than the wind (Zdziarski et al., 2010). In our data the suppression of high frequency variability power in Cyg X-1 is roughly observed at $\nu \sim$ 5–10 Hz. Using equation 5 of Zdziarski et al. (2010), these frequencies correspond to $\tau_s \sim$ 0.5–1 for a scattering region with a radial size of $R \sim 3 \times 10^9$ cm, as inferred for Cyg X–3. We verified that the suppression of high frequency variability in the power spectrum of observation 201 is still seen at very high energies (see Fig. 4.10 which reports the power spectrum for the Total and the NWA data sets of observation 201 in the $E = 6$–10 keV energy band). This confirms the need for such a large value of $\tau$ as inferred from our calculations. These results reinforce the hypothesis of the presence of an optically thick medium intercepting the LOS to the X-ray source at superior conjunction. Nonetheless, previous analyses suggest $\tau_w \ll 1$ for Cyg X-1 stellar wind (Zdziarski, 2012), way lower than the value obtained from our estimates. A gas optically thicker than the wind is thus needed to explain the decrease of high frequency variability observed in Cyg X-1 (as also observed in Cyg X–3). This optically thicker medium may be linked to an accretion bulge, possibly formed by collision of the stellar wind with the edge of the accretion disc (e.g. Poutanen et al., 2008; Zdziarski et al., 2010). To further test this hypothesis, we extracted power spectra of observation 201 from two adjacent time intervals. Close to superior conjunction, we selected one time interval characterised by a low level of absorption and the other one dominated by strong dips (see the inset of Fig. 4.11). The high frequency variability hump is suppressed in both power spectra (Fig. 4.11, see the comparison with the NWA data set of observation 501, which shows the shape of the power spectra far from superior conjunction), meaning that the component causing such suppression does not depend on the intensity of the wind absorption dips. Therefore, this supports the hypothesis of the presence of a scattering bulge.

To conclude, we note that, at the highest sampled frequencies, the variability power is not completely suppressed. Indeed, when studying observation 201 in more detail, it is clear that the decrease of fractional rms at high frequency is followed by a plateau during the most absorbed stages (Fig. 4.9). This can be due to intrinsic source variability, either from photons reaching the observer without being scattered, or to residual contribution from variable absorption. For example, considering the above-mentioned clumpy wind scenario, the fact that the clumps producing excess variability at low frequencies likely have a distribution of sizes implies the existence of smaller clumps, which would contribute to the X-ray variability of the source at high frequencies.

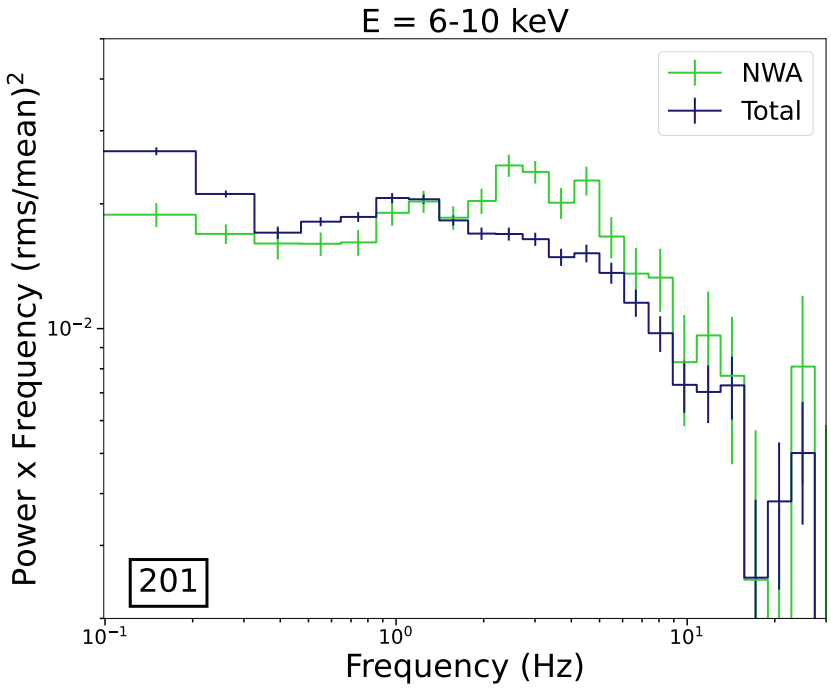


Figure 4.10: Power spectrum of observation 201 for the Total (in blue) and NWA (in green) data sets in the 6–10 keV energy band.

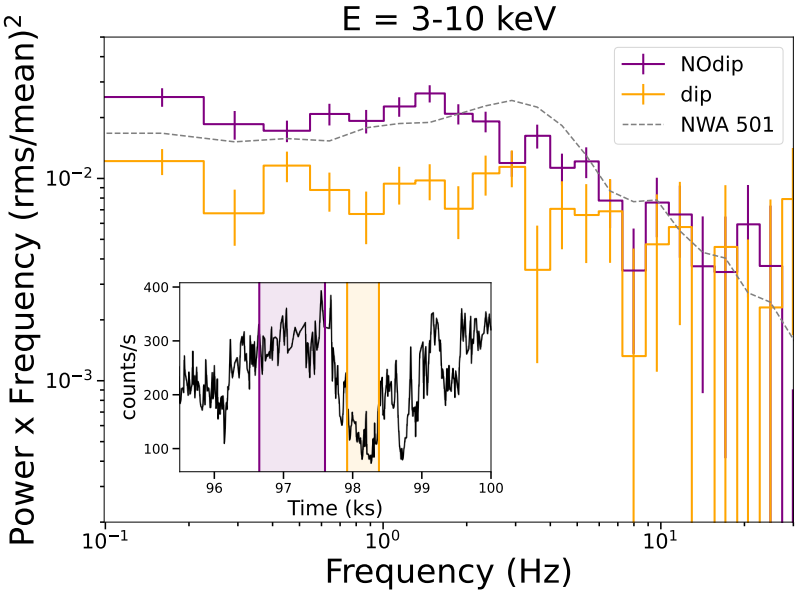


Figure 4.11: Power spectra extracted from two adjacent time intervals near superior conjunction during observation 201. The inset shows the selected intervals respectively characterised by low ("NOdip", in purple) and strong ("dip", in orange) absorption. The power spectra were extracted in the 0.3–10 keV energy band. For a comparison, the NWA power spectra of observation 501, near inferior conjunction, is also reported (dashed line), showing the intrinsic shape of the power spectrum of Cyg X-1.

**Effects of the stellar wind on the intrinsic coherence and time lags**

Another important effect that we found on all timescales is the decrease of intrinsic coherence between the soft (0.3–1 keV) and the hard (2–10 keV) energy bands due to the presence of the stellar wind (Fig. 4.5). On the contrary, accordingly to previous studies, the intrinsic coherence is close to unit when considering time intervals free from wind absorption (i.e. NWA in Fig. 4.5). Additionally, we found that the amplitude of the hard X-ray lags decreases at superior conjunction. This effect is strongest during observation 201 (Fig. 4.6), possibly caused by denser clustering of absorption events (Fig. 4.1).

The coherence loss we observe in the most absorbed phases of the orbit requires the emergence of one (or multiple) non-linear variability components. This is clearly a direct or indirect consequence of the presence of the stellar wind. Indeed, selecting the most absorbed time intervals of observation 201 (DIPS data set in the upper left-hand panel of Fig. 4.6), a low level of coherence is observed in the whole frequency interval (the average coherence at low frequency is $\sim 0.5$, a factor of $\sim 2$ lower than in the NWA data set). The most plausible way to explain the observed decrease in coherence between the two energy bands is the non-linearity of absorption variability given the presence of the stellar wind. This can be caused either by the motion of clumps, optically thicker in the soft with respect to the hard energy band, or by the non-linear response of the absorbing medium to variations of the hard X-ray flux. We note that a similar loss of coherence ascribable to the intervening absorption gas was found in the Seyfert 1 galaxy NGC 3783 (De Marco et al., 2020). Simulations showed that variations in the photoionization state of the wind, produced by variability of the irradiating X-ray flux, can cause significant losses of coherence level during the most obscured states (see also Juráňová et al. 2022).

Interestingly, the DIPS data set selected for observation 201, shows the presence of an additional, soft (negative) lag component at frequencies $\lesssim 0.2$ Hz (upper left panel in Fig. 4.6). This has the net effect of diminishing the amplitude of the observed hard X-ray lags at low frequencies in the Total data set (upper left panel in Fig. 4.6), i.e. when both absorbed and not absorbed intervals are considered. The resulting lag is likely due to large scale scattering off the wind, becoming dominant when the direct continuum is blocked by the strong absorption along the LOS. Another possible explanation is that the lag is due to recombination delays (Silva et al., 2016), thus scaling inversely with the density of the absorbing medium (Nicastro et al., 1999; Behar et al., 2003; Krongold et al., 2007; Kaastra et al., 2012). Nonetheless, a more detailed modelling with appropriate spectral-timing models as well as a higher energy-resolution study of the soft lag at low frequencies associated with the DIPS data set would be necessary to confirm this hypothesis.

# Chapter 5

# Characterisation of the stellar wind via modelling of time-resolved colour-colour diagrams

This chapter describes the study reported in the paper: "Characterisation of the stellar wind in Cyg X-1 via modelling of colour-colour diagrams"[1] accepted for publication in Astronomy and Astrophysics.

## 5.1 Introduction

As discussed in Sect. 2.5, line-driven winds (Castor et al., 1975) in HMXBs can be characterised by extremely high terminal velocities (up to $v_\infty \sim 2500$ km s$^{-1}$ Martínez-Núñez et al. 2017). Internal shocks lead to the formation of highly structured and over dense clumps (e.g. Owocki et al. 1988; Feldmeier et al. 1997; Oskinova et al. 2012; Sundqvist and Owocki 2013). Although several stellar wind models have been developed (e.g. Oskinova et al., 2012; Sundqvist and Owocki, 2013; Sundqvist et al., 2018; El Mellah et al., 2018, 2020), the physical properties of wind clumps, such as their density, distribution, shape and ionisation structure, are yet to be accurately constrained.

Investigating the stellar wind structure is of crucial importance. Not only it is key to understand the accretion mechanism in wind-fed HMXBs, but it is also fundamental to constrain models of stellar and galactic evolution. Indeed, stellar winds from massive stars are the main channel of stellar mass loss (with mass-loss rates up to $10^{-5}$ M$_\odot$ yr$^{-1}$ Puls et al. 2008; Martínez-Núñez et al. 2017). This influences the properties of the donor star as well as its evolutionary timescales. Additionally, in wind-fed binary systems, only a small fraction of the expelled

[1] https://doi.org/10.48550/arXiv.2408.05852

material is accreted. The rest escapes the system, causing a decrease of angular momentum and a consequent change in the orbital parameters. This can lead either to a shrinking or a widening of the orbit (e.g. Hoyle and Lyttleton, 1939; Bondi and Hoyle, 1944; Paczynski, 1976; El Mellah et al., 2020), depending on key parameters such as the stellar wind terminal velocity, the orbital separation and the accretion efficiency (e.g. Saladino et al., 2018). All together this can have a high impact on the rate of merging events, and ultimately provide crucial information on merger progenitors (e.g. Bulik et al., 2011; Belczynski et al., 2011; Neijssel et al., 2021).

Cyg X-1 is a perfect laboratory to constrain the stellar wind structure and its physical properties (see Sect. 2.5). In Ch. 4 we showed how the stellar wind modifies the timing properties of the source. In particular, on timescales longer than 1 s, the wind contributes to an increase of the observed X-ray fractional variability. We ascribed this behaviour to the motion of clumps of the size of $\sim 10^{-4}\,R_*$. Radiative hydrodynamical simulations demonstrated how clumps should increase in size as they move away from the star (Sundqvist et al., 2018), thus producing absorption dips of different duration. Therefore, sensitivity to a broad range of timescales is necessary to fully investigate the clumps' properties. In particular, the shortest timescales ($\sim$ 1 min or shorter) allow us to characterise the smallest clumps, formed close to the base of the wind. However, the limitations of current instruments (particularly in terms of collective area), do not allow us to investigate spectral changes occurring on very short timescales via canonical spectral analysis. A possible solution to this problem is to use colour-colour diagrams (see Sect. 3.3, e.g. Nowak et al. 2011; Grinberg et al. 2020). Indeed, detailed modelling of the colour-colour diagram of wind-fed systems provides a way to constrain the stellar wind properties. Previous studies used empirical functions or simple (neutral) stellar wind models to explain the characteristic shape of colour-colour tracks (e.g. Hanke et al., 2008; Nowak et al., 2011; Hirsch et al., 2019). Recently, Grinberg et al. (2020) made use of more complex wind models. They concluded that different levels of ionisation in the wind structure should be accounted for in order to obtain a proper description of the observed colour-colour tracks. In this work, starting from the results obtained by Grinberg et al. (2020), we model the colour-colour diagrams of Cyg X-1 in order to constrain the stellar wind parameters as a function of the orbital phase. We used this approach to infer two of the main physical properties of the stellar wind: the stellar mass-loss rate and the mass of the clumps (e.g. El Mellah et al., 2020).

## 5.2 Observation and data reduction

For the analysis presented in this chapter we focused on the first *XMM-Newton* observation of Cyg X-1 of the CHOCBOX monitoring (see Sect 3.1), observation 201. The observation caught the source in the hard state, and during a passage at superior conjunction (orbital phases between 0.82 and 0.06). In Ch. 4 we studied how the stellar wind affects the X-ray spectral-timing properties of the X-ray source. In particular, we showed that observation 201 resulted to be the most affected by wind absorption among all observations composing the *XMM-Newton* CHOCBOX campaign. Moreover, the strongest effects on the fast (i.e. 0.1–10 s) X-ray variability were observed during this observation (as compared to the rest of the monitoring). Despite focusing on observation 201 for the characterisation of the stellar wind properties, we also made use of observation 501 in order to localize the area of the colour-colour diagram less affected by absorption. Observation 501 covers orbital phases between 0.17 and 0.46, the closest to inferior conjunction ($\phi_{orb} = 0.5$, see Fig. 3.1), thus it is ideal to characterise the source colours during the least absorbed stages (see also Fig. 4.1).

We used the EPIC-pn (Strüder et al., 2001) data in timing mode for both observations. We performed the data reduction using the *XMM-Newton* `SAS`, version 20.0.0, and CCF as of 2022 March. As discussed by Diez et al. (2023), the default Rate Dependent PHA (RDPHA) correction applied to EPIC-pn data in timing mode could result in spectral line energies higher than expected. In order to mitigate this problem, we followed the non-standard calibration procedure suggested by Diez et al. (2023). Specifically, we used `epproc` on the Observation Data Files (ODFs), turning off the RDPHA correction (imposing `withrdpha='N'`) and applying the Rate Dependent CTI (RDCTI) correction via `epfast` (imposing `runepfast='Y'`). For the rest of the data reduction we followed the same procedure described in Sect. 4.2. First of all we screened calibrated event files for strong background flaring events. We used light curves in the 10–15 keV energy band with a time bin of 1 s. Nonetheless, we did not observe significant flares. Then, we used the `SAS` task `epatplot` to investigate for the presence of pile-up. We found that a small fraction of pile-up is affecting the data. We therefore corrected for it. The resulting extracted region excludes the central pixels RAWX = [36 : 39], i.e. RAWX = [30 : 35; 40 : 46]. As discussed in Sect. 4.2, since the observation is in timing mode and Cyg X-1 is a very bright source (200 counts $s^{-}1$), we did not account for the background in this analysis. We followed the same procedure we described in Sect. 4.2 to extract the ARF and RMF and the spectrum of the observation 201 via the `SAS` tasks `arfgen`, `rmfgen` and `addarf`. We also rebinned the spectrum to ensure the minimum of 20 counts per bin. We used `Xspec` v12.10.1 (Arnaud, 1996) for the spectral fitting. The Interactive Spectral Interpretation System (`ISIS`) version 1.6.2 plus a Python (v3.10) proprietary code were used to

calculate and model the colour-colour diagrams. Time series were extracted using `stingray` v1.1.2 (Huppenkothen et al., 2019; Huppenkothen et al., 2019; Bachetti et al., 2023).

## 5.3 Colour-colour diagram models for Cyg X-1

As we already mentioned in Sect. 2.5, stellar wind clumps crossing our LOS induce dips in the X-ray light curve, with a duration comprised between several seconds to hours (Hirsch et al., 2019). To better explore the presence of such dips in observation 201 (see Fig. 4.1 for the entire monitoring), we extracted light curves in the soft (0.5–1.5 keV) and hard (3–10 keV) bands (Fig. 5.1). A net increase of the hardness ratios between the two light curves (bottom panel of Fig. 5.1) is observed in correspondence of the absorption dips, the latter being about three times more intense in the soft than in the hard band. The single dips are quite short, with a duration of $\lesssim 1$ ks. As a result, given the swiftness of such events, their energy spectrum is hard to study via time-resolved spectroscopy. This motivates the use of colour-colour diagrams (see Sect. 3.3, e.g. Nowak et al. 2011) for the study of the broad band spectral variability of the source. As mentioned in Sect. 3.3, the least absorbed phases are characterised by high values of both soft and hard colours, mapping the upper-right region of the diagram. For increasing absorption along the LOS, colour values change. In case of a partially covering absorber, the resulting colour-colour tracks show a "pointy" or "nose-like" shape as the source becomes more absorbed (i.e. in the colour-colour diagram lower region, see e.g. Hirsch et al., 2019).

Building on previous works (Hanke et al., 2008; Nowak et al., 2011; Hirsch et al., 2019; Grinberg et al., 2020), we extracted the colour-colour diagram of observation 201 using light curves with a time bin of 10 s. This time resolution allows us to sample spectral variability on a wide range of timescales, down to those probably produced by quite small clumps. The size of the clumps is directly connected to the fly-by time across the LOS. With such time resolution, the minimum size of the clumps that can be inferred is $\sim 2 \times 10^{-4} R_*$, when assuming a wind terminal velocity $v_\infty = 2400\,\mathrm{km\,s^{-1}}$ (Grinberg et al., 2015).

In order to find a suitable stellar wind model capable to describe the observed colour-colour diagram tracks in Cyg X-1, we then tested a number of physical scenarios. We chose a primary X-ray continuum modified by a partially covering absorber (Fürst et al., 2014; Fornasini et al., 2017; Grinberg et al., 2020) as our baseline model. The adopted model is of the form:

$$\mathtt{abs}_{ism} \times \mathtt{continuum} \times (f_c \times \mathtt{abs}_{wind} + (1 - f_c)) \tag{5.1}$$

where $\mathtt{abs}_{ism}$ is the ISM absorption, `continuum` is the unabsorbed primary emis-

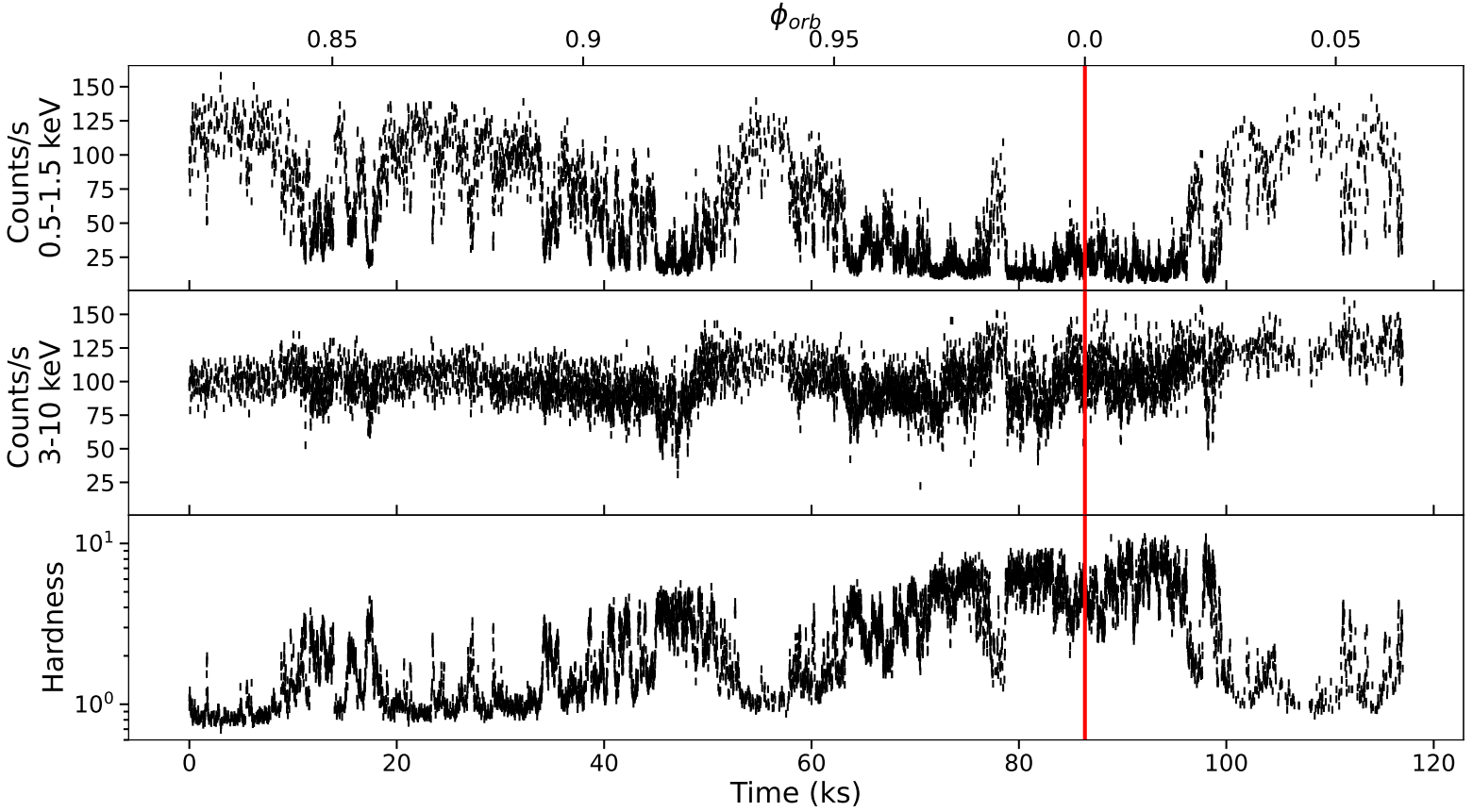


Figure 5.1: *XMM-Newton* light curves (with 10 s time bin) of observation 201 of Cyg X-1 in detail (see Fig. 4.1 for the light curve of the entire CHOCBOX monitoring). The upper and the middle panels show, respectively, the soft and the hard energy band light curves. Hardness ratios (hard-to-soft) are reported in the bottom panel. The passage at superior conjunction is highlighted with the red vertical line.

sion from the X-ray source and $\texttt{abs}_{wind}$ is the absorption component associated with the stellar wind. This component blocks a fraction ($f_c$, or covering factor) of the X-ray source photons, while only a percentage $1 - f_c$ reaches the observer, modified only by absorption in the ISM.

We used standard `Xspec` models (Arnaud, 1996) for both the continuum and the stellar wind component to simulate spectra within `ISIS` (Houck and Denicola, 2000; Houck, 2002; Noble and Nowak, 2008), using the response matrices from observation 201 (see Sect. 5.2). We let vary the model parameters of interest, and for each parameter combination, we calculated the corresponding soft and hard colours. For each set of simulations, in order to speed up the process, only one parameter is left free to vary, while the others are kept fixed. This procedure permits to build simulated colour-colour tracks, which are then compared to the data. In the following, we illustrate the different tested models. Throughout this work the ISM absorption was modelled with `TBabs`[2] using the `vern` cross-sections(Verner et al., 1996) and the `wilm` abundances (Wilms et al., 2000). The ISM column density was kept fixed at the tabulated value of $\sim 0.7 \times 10^{22}\mathrm{cm}^{-2}$ (HI4PI Collaboration et al. 2016). In this work, we are mainly interested in testing for variability of the stellar wind component, thus we did not investigate intrinsic spectral variations of the X-ray source.

### 5.3.1 Model 1: a neutral stellar wind and a single power law

We first simulated theoretical colour-colour tracks considering a power law for the continuum and a partially covering neutral absorber for the stellar wind. In this model the shape of the colour-colour tracks mainly depends on three parameters: the photon index $\Gamma$ of the power law describing the continuum, the stellar wind covering fraction $f_c$, and its column density $N_{\mathrm{H,w}}$.

The resulting simulated tracks are over plotted on the colour-colour diagram of observation 201 in Fig. 5.2. For fixed values of $N_{\mathrm{H,w}}$ and $\Gamma$, a variable $f_c$ describes the curvature of the blue-cyan tracks shown in Fig. 5.2. The parameter $f_c$ spans values between 0.1 and 1, at steps of 0.1. From deep blue to light cyan, tracks are obtained by increasing the value of $N_{\mathrm{H,w}}$ from a minimum value of $0.1 \times 10^{22}\,\mathrm{cm}^{-2}$ to a maximum value of $32 \times 10^{22}\,\mathrm{cm}^{-2}$ (for higher values of $N_{\mathrm{H,w}}$ hard colours start to increase again, however they produce an upward tail which is not observed in the data). On the other hand, for fixed values of $\Gamma$ and $f_c$, a variable $N_{\mathrm{H,w}}$ describes the curvature of the red-orange tracks shown in Fig. 5.2 (with $N_{\mathrm{H,w}}$ within the range 0.1–$32 \times 10^{22}\mathrm{cm}^{-2}$). The deep red to light orange tracks are obtained by increasing the value of $f_c$ from 0.1 to 1.

[2] `https://pulsar.sternwarte.uni-erlangen.de/wilms/research/tbabs/`

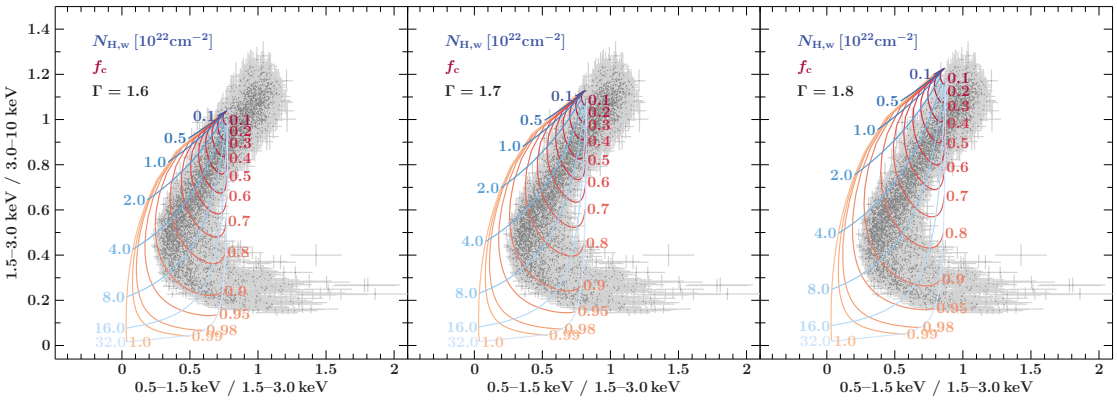


Figure 5.2: Comparison of the simulated tracks for a power law (for Γ values fixed at 1.6, 1.7, and 1.8, from the left to the right panel) plus a neutral absorber and the observed (gray points) colour-colour diagram tracks of observation 201 of Cyg X-1. The blue (red) tracks describe variations in the stellar wind $f_c$ ($N_{\rm H,w}$) for a fixed value of $N_{\rm H,w}$ ($f_c$).

The same simulations were repeated for Γ=1.6, 1.7, and 1.8 (panels from left to right in Fig. 5.2), matching typical values for the hard state (e.g. Joinet et al., 2008; Motta et al., 2009; Gilfanov, 2010; Basak et al., 2017; Zhou et al., 2022).

Our analysis confirms the results from previous studies (e.g. Hirsch et al., 2019; Grinberg et al., 2020) showing that this simple model fails to describe the observed colour-colour diagram. Indeed, while approximating the curvature of the observed track, a variable $N_{\rm H,w}$ does not properly reproduce the characteristic pointy shape at low hard colours (giving the track a nose-like shape). We observe that a varying Γ shifts the tracks only vertically. For this reason, in line with previous studies (e.g. Grinberg et al., 2020), we infer that a more complex modelling of the stellar wind and/or the intrinsic X-ray continuum is required by the data. Indeed, the need for a more complex primary continuum for Cyg X-1 as well as a structured stellar wind made of differently ionised material (Hirsch et al., 2019) has been also highlighted by spectroscopic studies (e.g. Basak et al., 2017; Tomsick et al., 2018) .

### 5.3.2 Model 2: an ionised stellar wind and a structured continuum

Changing our assumptions on the underlying primary continuum we then tested a more complex model. We assumed the model presented in Sect. 4.2.1 (`TBabs` × `[diskbb + nthComp + relxillCp]` in `Xspec`) used to fit the NWA data set (see Sect. 4.2.1 for the detailed description on how this data set has been obtained)

to properly assess the time-averaged parameters of the continuum. Additional details on the best-fit continuum model we used in these simulations are reported in Appendix D.

In Fig. 5.3 we show the colour-colour tracks calculated for a neutral medium, partially absorbing the adopted structured continuum. These tracks start right at the centre of the observed distribution of data points (upper part of the diagram), thus representing an improvement with respect to the simulations shown in Fig. 5.2 for Model 1. This indicates that the new continuum model describes the unabsorbed time-averaged spectrum much better than a simple power law. Therefore, we used this more complex model to describe the continuum in the following simulations.

In order to account for the effects of an ionised wind on the simulated colour-colour tracks, we substituted the $\texttt{abs}_{wind}$ component in Eq. 5.1 with the `warmabs` (v2.31) analytic photoionisation model (Kallman et al., 2009). As done in Grinberg et al. (2020), we made use of the standard population files delivered with `warmabs`, with densities of $10^{12}\,\mathrm{cm}^{-3}$ (typical of stellar wind densities close to the compact object, Lomaeva et al. 2020). We first verified how the simulated tracks are modified by different levels of ionisation. To this purpose, we considered different values of the ionisation parameter $\xi = L_X/nr^2$ (Tarter et al., 1969), where $L_X$ is the ionising luminosity above 13.6 eV, $n$ is the absorbing gas density and

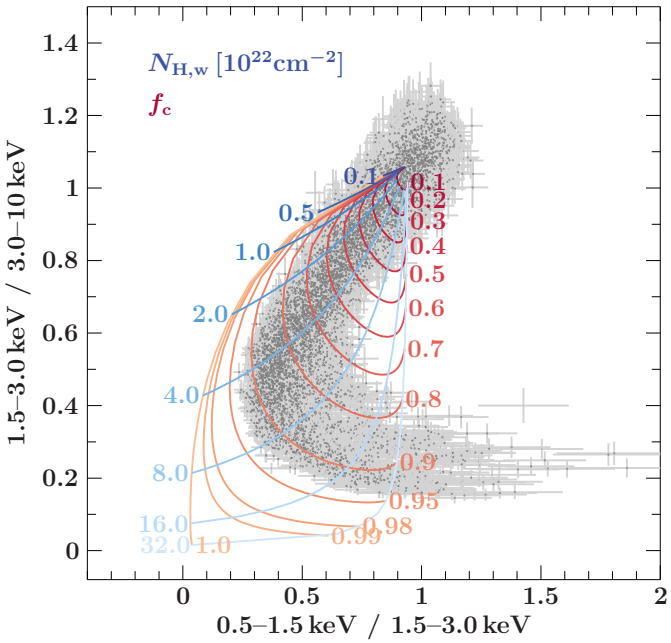


Figure 5.3: Simulated tracks for the complex continuum plus neutral wind model, compared to the colour-colour diagram of observation 201.

$r$ its distance from the ionising X-ray source. We considered $\log \xi$ values comprised between $-4$ and 2. We let the $N_{\rm H,w}$ vary in the range 0.1–32 $\times 10^{22}$ cm$^{-2}$ for each fixed value of $\log \xi$. The resulting tracks are shown in Fig. 5.4. The same simulations were repeated for three different values of the covering factor ($f_c = 0.8, 0.87, 0.95$, Fig. 5.4 from left to right).

Increasing the ionisation parameter makes the simulated tracks more pointy, thereby more closely matching the observed tracks. Increasing the covering factor primarily extends the range of the hard and soft colours. Specifically, with sufficiently high $N_{\rm H,w}$, a higher $f_c$ results in a higher absorption at low-to-intermediate energies, making absorption dips more spectrally hard (lower values of hard and soft colours during the most absorbed stages). We observe that, among all simulated curves, the one better resembling the observed tracks corresponds to $f_c = 0.87$, $\log \xi = 1.6$, and $N_{\rm H,w}$ varying in the range 0.1–32 $\times 10^{22}$ cm$^{-2}$, as highlighted in black in Fig. 5.4 (middle panel) thus suggesting mild ionisation for the partially covering wind.

### 5.3.3 Model 3: stellar wind with variable ionisation

In Sect. 5.3.2 we assumed a constant ionisation parameter for the stellar wind. However, Hirsch et al. (2019) showed that the most absorbed stages of the dips, populating the lower part of the colour-colour diagram, are characterised by the presence of less ionised species. This is consistent with the existence of structured clumps, made of differently ionised material. Therefore, changes in the ionisation parameter need to be considered in order to properly model the observed colour-

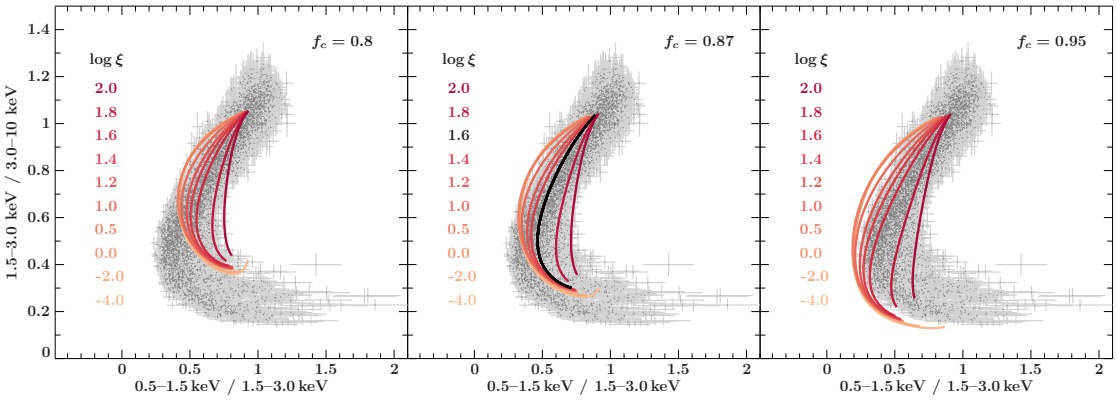


Figure 5.4: Comparison between the simulated tracks for a homogeneously ionised absorber (with $\log \xi = -4-2$) and the colour-colour diagram of observation 201. From the left to the right panel, the simulated tracks are computed for values of $f_c$ of 0.8, 0.87 and 0.95. The curve best describing the data is highlighted in black.

colour diagrams (Grinberg et al., 2020). For this reason, we then accounted for variations of the ionisation parameter of the stellar wind as a function of $N_{\rm H,w}$.

As done by Grinberg et al. (2020), we tested two empirical functions for the dependence of the ionisation parameter on the column density of the absorbing material. The first function is:

$$\log \xi = \log(A/[N_{\rm H,w}/10^{22}{\rm cm}^{-2}]), \tag{5.2}$$

with $A > 0$. This function assumes a linear decrease of $\xi$ as a function of $N_{\rm H,w}$, reflecting the definition of the ionisation parameter. The second function is:

$$\log \xi = \log \frac{B + [N_{\rm H,w}/10^{22}\,{\rm cm}^{-2}]}{[N_{\rm H,w}/10^{22}\,{\rm cm}^{-2}]} + C, \tag{5.3}$$

with $B, C > 0$. This function assumes that the ionisation parameter remains relatively high at high column densities, significantly deviating from a linearly decreasing trend. Such a behaviour is expected if an additional source of ionisation plays an important role in denser environments (e.g. Feldmeier et al., 1997). The values of the constant parameters were arbitrarily chosen to be $A = 100$, $B = 10$, and $C = 1$. This choice of parameters allows for the two functions to match at low column densities $N_{\rm H,w}/10^{22}\,{\rm cm}^{-2} << 10$, while diverging significantly at higher densities, $N_{\rm H,w}/10^{22}\,{\rm cm}^{-2} \gtrsim 1$. We let $N_{\rm H,w}$ vary in the range 0.01–$32 \times 10^{22}\,{\rm cm}^{-2}$. The lowest value in this range, $N_{\rm H,w} = 0.01 \times 10^{22}\,{\rm cm}^{-2}$, corresponds to the highest value of the ionisation parameter allowed by the `warmabs` model. The first function covers the range of $\log \xi \sim 0.5$–4, while the second function covers $\log \xi \sim 1.12$–4. Fig. 5.5 shows the two empirical functions.

We built models consisting of the complex continuum defined in Sect. 5.3.2 modified by the variable absorption produced by each of these two empirical functions. Due to the fact that the data in the colour-colour diagrams are not normally distributed, a simple $\chi^2$ minimisation method cannot be used to find the best-fit model. Therefore, we employed a non-parametric method, which does not require any prior assumption on the distribution of the data.

We inferred the probability density function (PDF) of the data using the kernel density estimation (KDE) method (e.g. Hill, 1985; Cavecchi and Patruno, 2022). The KDE is a non-parametric estimator whose functional form is determined by combining as many building blocks (kernels) as the number of data points. A single type of kernel $K$ is used, and its choice is arbitrary. This choice does not affect significantly the final output if the data set is large. For our analysis, we chose a Gaussian kernel. The kernel $K_i$ centred on the data point $\vec{x}_i$ is defined as:

$$K_i(\vec{x}) \propto \exp\left(-\frac{(\vec{x} - \vec{x}_i)^2}{2h^2}\right) \tag{5.4}$$

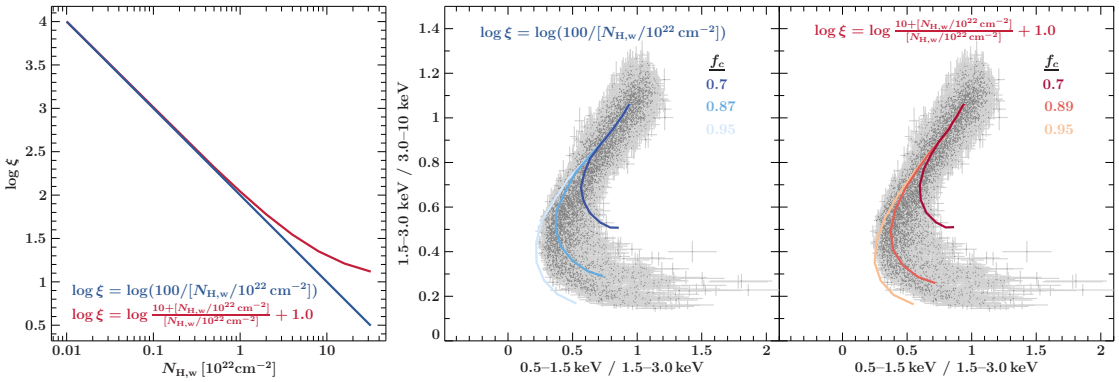


Figure 5.5: Assumed dependencies of the ionisation parameter $\log \xi$ on the column density $N_{\rm H,w}$ (left panel). Comparison of the simulated tracks for a warm absorbing gas, assuming $\log \xi = \log(100/[N_{\rm H,w}/10^{22}\,{\rm cm}^{-2}])$ (middle panel), and $\log \xi = \log \frac{10+[N_{\rm H,w}/10^{22}\,{\rm cm}^{-2}]}{[N_{\rm H,w}/10^{22}\,{\rm cm}^{-2}]} + 1$ (right panel). Different values of covering factor are presented with different shades as reported in the labels.

where $\vec{x}$ is the data point in the colour-colour diagram at which the kernel function is estimated. The level of smoothing is controlled by the width of the kernel $h$. The normalised PDF is computed as the sum of the contribution of the kernels centred on each data point:

$$\mathrm{PDF}(\vec{x}) = \frac{1}{n}\sum_{i}^{n} K_i(\vec{x}) \tag{5.5}$$

with $n$ being the total number of data points. We made use of the SciPy function `gaussian_kde` to implement the method. The optimal kernel width is automatically determined by the function (default parameter `bw_method='scott'`[3]). Given the estimated the PDF of the data, we computed the combined likelihood of each simulated model as the product of the values of the probability density at each point of the model. We chose as the best-fit model the one characterised by the highest combined likelihood.

Fig. 5.5 shows the best-fit track obtained using the functions $\log \xi = \log(100/[N_{\rm H,w}/10^{22}{\rm cm}^{-2}])$ (middle panel) and $\log \xi = \log \frac{10+[N_{\rm H,w}/10^{22}\,{\rm cm}^{-2}]}{[N_{\rm H,w}/10^{22}\,{\rm cm}^{-2}]} + 1$ (right panel) to model the ionised absorber. In both cases, the best-fit track is obtained by fitting for the covering factor $f_c$ parameter (between 0.7 and 0.95, at steps of 0.01) while $N_{\rm H,w}$ spans the entire range $0.01 - 32 \times 10^{22}\,{\rm cm}^{-2}$ for each fit value of the covering factor. The tracks corresponding to $f_c = 0.7$ and $f_c = 0.95$ are also shown

[3] `https://docs.scipy.org/doc/scipy/reference/generated/scipy.stats.gaussian_kde.html`

(Fig. 5.5). Outside these limiting values the simulated curves do not intersect the data in the lower part of the diagram.
For hard colours $\gtrsim 0.8$, i.e. when the source is less absorbed, the simulated tracks are not very sensitive to the covering factor. In this regime all the simulated curves resemble fairly well the observed shape of the track. Nonetheless, in the most absorbed stages (i.e. lower values of hard colours), the dependence on the covering factor becomes significant. The two variable ionisation models considered in this work describe the data well, with a mild 5% difference between their inferred likelihoods. Such a small difference does not allow either one of the two models to be preferred over the other. Interestingly, both functions can resemble the pointy shape of the data much better than the model we considered in Sect. 5.3.2, i.e. an homogeneously ionised absorber. This gives more support to the hypothesis of a structured absorber.

Finally, we note that the data all lay within the simulated tracks for $f_c = 0.7$ and $f_c = 0.95$. The data points scatter in this part of the diagram might be partially due to intrinsic variations of the covering factor between these two limit values. In the following section we further investigated this possibility.

## 5.4 Time-resolved colour-colour diagrams

We investigated the temporal evolution of the colour-colour diagram shape in order to study the phase-dependent variability of the absorbing column density and covering fraction of the stellar wind. To this aim, we divided observation 201 in 10 segments of the same duration of ∼11 ks each (corresponding to orbital phase segments of ∼0.024). We then calculated the colour-colour diagram for each of them. Fig. 5.6 shows all the corresponding tracks with a colour code based on the range of orbital phases. A strong temporal evolution of the tracks is evident. The same data are shown in Fig. E.1, Appendix E, divided in separate time-resolved colour-colour diagrams. We inferred the PDF of the data in each diagram via the KDE method (see Sect. 5.3.3). Fig. 5.7 shows the resulting probability distribution maps.

The source passage at superior conjunction occurs at $t \sim 86.36$ ks from the starting time of the observation (see Fig. 5.1), thus it is caught by panel "h", which corresponds to $\phi_{\rm orb} = 0.988$–$0.012$. The fact that the LOS crosses the densest stellar wind regions in this orbital phase is clearly evident from the shape of the corresponding colour-colour track, whereby *only* the lower region of the diagram is populated (i.e. at hard colours $\lesssim 0.75$). Both at earlier and later phases of the orbit (i.e. from panel "f" to "i") we observe a similar distribution due to strong dipping events happening several hours before and after superior conjunction (see Fig. 5.1). The observed changes in the colour-colour tracks can

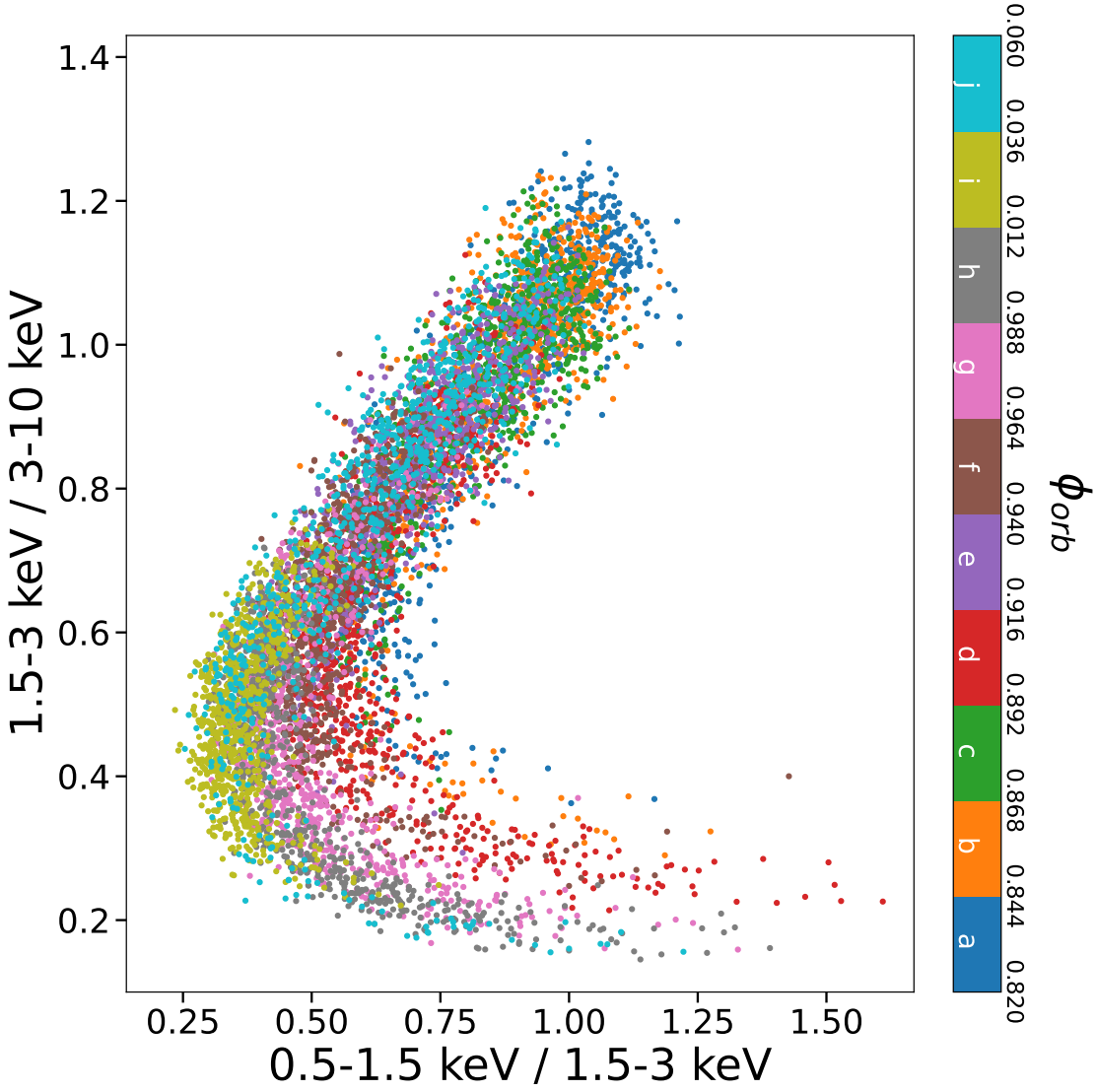


Figure 5.6: Time-resolved colour-colour diagrams of observation 201. Each diagram is calculated extracting segments with a duration of 11 ks (corresponding to $\sim$0.024 in orbital phase) and time resolution of 10 s. All the diagrams are over plotted with different colours to distinguish the covered orbital phases (see the colour map on the right).

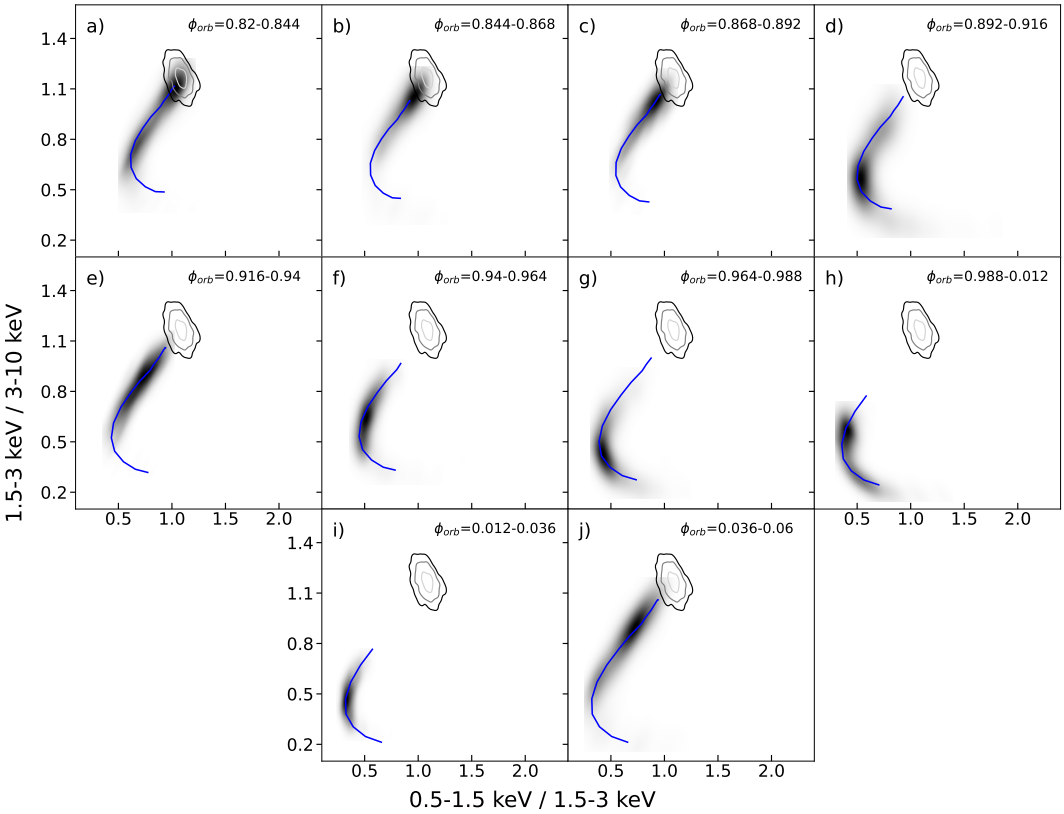


Figure 5.7: Probability distribution maps of the time-resolved colour-colour diagrams of each epoch obtained using the KDE method. The best-fit simulated tracks are shown in blue. The grey-shaded areas represent the probability distribution map close to inferior conjunction ($\phi_{\rm orb} = 0.43$–$0.46$) at the 99.7% (in black), 95% (in grey) and 68% (in light grey) confidence levels.

be caused by changes in the wind parameters. Therefore, we built simulated tracks for each time-resolved colour-colour diagram in order to constrain such parameters. To this purpose, we made use of the complex continuum model fitted to the spectrum of each time-resolved epoch (see Sect. 5.3.2 for its description) plus the variable ionisation absorption component described by the empirical function $\log \xi = \log \frac{10+[N_{\rm H,w}/10^{22}\,{\rm cm}^{-2}]}{[N_{\rm H,w}/10^{22}\,{\rm cm}^{-2}]} + 1$ (see Sect. 5.3.3 and Fig. 5.5, left panel in red). We chose to use this particular empirical function, although not statistically preferable to the other one we tested in Sect. 5.3.3 (in Fig. 5.5, left panel in blue), because we wish to include the effects of additional sources of ionisation becoming important in denser environments (e.g. Feldmeier et al., 1997; Sundqvist and Puls, 2018), such as the base of the wind, intercepted by the LOS at superior conjunction. As described in Sect. 5.3.3, the best-fit tracks are the ones giving the highest combined

likelihood. Fig. 5.7 (as well as Fig. E.1) shows the best-fit tracks, while Tab. 5.1 lists the best-fit covering factors for each time-resolved diagram.

It is worth noticing that the best-fit tracks do not always reach to high hard colours as much as the data do. This is particularly visible when the source is out of superior conjunction (i.e. panels "a", "b", "c", and "j"), during the less absorbed phases of the orbit. This is due to the fact that the model reaches the maximum allowed value for the ionisation parameter (the lowest values of $N_{\rm H,w}$ correspond to the highest values of $\xi$ in our model, left panel in Fig. 5.5). Nonetheless, the portion of the colour-colour diagram not covered by the wind model track comprises the least absorbed data bins. Therefore, in this region, the scattering in the measured hard and soft colours might be completely driven by the spectral variability intrinsic to the source. To test this, we calculated a colour-colour diagram from observation 501, carried out right before inferior conjunction, thus one of the observations of the CHOCBOX monitoring least affected by the wind (see Figs. 3.1 and 4.1). It is worth clarifying that CHOCBOX missed the passage at $\phi = 0.5$, thus we selected the closest orbital phases to it ($\phi_{\rm orb} = 0.43$–$0.46$). Moreover, observation 501 is consecutive to observation 201. This permits to rely on the implicit assumption that the X-ray source continuum spectrum has not significantly changed between the two observations, and that any scatter in the colour-colour diagram would only be associated with fluctuations in the parameters of the same continuum model. The KDE method (Sect. 5.3.3) was used to calculate the probability distribution of soft and hard colours in the colour-colour diagram of observation 501. The diagram and the corresponding contour plots are shown in Fig. F.1, Appendix F. The data are quite scattered, suggesting intrinsic variability of the continuum on short timescales. To highlight the region of the diagram in which the intrinsic emission from the X-ray source dominates, in Figs. 5.7 and E.1 we over plot the 99.7%, 95% and 68% confidence contours of observation 501. In this area, the probability for the source to be free from stellar wind absorption is the highest. As a result, the data points not reached by the simulated tracks are therefore fully consistent with being free from stellar wind absorption.

The fit of the time-resolved colour-colour diagrams reveal a steady and significant increase of the covering factor, by approximately a factor of 1.2 between $\phi_{\rm orb} = 0.820$–$0.844$ and $\phi_{\rm orb} = 0.036$–$0.06$ (see Tab. 5.1). In Fig. 5.8, upper panel, we plot the resulting trend. We register the maximum value of the covering factor at superior conjunction. However, the data suggest this parameter remains high up to at least $\phi_{\rm orb} = 0.06$. Using the PDFs of Fig. 5.7 and our best-fit tracks we calculated the average column density $\overline{N}_{\rm H,w}$ and its scatter $\delta N_{\rm H,w}$. The latter is an indicator of the amount of short-term variability of $N_{\rm H,w}$. For each epoch, we report these values in Tab. 5.1 and plot them in Fig. 5.8 (middle and lower panels). The procedure we used is the following: once a best-fit track is inferred,

we calculate the probability of each point using the KDE method, which is thus a function of $N_{\rm H,w}$. Next, we consider the range of $N_{\rm H,w}$ that encompasses 68% of the total (renormalised) probability for the corresponding track, serving as a proxy for the total number of data points. The parameter $\delta N_{\rm H,w}$ is given by the width of the range, while $\overline{N}_{\rm H,w}$ is given by the average value. This approach is more informative than, for example, considering the highest probability to extract $N_{\rm H,w}$. This is because, the latter method would result in a loss of information, especially for cases in which the distributions show more than one peak. As an example, fitting the colour-colour diagram shown in panel "a" in Fig. 5.7 would result in a low $N_{\rm H,w}$, therefore missing the information associated with the second peak of the PDF. The procedure also gives a straightforward way to infer the confidence intervals for each pair of $\overline{N}_{\rm H,w}$ and $\delta N_{\rm H,w}$ values. Considering the two tracks corresponding to the extrema of the $f_c$ 68% confidence level, we now repeat the procedure obtaining new confidence level of $N_{\rm H,w}$. In order to be conservative, we consider the overall maximal and minimal confidence level to obtain the intervals of $\overline{N}_{\rm H,w}$ and $\delta N_{\rm H,w}$. Significant variations are observed in both parameters: $\overline{N}_{\rm H,w}$ and $\delta N_{\rm H,w}$. The two show the same trend of variations (when the average column density increases, its scatter also increases), while the trend characterising $f_c$ differs. Specifically, both $\overline{N}_{\rm H,w}$ and $\delta N_{\rm H,w}$ show two peaks. The second peak occurs at superior conjunction, when also $f_c$ reaches its maximum value. Nevertheless, when $f_c$ is still at its maximum, the other two parameters drop by a factor $\sim$2.5 and $\sim$2, respectively. This is clearly visible in panel "j" of Fig. 5.7 and Fig. E.1. In this panel, the data populate again the region of high hard colours (as in panels "a–e"), also stretching down to the lowest registered hard colours. Finally, it is important to notice that the measured values of $\overline{N}_{\rm H,w}$ (ranging from $\sim 6 \times 10^{22}\,{\rm cm}^{-2}$ to $\sim 16 \times 10^{22}\,{\rm cm}^{-2}$) all fall in the regime where our model predicts significant additional ionisation in high density environments (see Fig. 5.5, left panel). In this regime, strong variations of $\overline{N}_{\rm H,w}$ along the dips are not accompanied by equally strong variations of the ionisation parameter, the latter remaining constrained within the range $\log \xi \sim$1.2–1.4.

### 5.4.1 On the soft tail of colour-colour tracks

Before going further with the discussion of our results, we note that among all the models used to fit the colour-colour diagrams (Sect. 5.3 and Sect. 5.4), none is able to produce tracks that can explain the tail extending down to high values of soft colours characterising the most absorbed stages of the dips (see e.g. Fig. 5.5 and Fig. E.1).

Such high values of soft colour indicate the presence of an additional soft component, whose contribution becomes significant in the deeper parts of the dips. Possible candidates are the emission lines produced by the wind itself, and/or

Table 5.1: Parameters inferred from the best-fits of the time-resolved colour-colour diagrams of observation 201. The table reports the orbital phases ranges covered by each time-resolved diagram and the stellar wind parameters: the covering factor $f_c$, the average column density $\overline{N}_{\rm H,w}$ and its scatter $\delta N_{\rm H,w}$. The column density parameters are in units of $10^{22}$ cm$^{-2}$.

| $\phi_{\rm orb}$ | $f_c$ | $\overline{N}_{\rm H,w}$ | $\delta N_{\rm H,w}$ |
|---|---|---|---|
| $0.820 - 0.844$ | $0.74 \pm 0.01$ | $6.88 \pm 0.02$ | $4.93 \pm 0.03$ |
| $0.844 - 0.868$ | $0.74 \pm 0.01$ | $6.22 \pm 0.27$ | $6.70 \pm 0.53$ |
| $0.868 - 0.892$ | $0.76 \pm 0.01$ | $6.00 \pm 0.15$ | $6.6 \pm 0.3$ |
| $0.892 - 0.916$ | $0.80 \pm 0.01$ | $11.78 \pm 0.48$ | $11.84 \pm 0.97$ |
| $0.916 - 0.940$ | $0.85 \pm 0.01$ | $5.48 \pm 0.23$ | $7.12 \pm 0.47$ |
| $0.940 - 0.964$ | $0.84 \pm 0.01$ | $9.76 \pm 0.46$ | $9.51 \pm 0.91$ |
| $0.964 - 0.988$ | $0.88 \pm 0.01$ | $13.55 \pm 0.56$ | $10.92 \pm 1.11$ |
| $0.988 - 0.012$ | $0.90 \pm 0.01$ | $16.09 \pm 1.31$ | $16.15 \pm 2.62$ |
| $0.012 - 0.036$ | $0.92 \pm 0.01$ | $10.80 \pm 0.28$ | $7.02 \pm 0.55$ |
| $0.036 - 0.060$ | $0.92 \pm 0.01$ | $6.52 \pm 0.06$ | $8.38 \pm 0.11$ |

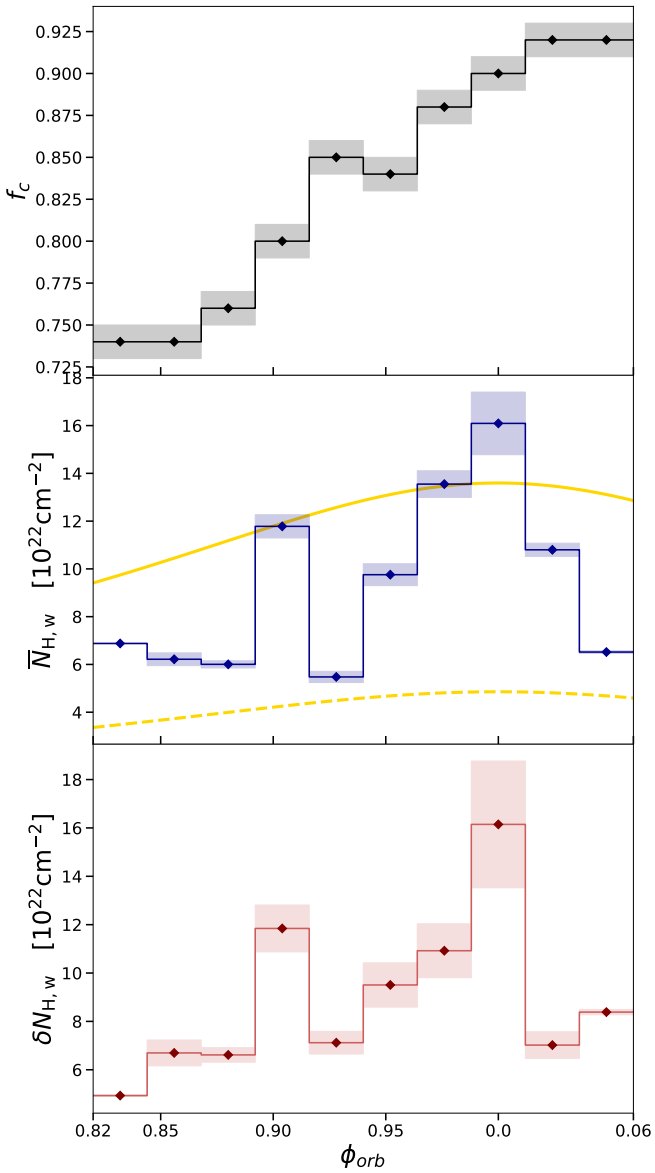


Figure 5.8: Stellar wind parameters as inferred from the fit of the time-resolved colour-colour diagrams of observation 201, as a function of the orbital phase (see also Tab. 5.1). The covering factor $f_c$ is shown in the upper panel, while the middle and bottom panels show the mean column density $\overline{N}_{\mathrm{H,w}}$ and the scatter in column density parameter $\delta N_{\mathrm{H,w}}$, respectively. The 68% confidence contours are reported as shaded areas. The yellow curves are the neutral column density profiles resulting from the smooth wind model of El Mellah et al. 2020 at low (dashed) and high (solid) stellar mass loss rates.

contribution from a dust scattering halo (e.g. Nowak et al., 2011).

Results obtained by Hirsch et al. (2019) support the former possibility. The authors revealed the presence of an emission line spectrum from the photoionised plasma around the BH, that can be clearly observed only when the X-ray source is highly absorbed (down in the dips). However, we cannot exclude that a dust scattering halo gives an additional contribution to the soft tail. Source photons intercepted by foreground interstellar dust along the LOS are scattered away, resulting in a dimming of the source. However, interstellar dust grains outside the LOS can redirect photons back to the observer, creating a halo around the source. Since the dust scattering cross-section (Corrales et al., 2016) is energy dependent, soft X-ray photons will have a higher chance to be scattered back, thus producing an excess of soft X-ray flux (Maeda et al., 1996).

In order to investigate the presence of a dust scattering halo component in the *XMM-Newton* EPIC-pn data of Cyg X-1, we followed the approach of Jin et al. (2017), and checked whether the spectrum softens significantly when extracting photons from increasingly more external regions. It should be emphasized that the timing mode does not permit to select regions totally unaffected by a dust scattering halo since all pixels in the same column lose their spatial information along RAWY. Nevertheless, for a bright X-ray source, if a scattering halo is present, the inner columns will still be harder than the external columns since the the X-ray source dominates the central columns and the halo dominates the external ones.

Therefore, we extracted spectra in the 2–10 keV energy band only during the time interval ∼82–94 ks, since this selects the passage at superior conjunction, and the halo emission is expected to be more significant when the X-ray source is highly absorbed (e.g. Jin et al., 2018). We then selected three detector regions. We chose them to be at increasingly higher distance from the central pixels. We discarded the central RAWX= [36 : 39] to avoid pile-up effects (Sect. 5.2). The chosen regions are: RAWX = [32 : 35]–[40 : 43] (covering an angular diameter D = 8”–16” from the central pixel), RAWX = [30 : 32]–[43 : 46] (D = 16”–32”) and RAWX = [27 : 30]–[46 : 49] (D = 32”–44”). Fitting the spectra with a power law, we observe a gradual softening of the $\Gamma$ parameter, up to ∼10% in the most external region (Fig. 5.9). More specifically, we find $\Gamma = 1.42 \pm 0.01$ for RAWX = [32 : 35]–[40 : 43], $\Gamma = 1.54 \pm 0.01$ for RAWX = [30 : 32]–[43 : 46], and $\Gamma = 1.58 \pm 0.01$ for RAWX = [27 : 30]–[46 : 49]. This gradual softening suggests the presence of a dust scattering halo component. Therefore, we conclude that the dust scattering halo can potentially contribute to the soft tail seen in the colour-colour diagrams of Cyg X-1. Nevertheless, we highlight that both a dust scattering halo and a stellar wind emission line component would contribute the most when the source is highly absorbed. Therefore, we expect a soft tail to be particularly prominent when the data do not populate the uppermost part of the colour-colour

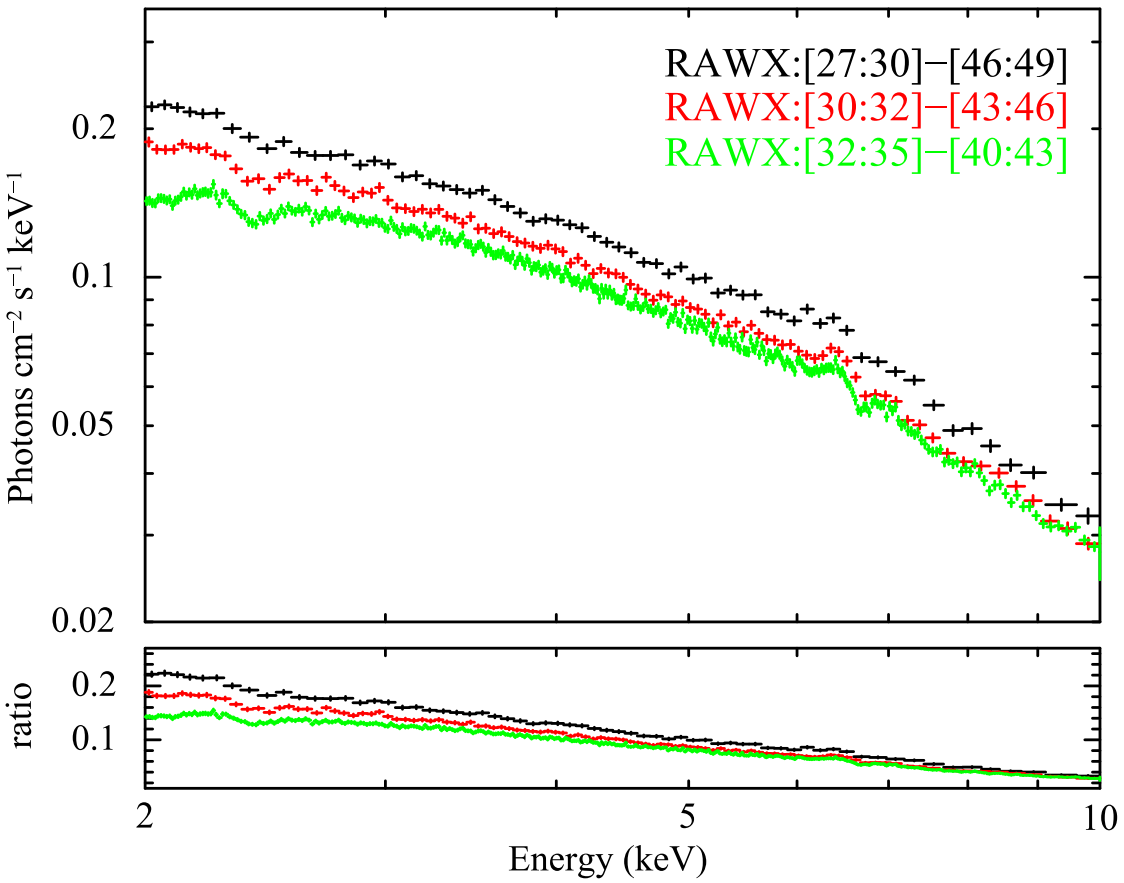


Figure 5.9: Unfolded (against a constant model fixed at 1) EPIC-pn spectra (upper panel) in the 2–10 keV energy band. Spectra were extracted in the time interval $t \sim$ 82–94 ks, covering the passage at superior conjunction. Labels report the chosen RAWX selections for each spectrum. The softening of the spectra, suggesting a dust scattering halo contribution, is easily visible in the ratios (bottom panel).

diagram. Indeed, all the observed time-resolved colour-colour diagrams follow these expectations (for a better visualisation see Fig. E.1). However, panel "i", corresponding to $\phi_{\rm orb} = 0.012$–$0.036$, does not show a prominent soft tail despite being highly absorbed ($\overline{N}_{\rm H,w} \sim 10.80 \times 10^{22}\,{\rm cm}^{-2}$ and $f_c \sim 0.92$). We think that this might be related to a delayed response of the illuminated dust halo or emission line region to a change of the irradiating flux from the X-ray source (see Fig. 5.1).

## 5.5 Discussion

As demonstrated by several studies (e.g. Grinberg et al., 2015; Miškovičová et al., 2016; Hirsch et al., 2019; Grinberg et al., 2020), the stellar wind in Cyg X-1 is highly complex. The passage of dense wind clumps (e.g. Owocki et al. 1988; Feldmeier et al. 1997; Oskinova et al. 2012; Sundqvist and Owocki 2013) across our LOS induces stochastic variability, resulting in absorption dips in the X-ray light curves. This absorption variability adds up to the variability intrinsic to the X-ray source (see Ch. 4). Absorption dips are more prominent close to superior conjunction (see Sect. 2.5, e.g. Bałucińska-Church et al. 2000), as the LOS crosses deeper wind layers in these phases.

In this work, we modelled colour-colour diagrams to characterise the stellar wind in Cyg X-1 in its hard state during a passage at superior conjunction (covering orbital phases between 0.82 and 0.06, see Fig. 3.1 and Fig. 5.1). In the hard state, the high occurrence of absorption dips, rather than in softer states, can be explained as due to the X-ray source not being strong enough to completely ionise the stellar wind (e.g. Grinberg et al., 2015; Miškovičová et al., 2016). A novelty with respect to previous studies is the fact that we used a non-parametric fitting method (Sect. 5.3.3) to find the best-fit model and constrain the physical parameters of the stellar wind (Sect. 5.3.3 and Sect. 5.4).

### 5.5.1 Evolution of stellar wind parameters

Our study corroborates the hyphothesis that the characteristic "pointy" or "nose-like" shape of the colour-colour tracks requires the absorbing wind to be partially ionised (Sect. 5.3.2, see also Grinberg et al. 2020 who analysed an observation from *Chandra* from 2004 of Cyg X-1 covering similar orbital phases). This is in agreement with previous and independent results obtained via high resolution spectroscopy (e.g. Hanke et al., 2009; Miškovičová et al., 2016). Specifically, Hirsch et al. (2019) showed that different levels of ionisation are required to explain absorption features at different dip stages. This indicates an (unknown) functional dependence of the ionisation parameter $\log \xi$ on the column density of the absorbing gas $N_{\mathrm{H,w}}$ (Grinberg et al., 2020). In our work, we tested two empirical functions (Sect. 5.3.3): one assuming a linear scaling between the two parameters, and the other allowing for additional sources of ionisation at high column densities (Fig. 5.5). Despite the fact that the data do not allow one particular empirical function to be statistically preferred with respect to the other, simulations (Feldmeier et al., 1997; Sundqvist and Puls, 2018) indicate that collisions in the ambient stellar wind occurring in denser regions (high $N_{\mathrm{H,w}}$ regime) are expected to induce significant X-ray emission. This emission can contribute to further ionise the gas.

In order to constrain the stellar wind evolution as a function of the orbital phase

close to superior conjunction, we extracted time-resolved colour-colour diagrams and fit them with a continuum plus variable ionisation model (see Sect. 5.4). Our fits reveal that the covering factor $f_c$ steadily increases by a factor $\sim$1.2 between $\phi_{\rm orb} \sim 0.8$ and $\phi_{\rm orb} \sim 0$, remaining high also after the passage at superior conjunction (up to at least $\phi_{\rm orb} \sim 0.06$, top panel of Fig. 5.8 and Tab. 5.1). On the contrary, the mean column density $\overline{N}_{\rm H,w}$ displays two peaks: one at $\phi_{\rm orb} \sim 0.9$ and the other right at superior conjunction ($\phi_{\rm orb} = 0$). Later in the orbit, $f_c$ remains high, while $\overline{N}_{\rm H,w}$ drops to a minimum (middle panel of Fig. 5.8 and Tab. 5.1). We also measured the scatter parameter $\delta N_{\rm H,w}$, which is a diagnostic of the amount of $N_{\rm H,w}$ variability for each time-resolved colour-colour diagram (bottom panel of Fig. 5.8 and Tab. 5.1). This parameter follows the same behaviour as $\overline{N}_{\rm H,w}$ (see also Fig. 5.10). Considering the sampling we chose to extract the time-resolved colour-colour diagrams (i.e. 10 segments of $\sim$11 ks), while the inferred $\overline{N}_{\rm H,w}$ parameter is sensitive to relatively long term modulations, the $\delta N_{\rm H,w}$ parameter is sensitive to more rapid variability (from 10 s, the time resolution we used to calculate the colour-colour diagrams, to $\sim$11 ks) likely driven by the smallest-scale inhomogeneities in the stellar wind. Our study points to a one-to-one relation between the amount of absorption at a given orbital phase and its associated rapid variability. In other words, the higher the $\overline{N}_{\rm H,w}$, the higher its scatter $\delta N_{\rm H,w}$ (see Fig. 5.10). This relation is reminiscent of the "rms-flux" relation characterising the stochastic flux variability in systems containing a compact object (e.g. Uttley et al., 2005; Scaringi et al., 2012). The latter implies the flux to be log-normally distributed, and the variability across different timescales to combine multiplicatively (Uttley et al., 2005). Since the observed column density is influenced by the size of the clumps, if confirmed, the $\overline{N}_{\rm H,w}$ versus $\delta N_{\rm H,w}$ relation could have implications on the clump sizes distribution and on the way they merge to form bigger clumps.

### 5.5.2 Estimate of the mass loss rate and the mass of the clumps

Variations of the absorbing column density of the stellar wind can occur because of two reasons. First of all, periodic variations due to the orbital motion of the BH around its stellar companion are expected. This gives rise to smooth variations of the absorbing column, and is well captured by models of smooth winds. However, it cannot explain any stochastic variability occurring on timescales much shorter than the orbital period. The latter is induced by clumps crossing the LOS to the BH (El Mellah et al., 2020), thus capturing the inhomogeneities in the wind. In this context, the average column density ($\overline{N}_{\rm H,w}$) time series matches the mass loss rate of a smooth wind, while the dispersion around the average value ($\delta N_{\rm H,w}$) provides information on the properties of the clumps.

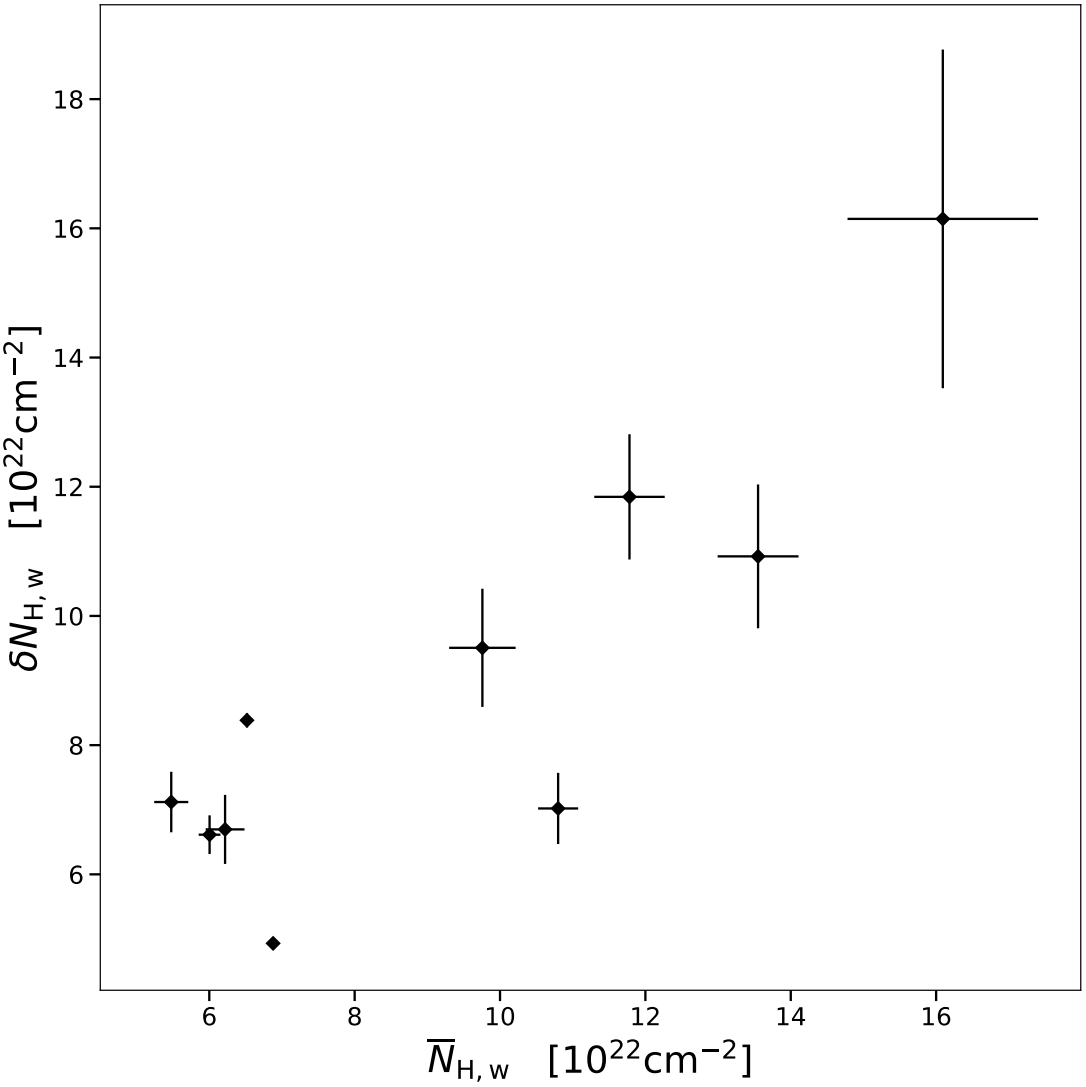


Figure 5.10: Relation between the measured $\overline{N}_{\mathrm{H,w}}$ and $\delta N_{\mathrm{H,w}}$ parameters. The single parameters respectively sample the long-term and rapid variations of the stellar wind column density (see Tab. 5.1).

The small portion of the orbital period covered by the observation analysed in this paper does not allow us to constrain the periodic variations of column density. Therefore, in the middle panel of Fig. 5.8, we plotted the expected periodic component of the column density due to the orbital motion (yellow lines) for two different values of stellar mass loss rate. For this computation we made use of the smooth and spherically-symmetric stellar wind model developed by El Mellah et al. (2020). This model accounts for all the material along the LOS between the observer and the BH, independently of its ionisation state, thus, it is an estimate of the neutral column density, resulting necessarily higher than the measurable ionised column density. Neglecting the orbital eccentricity and assuming a $\beta$-law for the wind velocity profile, the shape of the neutral column density curve only depends on three parameters: the orbital inclination $i$, the ratio of the orbital separation $d$ to the stellar radius $R_*$ and on the $\beta$ exponent of the velocity profile. We considered $i = 27°$ and $d/R_* = 2.3$ (corresponding to the values of Miller-Jones et al. 2021), and $\beta = 1.5$, a characteristic value for UV-line driven winds of O supergiants (Rubio-Díez et al., 2022). Given the low inclination of Cyg X-1, the peak-to-peak variation is modest along the orbit and we do not expect significant changes for realistic values of $d/R_*$ and $\beta$. On the contrary, the scale of the neutral column density curve is given by $\dot{M}_*/(m_p v_\infty R_*)$, with $\dot{M}_*$ representing the stellar mass loss rate and $m_p$ the proton mass. We considered $v_\infty = 2100\,\mathrm{km\,s^{-1}}$ (Herrero et al., 1995) and $R_* = 22\ R_\odot$ as reported by Miller-Jones et al. (2021). Gies et al. (2003) inferred a stellar mass loss rate $\dot{M}_* \sim 2.6 \times 10^{-6}\ \mathrm{M_\odot\,yr^{-1}}$ in the hard state via $H\alpha$ diagnostics. Nevertheless, this estimate does not take ionisation into account, and makes use of the stellar parameters used by Herrero et al. (1995), which differ from the updated values. Therefore, we think that this estimate for the mass loss rate could be underestimated. As a matter of fact, the neutral column density profile corresponding to $\dot{M}_* \sim 2.6 \times 10^{-6}\ \mathrm{M_\odot\,yr^{-1}}$ (dashed yellow line) lies below our data points. However, since the data correspond to the absorbing column density (i.e. only the gas in an ionisation state low enough to contribute to absorption), while the smooth profile of the model accounts for the neutral column density, the latter should represent an upper limit. Therefore, we deduce that a higher value of stellar mass loss rate, for example $\dot{M}_* \sim 7 \times 10^{-6}\,\mathrm{M_\odot\,yr^{-1}}$ (solid yellow line), is more compatible with the values of column density measured at superior conjunction. To obtain better constraints, the variations of $\overline{N}_{\mathrm{H,w}}$ should be sampled over longer periods, ideally covering multiple consecutive orbits.

In addition, our analysis revealed significant short-term variability of both the $\overline{N}_{\mathrm{H,w}}$ and the $\delta N_{\mathrm{H,w}}$ parameters (Fig. 5.8). El Mellah et al. (2020) developed a model which explores the effects of the clumpiness of the stellar wind on the rapid time-variability of its column density. The authors also explores the ways such variability can be used to infer the physical properties of the clumps, such

as their size and mass. In the clumpy wind model of El Mellah et al. (2020), the clumps' properties are directly connected to the scatter parameter $\delta N_{\rm H,w}$. In their simulations, this parameter reaches a maximum at superior conjunction as indeed observed (Tab. 5.1 and lower panel of Fig. 5.8). An additional prediction of the model is that the scatter is an excellent tracer of the ratio $\sqrt{m_{cl}}/R_{cl}$, where $m_{cl}$ and $R_{cl}$ are the mass and radius of the clumps, respectively. In Ch. 4, Sect. 4.6.1, we estimated a clump radial size of $\gtrsim 10^{-4}\ R_*$, based on the measurement of the the minimum timescales at which the passage of clumps induces significant excess X-ray variability in the power spectra of Cyg X-1. Using the estimated value of $\sim 10^{-4}\ R_*$ as the smallest clumps radius, the measured maximum value of $\delta N_{\rm H,w}$ (Tab. 5.1), and the value of the mass loss rate inferred above, and plugging them into equation 18 of El Mellah et al. (2020) we found $m_{cl} \sim 10^{17}$ g as an estimate for the mass of the clumps (for $v_\infty = 2100\,{\rm km\,s^{-1}}$ and $R_* = 22\ R_\odot$). The estimated value is in agreement with the values found through radiative hydrodynamical simulations (Sundqvist et al., 2018), as well as from spectral analysis (Härer et al., 2023).

### 5.5.3 Comments on the soft-colour tail

The observed colour-colour diagrams also show an extended soft-colour tail, which is consistent with the presence of a soft emission component in the most absorbed stages. We found (Sect. 5.4.1) that the analysed *XMM-Newton* data are consistent with being affected by a significant contribution from a dust scattering halo (e.g. Jin et al., 2017). Nevertheless, we expect also an additional contribution from the stellar wind itself, manifesting as emission lines from the diffused photoionised gas around the BH (Hirsch et al., 2019). Both contributions should be particularly prominent when the primary X-ray source radiation is significantly blocked by the absorbing material, i.e. in the dips deepest stages. A more complex modelling approach is needed to disentangle the two contributions, but this goes beyond the scope of this work.

As a final remark, it is important to notice that our modelling of the colour-colour diagrams does not take into account the possibility of additional spectral changes extrinsic to the wind i.e. intrinsic changes of the hard X-ray source properties. As an example, rapid changes in either the temperature or the optical depth (or both) of the Comptonising gas would induce time variability of the spectral index $\Gamma$, which would manifest as changes in the colour of the source. Indeed, in Sect. 5.4, we showed that changes in hard and soft colours in the unabsorbed part of the diagrams (upper region) can be ascribed to spectral variability. Mastroserio et al. (2021) found that in hard state sources with measured fractional rms variability of $\sim$10%, $\Gamma$ variability of a few percents is plausible. Skipper et al. (2013) inferred a larger $\Gamma$ variability ($\sim$10%) for the same source and spectral

state. However, the impact of these spectral changes on the most absorbed parts of the diagram is yet to be tested.

# Chapter 6

# Conclusions and future perspectives

The primary goal of this dissertation is the study of the X-ray variability of the stellar wind in the HMXB Cyg X-1 and of its physical properties. In this chapter, we summarise the key results of our work and outline future perspectives.

In Ch. 4 we investigated the effects of the stellar wind on the observed X-ray spectral-timing properties of Cyg X-1, particularly focusing on the short timescales ($< 10\,\mathrm{s}$). Using *XMM-Newton* data from the CHOCBOX campaign (Sect. 3.1) we were able to observe two consecutive passages at superior conjunction (i.e. $\phi_{orb} = 0$), which represent the orbital phase most affected by absorption dips caused by the stellar wind (see Figs. 4.1 and 5.1). Our main findings from the work described in Ch. 4 are as follows:

- The orbital phases close to superior conjunction exhibit the strongest absorption events, which result in a significant modification of the observed X-ray variability power spectral density of the source. In particular, we observe an increase of the low-frequency ($\lesssim 1\,\mathrm{Hz}$) X-ray fractional variability power and a suppression at the highest frequencies ($\gtrsim 1\,\mathrm{Hz}$). As a result, the double-hump power spectrum shape, typical of the hard state of Cyg X-1, is smoothed out when the source approaches superior conjunction.

- We attribute the increased low-frequency fractional variability to changes of the column density of the intervening material, likely as a consequence of the motion of the clumps crossing our LOS. Assuming a terminal wind speed of $2400\,\mathrm{km\,s^{-1}}$, the observed timescales suggest clumps radial sizes of $0.5\text{–}1.5 \times 10^{-4} R_*$.

- The decrease in high-frequency fractional variability during the most absorbed orbital phases suggests the presence of a scattering medium, optically thicker than the stellar wind. We associate this component with an accretion bulge, likely resulting from the collision of the stellar wind with the outer

edge of the accretion disc. The presence of an accretion bulge had been proposed in the past for both Cyg X-1 and Cyg X-3 (Poutanen et al., 2008; Zdziarski et al., 2010).

- The most absorbed orbital phases are also characterised by suppression of the intrinsic coherence between soft (absorption-dominated) and hard (primary continuum-dominated) light curves. We ascribe the drop in coherence to non-linear variability of the absorbing material. Additionally, a long, low-frequency soft lag emerges during the most absorbed phases, which we interpret as due to large-scale reprocessing or recombination within the stellar wind. If absorption dips are not filtered out, the soft lag contributes to reduce the amplitude of the typical hard X-ray lags intrinsic to the broad band continuum.

In Ch. 5 we carried out an analysis of the short-time scale X-ray spectral variability of Cyg X-1 during the most absorbed observation of the *XMM-Newton* CHOCBOX monitoring (Sect. 3.1 and Fig. 5.1), with the goal of constraining physical parameters of the wind (such as column density, covering factor), and track their evolution. To this aim we performed a detailed modelling of the total and the time-resolved colour-colour diagrams of the observation (Sect. 3.3), and made use of the KDE method (Sect. 5.3.3) to select the best-fit models. This fitting approach allowed us to overcome issues related to non-normally distributed data. The main results are as follows:

- We confirmed that the model that best describes the characteristic "pointy" or "nose-like" shape of the colour-colour diagrams of Cyg X-1 requires the stellar wind to be partially ionised (Sects. 5.3.2 and 5.3.3).

- The shape of the colour-colour diagram strongly evolves over time around superior conjunction. Our analysis suggests that this evolution is driven by concurrent variations of the column density and covering factor of the stellar wind (Sect. 5.4). At superior conjunction, both the column density and the covering factor peak, as the LOS crosses deeper wind layers. However, their overall variations follow different trends.

- We discovered a one-to-one scaling between the long-term ($> 11$ ks) and the rapid (between 10 s and 11 ks) variations of the column density, resembling the "rms-flux" relation characterising the stochastic flux variability in compact objects. This correlation could have implications on the wind clumps size distribution and on the way they combine to form bigger clumps.

- Making use of El Mellah et al. (2020)'s clumpy wind model, we were able to estimate a wind mass loss rate of $\dot{M}_* \sim 7 \times 10^{-6}$ $\mathrm{M_\odot\,yr^{-1}}$ and a characteristic clump mass of $m_{cl} \sim 10^{17}$ g.

In the future, we plan to extend our analysis of colour-colour diagrams to the full *XMM-Newton* monitoring, in order to characterise the temporal evolution of the stellar wind physical parameters over an entire orbit of the binary system. Additional observations at superior conjunction (e.g. using available *NICER* data) will help track changes of the stellar wind across different orbits, as well as different accretion states of the X-ray source, thus providing deeper insights into the properties and size distribution of the clumps, and, possibly, over their growth mechanism.

This thesis also demonstrates the effectiveness of X-ray spectral-timing techniques for the study of stellar winds. Since, as also demonstrated in this thesis, wind clump absorption events can be quite short ($\lesssim$1 ks), these techniques overcome the limitations of standard time-resolved spectroscopic analysis, which require a high number of collected photons over the relevant timescales to achieve meaningful results. Before larger effective area, higher spectral resolution instruments (e.g. the X-IFU on board *NewAthena*) will be available, these techniques may be the most reliable method for probing short-lived absorption events, enabling us to extract valuable information about wind structure and variability with current observational capabilities.

# Appendices

# Appendix A

## Modelling the colour-colour diagram of observation 201

Using a simple absorption model, we modelled the colour-colour diagram calculated for each observation of Cyg X-1. As an example, here we report the results obtained for the first observation of the monitoring: observation 201. To model the continuum, we made use of `Xspec` using a partially absorbed power law with spectral index 1.7 (`tbpcf` $\times$ `powerlaw`). The covering fraction was fixed at 0.9 and let the wind column density of the stellar wind $N_{\mathrm{H,w}}$ to vary (from $0.1 \times 10^{22}\,\mathrm{cm}^{-2}$ to $3.5 \times 10^{23}\,\mathrm{cm}^{-2}$). This allowed us to calculate the colour-colour diagram track shown in Fig. A.1, over plotted to the data. We also included the ISM absorption (`TBnew`) in the model, with Galactic $\mathrm{N_H} = 0.7 \times 10^{22}\,\mathrm{cm}^{-2}$ (Basak et al., 2017; HI4PI Collaboration et al., 2016) using abundances from Wilms et al. (2000). For this model, the hard and soft colours threshold we used in Sect. 4.2.1 to exclude data characterised by strong wind absorption corresponds to a wind column density of $N_{\mathrm{H,w}} \geqslant 1.08 \times 10^{22}\mathrm{cm}^{-2}$ for a covering factor of 0.9.

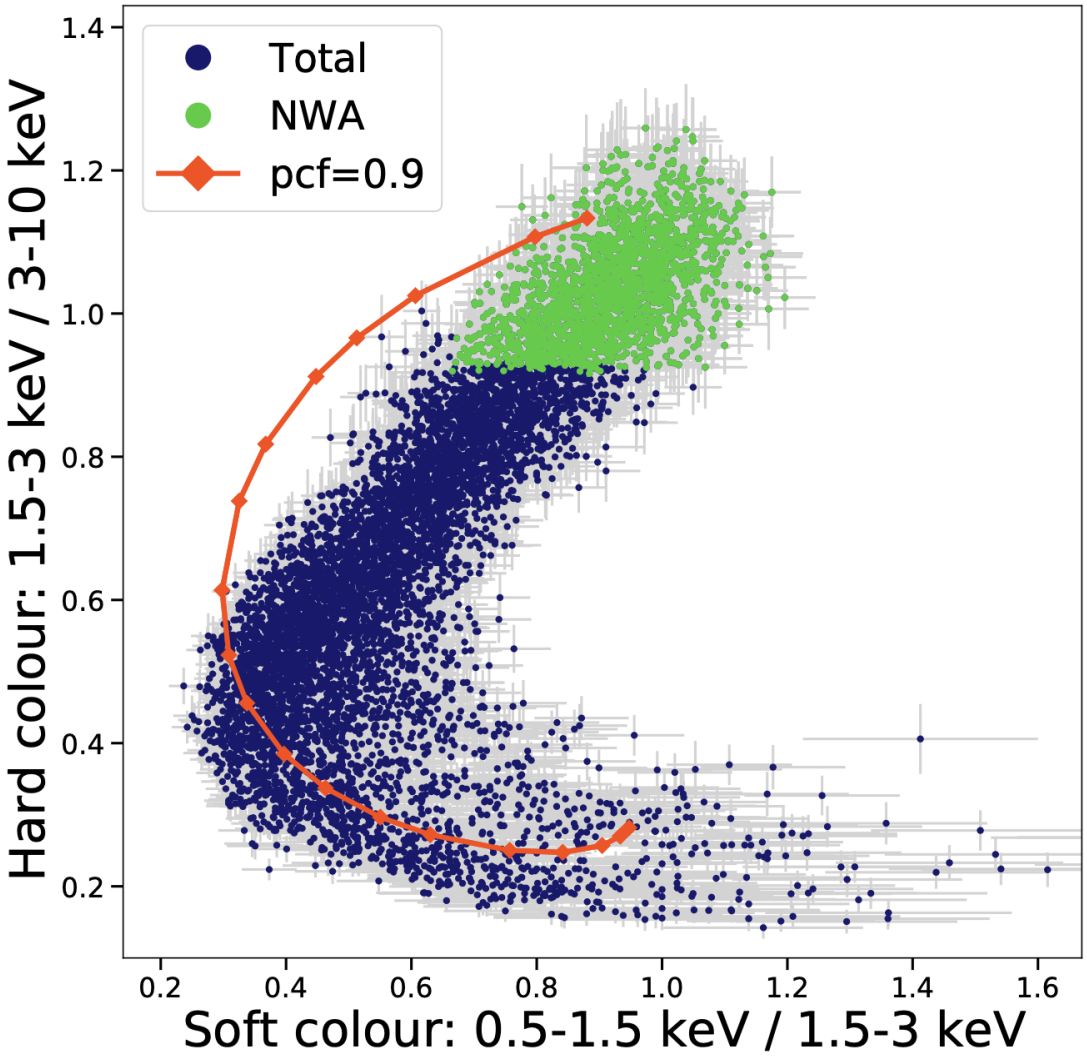


Figure A.1: Colour-colour diagram of observation 201 (in blue for the Total data set selection and in green for the NWA data set one, see Sect. 4.2.1) and associated simulated track obtained using a simple model (`TBnew` × `tbpcf` × `powerlaw` in `Xspec`) for a partial covering factor of 0.9 (in red). Each red point on the model curve corresponds to a different value of $N_{H,w}$ (starting from $0.1 \times 10^{22}\,cm^{-2}$, on the top, to $3.5 \times 10^{23}\,cm^{-2}$, on the bottom, arbitrarily spaced).

# Appendix B

## Selection of the NWA data set for observation 701

We verified that a tighter selection than the one used in Sect. 4.2.1) for hard and soft colours permits to recover the double-hump shape of the power spectrum in observation 701 (comprising the second passage at superior conjunction for the monitoring). For this selection, we chose hard colours $\geqslant 1.05$ and soft colours $\geqslant 1$. Results are shown in Fig. B.1.

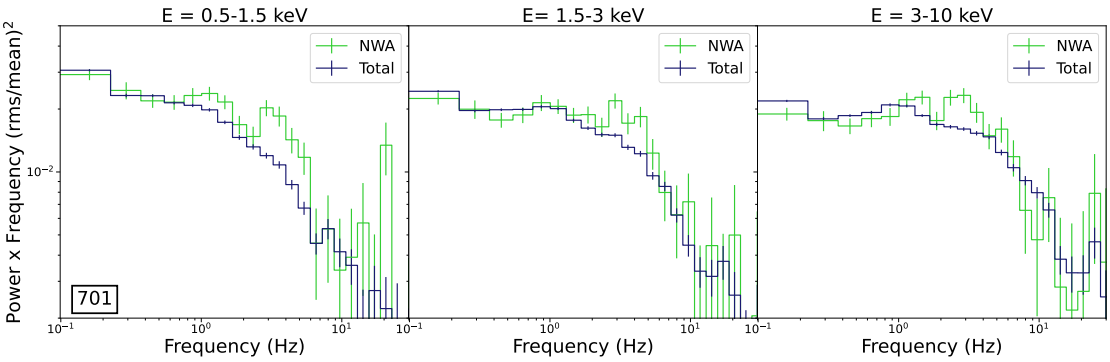


Figure B.1: Power spectra of observation 701 after selection of data sets characterised by hard colour $\geqslant 1.05$ and soft colour $\geqslant 1$ for the Total (in blue) and the NWA (in green) data sets, in the analysed energy bands: soft, intermediate and hard.

# Appendix C

## Parameters for the spectral fitting

In Tab. C.1 we report best-fit parameters of the broad band continuum for the model `Tbnew` × `[diskbb + nthComp + relxillCp]`. Spectra of all the *XMM-Newton* observations of Cyg X-1 were fitted jointly (see Sect. 4.4).

Table C.1: Best-fit parameters obtained from the spectral analysis for each *XMM-Newton* observations of Cyg X-1. The $kT_{in}$ parameter is the inner temperature of the accretion disc and the $kT_e$ one is the electron temperature of the soft Comptonisation component. The $\Gamma_S$ and $\Gamma_H$ parameters are the spectral indexes of the soft and hard Comptonisation components, respectively. Errors were calculated within a confidence level of 90%. Unconstrained parameters, indicated with $f$, were kept fixed at the best-fit value.

| Component | Parameter | 201 | 501 | $601_{\rm A}$ | $601_{\rm B}$ | 701 |
|---|---|---|---|---|---|---|
| `diskbb` | $kT_{in}$ (keV) | $0.18^{+0.01}_{-0.01}$ | $0.19^{+0.01}_{-0.01}$ | $0.17^{+0.01}_{-0.01}$ | $0.17^{+0.01}_{-0.01}$ | $0.20^{+0.01}_{-0.01}$ |
| `nthComp` | $\Gamma_S$ | $2.02^{+0.04}_{-0.04}$ | $1.68^{+0.08}_{-0.02}$ | $2.23^{+0.01}_{-0.03}$ | $2.51^{+0.09}_{-0.02}$ | $1.35^{+0.08}_{-0.04}$ |
| | $kT_e$ (keV) | $0.80^{+0.02}_{-0.04}$ | $1^f$ | $1^f$ | $1^f$ | $< 0.77$ |
| `relxillCp` | $\Gamma_H$ | $1.38^{+0.02}_{-0.02}$ | $1.32^{+0.04}_{-0.02}$ | $1.35^{+0.02}_{-0.02}$ | $1.42^{+0.04}_{-0.05}$ | $1.38^{+0.02}_{-0.01}$ |

# Appendix D

## Complex underlying continuum modelling

In Sects. 5.3.2 and 5.3.3 we made use of a complex primary continuum for our simulations. Although in our previous work we jointly fitted all the observations of the *XMM-Newton* CHOCBOX monitoring (see Sects. 4.2.1 and Appendix C), in this work we redo the spectral fitting focussing only on observation 201 starting from that model: `TBabs` × `[diskbb + nthComp + relxillCp]` in `Xspec`. Similar to what we have previously done, the BH spin was frozen at the maximum value $a = 0.998$, allowing the inner disc truncation radius to span the largest range of values, the inclination of the reflector $i$ at 27° (Miller-Jones et al. 2021, see also results by Krawczynski et al. 2022 and Poutanen et al. 2023) and the high-energy cut-off of the hard Comptonisation component at 100 keV (Basak et al., 2017). We tied the seed photon temperature of the soft Comptonisation component to the best-fit inner disc temperature of the `diskbb` component.

We fitted the spectrum of observation 201 considering only the data set not affected by wind absorption (i.e. NWA, see Sect. 4.2.1). Narrow residuals are still present after the fitting, primarily between ∼0.5–2.5 keV, close to the absorption edges of the response matrix (i.e. at $E \approx 0.528$ keV and $E \approx 1.83$–$1.87$ keV), thus probably related to calibration problems. We therefore modified the response matrix to account for these residuals via the `Xspec` function `gain`. This allows us to change the slope or the intercept of the effective area curve. We did this, shifting the energies at which the response matrix is defined. We introduced a linear gain shift (`intercept` parameter in `Xspec`) of 0.01 keV (`slope` parameter of `gain` fixed to 0). This improved the best-fit (from $\chi^2/\mathrm{dof} = 4404.17/1891$ to $\chi^2/\mathrm{dof} = 3923.7/1891$, see Fig. D.1).

Nevertheless, some residuals were still present, accompanied to a strong narrow excess in the Fe K$\alpha$ region. Therefore, to take into account for these remaining features, we included to the model narrow ($\sigma < 0.1$ keV) emission and absorption gaussian components (see Tab. D.1). Although we did not investigate their nature, we point out that these features could be related to incorrect calibration or residual wind absorption from the selection process of the NWA GTIs (see Sect. 4.2.1).

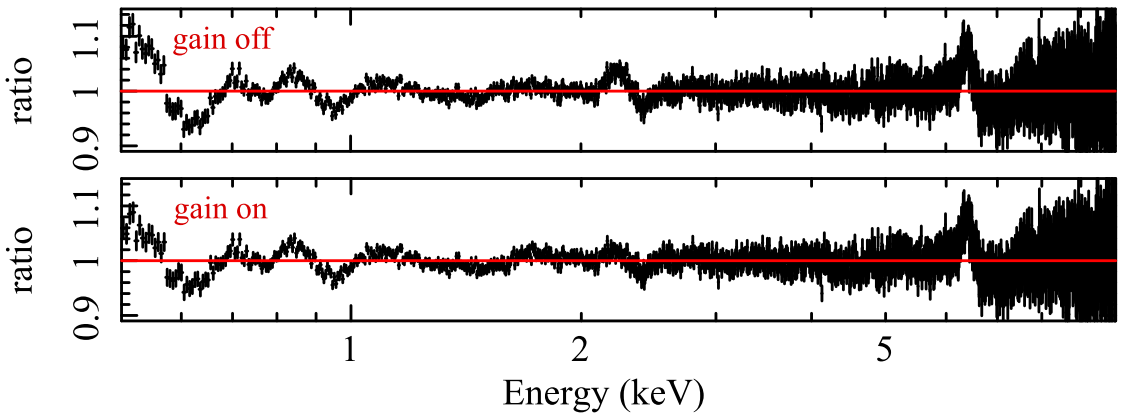


Figure D.1: Data to model ratios before (upper panel) and after (bottom panel) using the `gain` correction (`intercept` parameter set to 0.01 keV and `slope` parameter fixed to 0).

The presence of the narrow feature appearing in the Fe K$\alpha$ region might suggest the need to include a second reflection component (such as from the outer disc) to obtain a better description of the broad band continuum. Nevertheless, we highlight that our analysis, focussing on testing the effects of variable absorption on the colour-colour tracks, is not strongly influenced by the continuum model's details as long as it gives a good characterisation of the broad-band spectrum.

The final best-fit model yields $\chi^2$/dof = 2263.76/1873. Fig. D.2 shows the NWA spectrum of observation 201 and the obtained best-fit model. The most relevant parameters are listed in Tab. D.1.

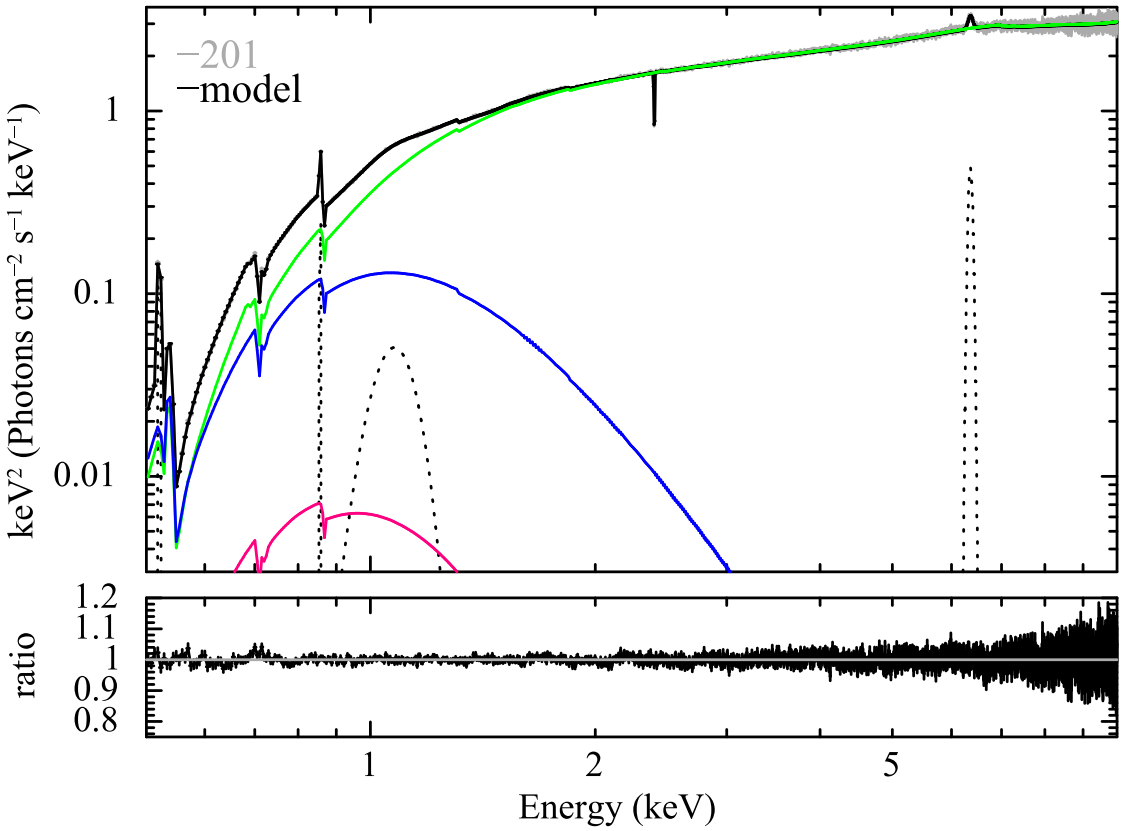


Figure D.2: Best-fit model of the NWA time-averaged spectrum of observation 201. We show the complex best-fit model in black and the single components in different colours: in magenta the disc blackbody, in blue the soft excess, in green the hard Comptonisation component and its relative reflection and in dotted grey the additional gaussians. Bottom panel shows the ratios data to best-fitting model.

Table D.1: Parameters obtained from the best-fit of the continuum model of the NWA spectrum of observation 201. The errors are at the 90% confidence level, i.e. $\Delta\chi^2 = 2.71$.

| | Component | Parameter | Value |
|---|---|---|---|
| ISM absorption | `TBabs` | $N_{\rm H}$ ($10^{22}{\rm cm}^{-2}$) | $0.79^{+0.01}_{-0.02}$ |
| `continuum` | `diskbb` | $kT_{bb}$ (keV) | $< 0.14$ |
| | `nthComp` | $\Gamma$ | $< 5.9$ |
| | | $kT_e$ (keV) | $> 0.67$ |
| | `relxillCp` | $R_{in}$ ($R_{\rm g}$) | $13.24 \pm 1.26$ |
| | | $\Gamma$ | $1.59 \pm 0.01$ |
| | | $\log_{10}\xi$ | $3.32 \pm 0.01$ |
| | | $A_{Fe}$ | $1.01^{+0.05}_{-0.02}$ |
| | | $\mathcal{R}$ | $0.52^{+0.01}_{-0.03}$ |
| `absorption features` | `gau1` | $E_l$ (keV) | $1.44 \pm 0.01$ |
| | `gau2` | $E_l$ (keV) | $2.40 \pm 0.01$ |
| `emission features` | `gau3` | $E_l$ (keV) | $6.36 \pm 0.01$ |
| | `gau4` | $E_l$ (keV) | $0.52 \pm 0.01$ |
| | `gau5` | $E_l$ (keV) | $0.86 \pm 0.01$ |
| | `gau6` | $E_l$ (keV) | $1.05 \pm 0.01$ |

# Appendix E

## Best-fit models of the time-resolved colour-colour diagrams

We report the time-resolved colour-colour diagrams of observation 201 (with the same colour code as in Fig. 5.6), and the best-fit models (obtained from the fits discussed in Sect. 5.4) in Fig. E.1.

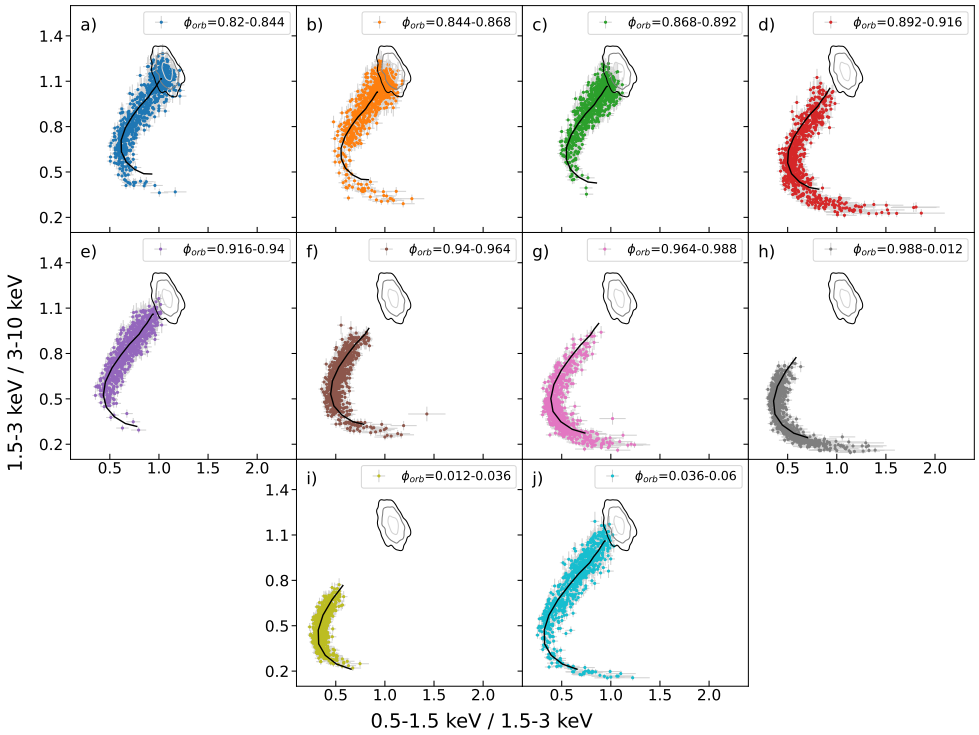


Figure E.1: Time-resolved colour-colour diagrams of observation 201 (colour-coded as in Fig. 5.4). Best-fit models tracks are over plotted in black. They were obtained assuming $\log \xi = \log \frac{10+[N_{\rm H,w}/10^{22}\ {\rm cm}^{-2}]}{[N_{\rm H,w}/10^{22}\ {\rm cm}^{-2}]} + 1$. The grey-shaded curves are the 99.7% (in black), 95% (in grey) and 68% (in light grey) confidence levels of the data distribution during the least absorbed stages of the orbit, close to inferior conjunction ($\phi_{\rm orb} = 0.43 - 0.46$, see Appendix F).

# Appendix F

## Probability distribution near inferior conjunction

We report the colour-colour diagram calculated from orbital phases $\phi_{\rm orb} = 0.43$–$0.46$, during observation 501. These phases were taken into account as they are the closest to inferior conjunction (i.e. $\phi_{\rm orb} \sim 0.5$), thus the least affected by wind absorption. Using the KDE method, we computed the probability distribution for this data set (Sect. 5.4). Fig. F.1 shows the resulting 99.7%, 95% and 68% confidence contours over plotted to the data.

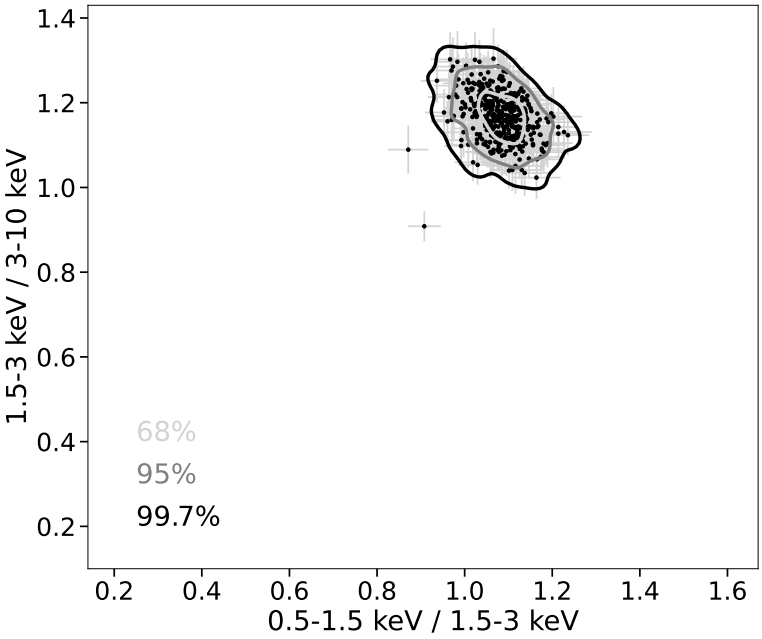


Figure F.1: Colour-colour diagram and probability distribution map for orbital phases between 0.43 and 0.46. The gray-shaded curves highlight the 99.7% (in black), 95% (in grey) and 68% (in light grey) confidence regions.

# Bibliography

*"XMM-Newton Users Handbook",* Issue 2.22,. 2024. (ESA: XMM-Newton SOC).

P. Arévalo and P. Uttley. Investigating a fluctuating-accretion model for the spectral-timing properties of accreting black hole systems. *MNRAS*, 367(2): 801–814, April 2006. doi: 10.1111/j.1365-2966.2006.09989.x.

K. A. Arnaud. XSPEC: The First Ten Years. In George H. Jacoby and Jeannette Barnes, editors, *Astronomical Data Analysis Software and Systems V*, volume 101 of *Astronomical Society of the Pacific Conference Series*, page 17, January 1996.

Astropy Collaboration, Thomas P. Robitaille, Erik J. Tollerud, Perry Greenfield, Michael Droettboom, Erik Bray, Tom Aldcroft, Matt Davis, Adam Ginsburg, Adrian M. Price-Whelan, Wolfgang E. Kerzendorf, Alexander Conley, Neil Crighton, Kyle Barbary, Demitri Muna, Henry Ferguson, Frédéric Grollier, Madhura M. Parikh, Prasanth H. Nair, Hans M. Unther, Christoph Deil, Julien Woillez, Simon Conseil, Roban Kramer, James E. H. Turner, Leo Singer, Ryan Fox, Benjamin A. Weaver, Victor Zabalza, Zachary I. Edwards, K. Azalee Bostroem, D. J. Burke, Andrew R. Casey, Steven M. Crawford, Nadia Dencheva, Justin Ely, Tim Jenness, Kathleen Labrie, Pey Lian Lim, Francesco Pierfederici, Andrew Pontzen, Andy Ptak, Brian Refsdal, Mathieu Servillat, and Ole Streicher. Astropy: A community Python package for astronomy. *A&A*, 558: A33, October 2013. doi: 10.1051/0004-6361/201322068.

A. Avakyan, M. Neumann, A. Zainab, V. Doroshenko, J. Wilms, and A. Santangelo. XRBcats: Galactic Low Mass X-ray Binary Catalogue. *arXiv e-prints*, art. arXiv:2303.16168, March 2023. doi: 10.48550/arXiv.2303.16168.

M. Axelsson, L. Borgonovo, and S. Larsson. Evolution of the 0.01-25 Hz power spectral components in Cygnus X-1. *A&A*, 438:999–1012, August 2005. doi: 10.1051/0004-6361:20042362.

M. Axelsson, L. Borgonovo, and S. Larsson. Probing the temporal variability of Cygnus X-1 into the soft state. *A&A*, 452(3):975–984, June 2006. doi: 10.1051/0004-6361:20054397.

Magnus Axelsson and Chris Done. Breaking the spectral degeneracies in black hole binaries with fast timing data: the hard state of Cygnus X-1. *MNRAS*, 480 (1):751–758, October 2018. doi: 10.1093/mnras/sty1801.

Matteo Bachetti, Daniela Huppenkothen, Usman Khan, Himanshu Mishra, Abbie Stevens, Swapnil Sharma, John Swinbank, Amogh Desai, Haroon Rashid, Evandro Martinez Ribeiro, Mihir Tripathi, Brigitta Sipőcz, Dhruv Vats, tappina, Guglielmo Mastroserio, omargamal8, Meg Davis, Achilles Rasquinha, Paul Balm, Stuart Mumford, Devansh Shukla, Riccardo Campana, parkma99, Nitish Garg, Akash Tandon, Anurag Hota, Arnav Anand, Nick, Rashmi Raj, and Sashank Mishra. Stingraysoftware/stingray: Version 1.1.2, May 2023. URL `https://doi.org/10.5281/zenodo.7970570`.

Steven A. Balbus and John F. Hawley. A Powerful Local Shear Instability in Weakly Magnetized Disks. I. Linear Analysis. *ApJ*, 376:214, July 1991. doi: 10.1086/170270.

M. Bałucińska-Church, M. J. Church, P. A. Charles, F. Nagase, J. LaSala, and R. Barnard. The distribution of X-ray dips with orbital phase in Cygnus X-1. *MNRAS*, 311(4):861–868, February 2000. doi: 10.1046/j.1365-8711.2000.03149.x.

Rupal Basak, Andrzej A. Zdziarski, Michael Parker, and Nazma Islam. Analysis of NuSTAR and Suzaku observations of Cyg X-1 in the hard state: evidence for a truncated disc geometry. *MNRAS*, 472(4):4220–4232, December 2017. doi: 10.1093/mnras/stx2283.

Ehud Behar, Andrew P. Rasmussen, Alexander J. Blustin, Masao Sako, Steven M. Kahn, Jelle S. Kaastra, Graziella Branduardi-Raymont, and Katrien C. Steenbrugge. A Long Look at NGC 3783 with the XMM-Newton Reflection Grating Spectrometer. *ApJ*, 598(1):232–241, November 2003. doi: 10.1086/378853.

Krzysztof Belczynski, Tomasz Bulik, and Charles Bailyn. The Fate of Cyg X-1: An Empirical Lower Limit on Black-hole-Neutron-star Merger Rate. *ApJL*, 742 (1):L2, November 2011. doi: 10.1088/2041-8205/742/1/L2.

T. Belloni and G. Hasinger. Variability in the noise properties of Cygnus X-1. *A&A*, 227:L33–L36, January 1990.

T. Belloni, G. Hasinger, and P. Kahabka. The "noisy" pulsar in HER X-1. *A&A*, 245:L29, May 1991.

T. Belloni, J. Homan, P. Casella, M. van der Klis, E. Nespoli, W. H. G. Lewin, J. M. Miller, and M. Méndez. The evolution of the timing properties of the black-hole transient GX 339-4 during its 2002/2003 outburst. *A&A*, 440(1): 207–222, September 2005. doi: 10.1051/0004-6361:20042457.

T. M. Belloni. States and Transitions in Black Hole Binaries. In Tomaso Belloni, editor, *Lecture Notes in Physics, Berlin Springer Verlag*, volume 794, page 53. 2010a. doi: 10.1007/978-3-540-76937-8_3.

Tomaso Belloni. *The Jet Paradigm*, volume 794. 2010b. doi: 10.1007/978-3-540-76937-8.

Tomaso Belloni, Dimitrios Psaltis, and Michiel van der Klis. A Unified Description of the Timing Features of Accreting X-Ray Binaries. *ApJ*, 572(1):392–406, June 2002. doi: 10.1086/340290.

Tomaso M. Belloni and Dipankar Bhattacharya. Basics of Fourier Analysis for High-Energy Astronomy. In *Handbook of X-ray and Gamma-ray Astrophysics*, page 7. 2022. doi: 10.1007/978-981-16-4544-0_136-1.

Tomaso M. Belloni and Sara E. Motta. Transient Black Hole Binaries. In Cosimo Bambi, editor, *Astrophysics of Black Holes: From Fundamental Aspects to Latest Developments*, volume 440 of *Astrophysics and Space Science Library*, page 61, January 2016. doi: 10.1007/978-3-662-52859-4_2.

S. Benlloch, K. Pottschmidt, J. Wilms, M. A. Nowak, T. Gleissner, and G. G. Pooley. Different kinds of long-term variability from Cygnus X-1. In Philip Kaaret, Frederick K. Lamb, and Jean H. Swank, editors, *X-ray Timing 2003: Rossi and Beyond*, volume 714 of *American Institute of Physics Conference Series*, pages 61–64. AIP, July 2004. doi: 10.1063/1.1781001.

M. Berger and M. van der Klis. High time resolution observations of Cygnus X-3 with EXOSAT. *A&A*, 292:175–182, December 1994.

John M. Blondin. The Shadow Wind in High-Mass X-Ray Binaries. *ApJ*, 435:756, November 1994. doi: 10.1086/174853.

John M. Blondin and Jonathan W. Woo. Wind Dynamics in SMC X-1. I. Hydrodynamic Simulation. *ApJ*, 445:889, June 1995. doi: 10.1086/175748.

John M. Blondin, Ian R. Stevens, and Timothy R. Kallman. Enhanced Winds and Tidal Streams in Massive X-Ray Binaries. *ApJ*, 371:684, April 1991. doi: 10.1086/169934.

M. Böck, V. Grinberg, K. Pottschmidt, M. Hanke, M. A. Nowak, S. B. Markoff, P. Uttley, J. Rodriguez, G. G. Pooley, S. Suchy, R. E. Rothschild, and J. Wilms. Spectro-timing analysis of Cygnus X-1 during a fast state transition. *A&A*, 533: A8+, September 2011. doi: 10.1051/0004-6361/201117159.

D. A. Bollimpalli, R. Mahmoud, C. Done, P. C. Fragile, W. Kluźniak, R. Narayan, and C. J. White. Looking for the underlying cause of black hole X-ray variability in GRMHD simulations. *MNRAS*, 496(3):3808–3828, June 2020. doi: 10.1093/mnras/staa1808.

C. T. Bolton. Identification of Cygnus X-1 with HDE 226868. *Nature*, 235(5336): 271–273, February 1972. doi: 10.1038/235271b0.

C. T. Bolton. Orbital elements and an analysis of models for HDE 226868 = Cygnus X-1. *ApJ*, 200:269–277, September 1975. doi: 10.1086/153785.

H. Bondi and F. Hoyle. On the mechanism of accretion by stars. *MNRAS*, 104: 273, January 1944. doi: 10.1093/mnras/104.5.273.

S. Bowyer, E. T. Byram, T. A. Chubb, and H. Friedman. Cosmic X-ray Sources. *Science*, 147(3656):394–398, January 1965. doi: 10.1126/science.147.3656.394.

L. L. E. Braes and G. K. Miley. Physical Sciences: Detection of Radio Emission from Cygnus X-1. *Nature*, 232(5308):246, July 1971. doi: 10.1038/232246a0.

C. Brocksopp, R. P. Fender, V. Larionov, V. M. Lyuty, A. E. Tarasov, G. G. Pooley, W. S. Paciesas, and P. Roche. Orbital, precessional and flaring variability of Cygnus X-1. *MNRAS*, 309(4):1063–1073, November 1999. doi: 10.1046/j.1365-8711.1999.02919.x.

Tomasz Bulik, Krzysztof Belczynski, and Andrea Prestwich. IC10 X-1/NGC300 X-1: The Very Immediate Progenitors of BH-BH Binaries. *ApJ*, 730(2):140, April 2011. doi: 10.1088/0004-637X/730/2/140.

John K. Cannizzo, Wan Chen, and Mario Livio. The Accretion Disk Limit Cycle Instability in Black Hole X-Ray Binaries. *ApJ*, 454:880, December 1995. doi: 10.1086/176541.

P. Casella, T. Belloni, and L. Stella. The ABC of Low-Frequency Quasi-periodic Oscillations in Black Hole Candidates: Analogies with Z Sources. *ApJ*, 629(1): 403–407, August 2005. doi: 10.1086/431174.

J. I. Castor, D. C. Abbott, and R. I. Klein. Radiation-driven winds in Of stars. *ApJ*, 195:157–174, January 1975. doi: 10.1086/153315.

Yuri Cavecchi and Alessandro Patruno. The peculiar behaviour of burst oscillations in the accreting millisecond X-ray pulsar XTE J1814-338. *MNRAS*, 510(1):1431–1437, February 2022. doi: 10.1093/mnras/stab3536.

E. Churazov, M. Gilfanov, and M. Revnivtsev. Soft state of Cygnus X-1: stable disc and unstable corona. *MNRAS*, 321(4):759–766, March 2001. doi: 10.1046/j.1365-8711.2001.04056.x.

M. J. Coe, A. R. Engel, and J. J. Quenby. Anti-correlated hard and soft X-ray intensity variations of the black-hole candidates Cyg X-1 and A0620-00. *Nature*, 259(5544):544–546, February 1976. doi: 10.1038/259544a0.

J. M. Corral-Santana, J. Casares, T. Muñoz-Darias, F. E. Bauer, I. G. Martínez-Pais, and D. M. Russell. BlackCAT: A catalogue of stellar-mass black holes in X-ray transients. *A&A*, 587:A61, March 2016. doi: 10.1051/0004-6361/201527130.

L. R. Corrales, J. García, J. Wilms, and F. Baganoff. The dust-scattering component of X-ray extinction: effects on continuum fitting and high-resolution absorption edge structure. *MNRAS*, 458(2):1345–1351, May 2016. doi: 10.1093/mnras/stw376.

W. Cui, W. A. Heindl, R. E. Rothschild, S. N. Zhang, K. Jahoda, and W. Focke. Rossi X-Ray Timing Explorer Observation of Cygnus X-1 in Its High State. *ApJL*, 474(1):L57–L60, January 1997a. doi: 10.1086/310419.

Wei Cui, S. N. Zhang, W. Focke, and J. H. Swank. Temporal Properties of Cygnus X-1 during the Spectral Transitions. *ApJ*, 484(1):383–393, July 1997b. doi: 10.1086/304341.

T. Dauser, J. Garcia, M. L. Parker, A. C. Fabian, and J. Wilms. The role of the reflection fraction in constraining black hole spin. *MNRAS*, 444:L100–L104, October 2014. doi: 10.1093/mnrasl/slu125.

Shane W. Davis, Omer M. Blaes, Ivan Hubeny, and Neal J. Turner. Relativistic Accretion Disk Models of High-State Black Hole X-Ray Binary Spectra. *ApJ*, 621(1):372–387, March 2005. doi: 10.1086/427278.

B. De Marco, G. Ponti, T. Muñoz-Darias, and K. Nandra. Tracing the Reverberation Lag in the Hard State of Black Hole X-Ray Binaries. *ApJ*, 814(1):50, November 2015a. doi: 10.1088/0004-637X/814/1/50.

B. De Marco, G. Ponti, T. Muñoz-Darias, and K. Nandra. The evolution of the disc variability along the hard state of the black hole transient GX 339-4. *MNRAS*, 454(3):2360–2371, December 2015b. doi: 10.1093/mnras/stv1990.

B. De Marco, G. Ponti, P. O. Petrucci, M. Clavel, S. Corbel, R. Belmont, S. Chakravorty, M. Coriat, S. Drappeau, J. Ferreira, G. Henri, J. Malzac, J. Rodriguez, J. A. Tomsick, F. Ursini, and A. A. Zdziarski. Evolution of the reverberation lag in GX 339-4 at the end of an outburst. *MNRAS*, 471 (2):1475–1487, October 2017. doi: 10.1093/mnras/stx1649.

B. De Marco, T. P. Adhikari, G. Ponti, S. Bianchi, G. A. Kriss, N. Arav, E. Behar, G. Brand uardi-Raymont, M. Cappi, E. Costantini, D. Costanzo, L. di Gesu, J. Ebrero, J. S. Kaastra, S. Kaspi, J. Mao, A. Markowitz, G. Matt, M. Mehdipour, R. Middei, S. Paltani, P. O. Petrucci, C. Pinto, A. Różańska, and D. J. Walton. Incoherent fast variability of X-ray obscurers. The case of NGC 3783. *A&A*, 634:A65, February 2020. doi: 10.1051/0004-6361/201936470.

B. De Marco, A. A. Zdziarski, G. Ponti, G. Migliori, T. M. Belloni, A. Segovia Otero, M. A. Dziełak, and E. V. Lai. The inner flow geometry in MAXI J1820+070 during hard and hard-intermediate states. *A&A*, 654:A14, October 2021. doi: 10.1051/0004-6361/202140567.

T. Di Salvo, C. Done, P. T. Życki, L. Burderi, and N. R. Robba. Probing the Inner Region of Cygnus X-1 in the Low/Hard State through Its X-Ray Broadband Spectrum. *ApJ*, 547(2):1024–1033, February 2001. doi: 10.1086/318396.

C. M. Diez, V. Grinberg, F. Fürst, I. El Mellah, M. Zhou, A. Santangelo, S. Martínez-Núñez, R. Amato, N. Hell, and P. Kretschmar. Observing the onset of the accretion wake in Vela X-1. *A&A*, 674:A147, June 2023. doi: 10.1051/0004-6361/202245708.

Chris Done, Marek Gierliński, and Aya Kubota. Modelling the behaviour of accretion flows in X-ray binaries. Everything you always wanted to know about accretion but were afraid to ask. *A&ARv*, 15(1):1–66, December 2007. doi: 10.1007/s00159-007-0006-1.

J. B. Dove, Jörn Wilms, M. A. Nowak, B. A. Vaughan, and M. C. Begelman. RXTE observation of Cygnus X-1: spectral analysis. *Nuclear Physics B Proceedings Supplements*, 69(1-3):308–311, January 1999. doi: 10.1016/S0920-5632(98)00230-8.

R. J. H. Dunn, R. P. Fender, E. G. Körding, T. Belloni, and C. Cabanac. A global spectral study of black hole X-ray binaries. *MNRAS*, 403(1):61–82, March 2010. doi: 10.1111/j.1365-2966.2010.16114.x.

A. Einstein. Die Grundlage der allgemeinen Relativitätstheorie. *Annalen der Physik*, 354(7):769–822, January 1916. doi: 10.1002/andp.19163540702.

I. El Mellah, J. O. Sundqvist, and R. Keppens. Accretion from a clumpy massive-star wind in supergiant X-ray binaries. *MNRAS*, 475(3):3240–3252, April 2018. doi: 10.1093/mnras/stx3211.

I. El Mellah, V. Grinberg, J. O. Sundqvist, F. A. Driessen, and M. A. Leutenegger. Radiography in high mass X-ray binaries. Micro-structure of the stellar wind through variability of the column density. *A&A*, 643:A9, November 2020. doi: 10.1051/0004-6361/202038791.

M. Elvis, C. G. Page, K. A. Pounds, M. J. Ricketts, and M. J. L. Turner. Discovery of powerful transient X-ray source A0620-00 with Ariel V Sky Survey Experiment. *Nature*, 257(5528):656–657, October 1975. doi: 10.1038/257656a0.

Martin Elvis, Belinda J. Wilkes, Jonathan C. McDowell, Richard F. Green, Jill Bechtold, S. P. Willner, M. S. Oey, Elisha Polomski, and Roc Cutri. Atlas of Quasar Energy Distributions. *ApJSupp*, 95:1, November 1994. doi: 10.1086/192093.

Event Horizon Telescope Collaboration, Kazunori Akiyama, Antxon Alberdi, Walter Alef, Keiichi Asada, Rebecca Azulay, Anne-Kathrin Baczko, David Ball, Mislav Baloković, John Barrett, Dan Bintley, Lindy Blackburn, Wilfred Boland, Katherine L. Bouman, Geoffrey C. Bower, Michael Bremer, Christiaan D. Brinkerink, Roger Brissenden, Silke Britzen, Avery E. Broderick, Dominique Broguiere, Thomas Bronzwaer, Do-Young Byun, John E. Carlstrom, Andrew Chael, Chi-kwan Chan, Shami Chatterjee, Koushik Chatterjee, Ming-Tang Chen, Yongjun Chen, Ilje Cho, Pierre Christian, John E. Conway, James M. Cordes, Geoffrey B. Crew, Yuzhu Cui, Jordy Davelaar, Mariafelicia De Laurentis, Roger Deane, Jessica Dempsey, Gregory Desvignes, Jason Dexter, Sheperd S. Doeleman, Ralph P. Eatough, Heino Falcke, Vincent L. Fish, Ed Fomalont, Raquel Fraga-Encinas, William T. Freeman, Per Friberg, Christian M. Fromm, José L. Gómez, Peter Galison, Charles F. Gammie, Roberto García, Olivier Gentaz, Boris Georgiev, Ciriaco Goddi, Roman Gold, Minfeng Gu, Mark Gurwell, Kazuhiro Hada, Michael H. Hecht, Ronald Hesper, Luis C. Ho, Paul Ho, Mareki Honma, Chih-Wei L. Huang, Lei Huang, David H. Hughes, Shiro Ikeda, Makoto Inoue, Sara Issaoun, David J. James, Buell T. Jannuzi, Michael Janssen, Britton Jeter, Wu Jiang, Michael D. Johnson, Svetlana Jorstad, Taehyun Jung, Mansour Karami, Ramesh Karuppusamy, Tomohisa Kawashima, Garrett K. Keating, Mark Kettenis, Jae-Young Kim, Junhan Kim, Jongsoo Kim, Motoki Kino, Jun Yi Koay, Patrick M. Koch, Shoko Koyama, Michael Kramer, Carsten Kramer, Thomas P. Krichbaum, Cheng-Yu Kuo,

Tod R. Lauer, Sang-Sung Lee, Yan-Rong Li, Zhiyuan Li, Michael Lindqvist, Kuo Liu, Elisabetta Liuzzo, Wen-Ping Lo, Andrei P. Lobanov, Laurent Loinard, Colin Lonsdale, Ru-Sen Lu, Nicholas R. MacDonald, Jirong Mao, Sera Markoff, Daniel P. Marrone, Alan P. Marscher, Iván Martí-Vidal, Satoki Matsushita, Lynn D. Matthews, Lia Medeiros, Karl M. Menten, Yosuke Mizuno, Izumi Mizuno, James M. Moran, Kotaro Moriyama, Monika Moscibrodzka, Cornelia Müller, Hiroshi Nagai, Neil M. Nagar, Masanori Nakamura, Ramesh Narayan, Gopal Narayanan, Iniyan Natarajan, Roberto Neri, Chunchong Ni, Aristeidis Noutsos, Hiroki Okino, Héctor Olivares, Gisela N. Ortiz-León, Tomoaki Oyama, Feryal Özel, Daniel C. M. Palumbo, Nimesh Patel, Ue-Li Pen, Dominic W. Pesce, Vincent Piétu, Richard Plambeck, Aleksandar PopStefanija, Oliver Porth, Ben Prather, Jorge A. Preciado-López, Dimitrios Psaltis, Hung-Yi Pu, Venkatessh Ramakrishnan, Ramprasad Rao, Mark G. Rawlings, Alexander W. Raymond, Luciano Rezzolla, Bart Ripperda, Freek Roelofs, Alan Rogers, Eduardo Ros, Mel Rose, Arash Roshanineshat, Helge Rottmann, Alan L. Roy, Chet Ruszczyk, Benjamin R. Ryan, Kazi L. J. Rygl, Salvador Sánchez, David Sánchez-Arguelles, Mahito Sasada, Tuomas Savolainen, F. Peter Schloerb, Karl-Friedrich Schuster, Lijing Shao, Zhiqiang Shen, Des Small, Bong Won Sohn, Jason SooHoo, Fumie Tazaki, Paul Tiede, Remo P. J. Tilanus, Michael Titus, Kenji Toma, Pablo Torne, Tyler Trent, Sascha Trippe, Shuichiro Tsuda, Ilse van Bemmel, Huib Jan van Langevelde, Daniel R. van Rossum, Jan Wagner, John Wardle, Jonathan Weintroub, Norbert Wex, Robert Wharton, Maciek Wielgus, George N. Wong, Qingwen Wu, Ken Young, André Young, Ziri Younsi, Feng Yuan, Ye-Fei Yuan, J. Anton Zensus, Guangyao Zhao, Shan-Shan Zhao, Ziyan Zhu, Juan-Carlos Algaba, Alexander Allardi, Rodrigo Amestica, Jadyn Anczarski, Uwe Bach, Frederick K. Baganoff, Christopher Beaudoin, Bradford A. Benson, Ryan Berthold, Jay M. Blanchard, Ray Blundell, Sandra Bustamente, Roger Cappallo, Edgar Castillo-Domínguez, Chih-Cheng Chang, Shu-Hao Chang, Song-Chu Chang, Chung-Chen Chen, Ryan Chilson, Tim C. Chuter, Rodrigo Córdova Rosado, Iain M. Coulson, Thomas M. Crawford, Joseph Crowley, John David, Mark Derome, Matthew Dexter, Sven Dornbusch, Kevin A. Dudevoir, Sergio A. Dzib, Andreas Eckart, Chris Eckert, Neal R. Erickson, Wendeline B. Everett, Aaron Faber, Joseph R. Farah, Vernon Fath, Thomas W. Folkers, David C. Forbes, Robert Freund, Arturo I. Gómez-Ruiz, David M. Gale, Feng Gao, Gertie Geertsema, David A. Graham, Christopher H. Greer, Ronald Grosslein, Frédéric Gueth, Daryl Haggard, Nils W. Halverson, Chih-Chiang Han, Kuo-Chang Han, Jinchi Hao, Yutaka Hasegawa, Jason W. Henning, Antonio Hernández-Gómez, Rubén Herrero-Illana, Stefan Heyminck, Akihiko Hirota, James Hoge, Yau-De Huang, C. M. Violette Impellizzeri, Homin Jiang, Atish Kamble, Ryan Keisler, Kimihiro Kimura, Yusuke Kono, Derek Kubo, John Kuroda, Richard Lacasse,

Robert A. Laing, Erik M. Leitch, Chao-Te Li, Lupin C. C. Lin, Ching-Tang Liu, Kuan-Yu Liu, Li-Ming Lu, Ralph G. Marson, Pierre L. Martin-Cocher, Kyle D. Massingill, Callie Matulonis, Martin P. McColl, Stephen R. McWhirter, Hugo Messias, Zheng Meyer-Zhao, Daniel Michalik, Alfredo Montaña, William Montgomerie, Matias Mora-Klein, Dirk Muders, Andrew Nadolski, Santiago Navarro, Joseph Neilsen, Chi H. Nguyen, Hiroaki Nishioka, Timothy Norton, Michael A. Nowak, George Nystrom, Hideo Ogawa, Peter Oshiro, Tomoaki Oyama, Harriet Parsons, Scott N. Paine, Juan Peñalver, Neil M. Phillips, Michael Poirier, Nicolas Pradel, Rurik A. Primiani, Philippe A. Raffin, Alexandra S. Rahlin, George Reiland, Christopher Risacher, Ignacio Ruiz, Alejandro F. Sáez-Madaín, Remi Sassella, Pim Schellart, Paul Shaw, Kevin M. Silva, Hotaka Shiokawa, David R. Smith, William Snow, Kamal Souccar, Don Sousa, T. K. Sridharan, Ranjani Srinivasan, William Stahm, Anthony A. Stark, Kyle Story, Sjoerd T. Timmer, Laura Vertatschitsch, Craig Walther, Ta-Shun Wei, Nathan Whitehorn, Alan R. Whitney, David P. Woody, Jan G. A. Wouterloot, Melvin Wright, Paul Yamaguchi, Chen-Yu Yu, Milagros Zeballos, Shuo Zhang, and Lucy Ziurys. First M87 Event Horizon Telescope Results. I. The Shadow of the Supermassive Black Hole. *ApJL*, 875(1):L1, April 2019. doi: 10.3847/2041-8213/ab0ec7.

Event Horizon Telescope Collaboration, Kazunori Akiyama, Antxon Alberdi, Walter Alef, Juan Carlos Algaba, Richard Anantua, Keiichi Asada, Rebecca Azulay, Uwe Bach, Anne-Kathrin Baczko, David Ball, Mislav Baloković, John Barrett, Michi Bauböck, Bradford A. Benson, Dan Bintley, Lindy Blackburn, Raymond Blundell, Katherine L. Bouman, Geoffrey C. Bower, Hope Boyce, Michael Bremer, Christiaan D. Brinkerink, Roger Brissenden, Silke Britzen, Avery E. Broderick, Dominique Broguiere, Thomas Bronzwaer, Sandra Bustamante, Do-Young Byun, John E. Carlstrom, Chiara Ceccobello, Andrew Chael, Chi-kwan Chan, Koushik Chatterjee, Shami Chatterjee, Ming-Tang Chen, Yongjun Chen, Xiaopeng Cheng, Ilje Cho, Pierre Christian, Nicholas S. Conroy, John E. Conway, James M. Cordes, Thomas M. Crawford, Geoffrey B. Crew, Alejandro Cruz-Osorio, Yuzhu Cui, Jordy Davelaar, Mariafelicia De Laurentis, Roger Deane, Jessica Dempsey, Gregory Desvignes, Jason Dexter, Vedant Dhruv, Sheperd S. Doeleman, Sean Dougal, Sergio A. Dzib, Ralph P. Eatough, Razieh Emami, Heino Falcke, Joseph Farah, Vincent L. Fish, Ed Fomalont, H. Alyson Ford, Raquel Fraga-Encinas, William T. Freeman, Per Friberg, Christian M. Fromm, Antonio Fuentes, Peter Galison, Charles F. Gammie, Roberto García, Olivier Gentaz, Boris Georgiev, Ciriaco Goddi, Roman Gold, Arturo I. Gómez-Ruiz, José L. Gómez, Minfeng Gu, Mark Gurwell, Kazuhiro Hada, Daryl Haggard, Kari Haworth, Michael H. Hecht, Ronald Hesper, Dirk Heumann, Luis C. Ho, Paul Ho, Mareki Honma, Chih-Wei L. Huang, Lei Huang, David H. Hughes, Shiro Ikeda, C. M. Violette Impellizzeri, Makoto Inoue, Sara Issaoun, David J.

James, Buell T. Jannuzi, Michael Janssen, Britton Jeter, Wu Jiang, Alejandra Jiménez-Rosales, Michael D. Johnson, Svetlana Jorstad, Abhishek V. Joshi, Taehyun Jung, Mansour Karami, Ramesh Karuppusamy, Tomohisa Kawashima, Garrett K. Keating, Mark Kettenis, Dong-Jin Kim, Jae-Young Kim, Jongsoo Kim, Junhan Kim, Motoki Kino, Jun Yi Koay, Prashant Kocherlakota, Yutaro Kofuji, Patrick M. Koch, Shoko Koyama, Carsten Kramer, Michael Kramer, Thomas P. Krichbaum, Cheng-Yu Kuo, Noemi La Bella, Tod R. Lauer, Daeyoung Lee, Sang-Sung Lee, Po Kin Leung, Aviad Levis, Zhiyuan Li, Rocco Lico, Greg Lindahl, Michael Lindqvist, Mikhail Lisakov, Jun Liu, Kuo Liu, Elisabetta Liuzzo, Wen-Ping Lo, Andrei P. Lobanov, Laurent Loinard, Colin J. Lonsdale, Ru-Sen Lu, Jirong Mao, Nicola Marchili, Sera Markoff, Daniel P. Marrone, Alan P. Marscher, Iván Martí-Vidal, Satoki Matsushita, Lynn D. Matthews, Lia Medeiros, Karl M. Menten, Daniel Michalik, Izumi Mizuno, Yosuke Mizuno, James M. Moran, Kotaro Moriyama, Monika Moscibrodzka, Cornelia Müller, Alejandro Mus, Gibwa Musoke, Ioannis Myserlis, Andrew Nadolski, Hiroshi Nagai, Neil M. Nagar, Masanori Nakamura, Ramesh Narayan, Gopal Narayanan, Iniyan Natarajan, Antonios Nathanail, Santiago Navarro Fuentes, Joey Neilsen, Roberto Neri, Chunchong Ni, Aristeidis Noutsos, Michael A. Nowak, Junghwan Oh, Hiroki Okino, Héctor Olivares, Gisela N. Ortiz-León, Tomoaki Oyama, Feryal Özel, Daniel C. M. Palumbo, Georgios Filippos Paraschos, Jongho Park, Harriet Parsons, Nimesh Patel, Ue-Li Pen, Dominic W. Pesce, Vincent Piétu, Richard Plambeck, Aleksandar PopStefanija, Oliver Porth, Felix M. Pötzl, Ben Prather, Jorge A. Preciado-López, Dimitrios Psaltis, Hung-Yi Pu, Venkatessh Ramakrishnan, Ramprasad Rao, Mark G. Rawlings, Alexander W. Raymond, Luciano Rezzolla, Angelo Ricarte, Bart Ripperda, Freek Roelofs, Alan Rogers, Eduardo Ros, Cristina Romero-Cañizales, Arash Roshanineshat, Helge Rottmann, Alan L. Roy, Ignacio Ruiz, Chet Ruszczyk, Kazi L. J. Rygl, Salvador Sánchez, David Sánchez-Argüelles, Miguel Sánchez-Portal, Mahito Sasada, Kaushik Satapathy, Tuomas Savolainen, F. Peter Schloerb, Jonathan Schonfeld, Karl-Friedrich Schuster, Lijing Shao, Zhiqiang Shen, Des Small, Bong Won Sohn, Jason SooHoo, Kamal Souccar, He Sun, Fumie Tazaki, Alexandra J. Tetarenko, Paul Tiede, Remo P. J. Tilanus, Michael Titus, Pablo Torne, Efthalia Traianou, Tyler Trent, Sascha Trippe, Matthew Turk, Ilse van Bemmel, Huib Jan van Langevelde, Daniel R. van Rossum, Jesse Vos, Jan Wagner, Derek Ward-Thompson, John Wardle, Jonathan Weintroub, Norbert Wex, Robert Wharton, Maciek Wielgus, Kaj Wiik, Gunther Witzel, Michael F. Wondrak, George N. Wong, Qingwen Wu, Paul Yamaguchi, Doosoo Yoon, André Young, Ken Young, Ziri Younsi, Feng Yuan, Ye-Fei Yuan, J. Anton Zensus, Shuo Zhang, Guang-Yao Zhao, and Shan-Shan Zhao. First Sagittarius A* Event Horizon Telescope Results. VI. Testing the Black Hole Metric. *ApJL*, 930(2):

L17, May 2022. doi: 10.3847/2041-8213/ac6756.

Andrew C. Fabian and Giovanni Miniutti. The X-ray spectra of accreting Kerr black holes. *arXiv e-prints*, art. astro-ph/0507409, July 2005. doi: 10.48550/arXiv.astro-ph/0507409.

A. Feldmeier, J. Puls, and A. W. A. Pauldrach. A possible origin for X-rays from O stars. *A&A*, 322:878–895, June 1997.

Francesca M. Fornasini, John A. Tomsick, Matteo Bachetti, Roman A. Krivonos, Felix Fürst, Lorenzo Natalucci, Katja Pottschmidt, and Jörn Wilms. An XMM-Newton and NuSTAR Study of IGR J18214-1318: A Non-pulsating High-mass X-Ray Binary with a Neutron Star. *ApJ*, 841(1):35, May 2017. doi: 10.3847/1538-4357/aa6ff4.

Juhan Frank, Andrew King, and Derek J. Raine. *Accretion Power in Astrophysics: Third Edition*. 2002.

D. B. Friend and J. I. Castor. Radiation driven winds in X-ray binaries. *ApJ*, 261: 293–300, October 1982. doi: 10.1086/160340.

F. Frontera, E. Palazzi, A. A. Zdziarski, F. Haardt, G. C. Perola, L. Chiappetti, G. Cusumano, D. Dal Fiume, S. Del Sordo, M. Orlandini, A. N. Parmar, L. Piro, A. Santangelo, A. Segreto, A. Treves, and M. Trifoglio. Broadband Spectrum of Cygnus X-1 in Two Spectral States with BeppoSAX. *ApJ*, 546(2):1027–1037, January 2001a. doi: 10.1086/318304.

F. Frontera, A. A. Zdziarski, L. Amati, J. Mikołajewska, T. Belloni, S. Del Sordo, F. Haardt, E. Kuulkers, N. Masetti, M. Orlandini, E. Palazzi, A. N. Parmar, R. A. Remillard, A. Santangelo, and L. Stella. A Measurement of the Broadband Spectrum of XTE J1118+480 with BeppoSAX and Its Astrophysical Implications. *ApJ*, 561(2):1006–1015, November 2001b. doi: 10.1086/323258.

Felix Fürst, Katja Pottschmidt, Jörn Wilms, John A. Tomsick, Matteo Bachetti, Steven E. Boggs, Finn E. Christensen, William W. Craig, Brian W. Grefenstette, Charles J. Hailey, Fiona Harrison, Kristin K. Madsen, Jon M. Miller, Daniel Stern, Dominic J. Walton, and William Zhang. NuSTAR Discovery of a Luminosity Dependent Cyclotron Line Energy in Vela X-1. *ApJ*, 780(2):133, January 2014. doi: 10.1088/0004-637X/780/2/133.

Javier A. García, James F. Steiner, Jeffrey E. McClintock, Ronald A. Remillard, Victoria Grinberg, and Thomas Dauser. X-Ray Reflection Spectroscopy of the Black Hole GX 339–4: Exploring the Hard State with Unprecedented Sensitivity. *ApJ*, 813(2):84, November 2015. doi: 10.1088/0004-637X/813/2/84.

Javier A. García, Andrew C. Fabian, Timothy R. Kallman, Thomas Dauser, Michael L. Parker, Jeffrey E. McClintock, James F. Steiner, and Jörn Wilms. The effects of high density on the X-ray spectrum reflected from accretion discs around black holes. *MNRAS*, 462(1):751–760, October 2016. doi: 10.1093/mnras/stw1696.

Marek Gierliński and Chris Done. Black hole accretion discs: reality confronts theory. *MNRAS*, 347(3):885–894, January 2004. doi: 10.1111/j.1365-2966.2004.07266.x.

Marek Gierlinski, Andrzej A. Zdziarski, Chris Done, W. Neil Johnson, Ken Ebisawa, Yoshihiro Ueda, Francesco Haardt, and Bernard F. Phlips. Simultaneous X-ray and gamma-ray observations of CYG X-1 in the hard state by GINGA and OSSE. *MNRAS*, 288(4):958–964, July 1997. doi: 10.1093/mnras/288.4.958.

Marek Gierliński, Andrzej A. Zdziarski, Juri Poutanen, Paolo S. Coppi, Ken Ebisawa, and W. Neil Johnson. Radiation mechanisms and geometry of Cygnus X-1 in the soft state. *MNRAS*, 309(2):496–512, October 1999. doi: 10.1046/j.1365-8711.1999.02875.x.

D. R. Gies and C. T. Bolton. The Optical Spectrum of HDE 226868 = Cygnus X-1. III. A Focused Stellar Wind Model for He II lambda 4686 Emission. *ApJ*, 304:389, May 1986. doi: 10.1086/164172.

D. R. Gies, C. T. Bolton, J. R. Thomson, W. Huang, M. V. McSwain, R. L. Riddle, Z. Wang, P. J. Wiita, D. W. Wingert, B. Csák, and L. L. Kiss. Wind Accretion and State Transitions in Cygnus X-1. *ApJ*, 583(1):424–436, January 2003. doi: 10.1086/345345.

D. R. Gies, C. T. Bolton, R. M. Blake, S. M. Caballero-Nieves, D. M. Crenshaw, P. Hadrava, A. Herrero, T. C. Hillwig, S. B. Howell, W. Huang, L. Kaper, P. Koubský, and M. V. McSwain. Stellar Wind Variations during the X-Ray High and Low States of Cygnus X-1. *ApJ*, 678(2):1237–1247, May 2008. doi: 10.1086/586690.

M. Gilfanov. X-Ray Emission from Black-Hole Binaries. In Tomaso Belloni, editor, *Lecture Notes in Physics, Berlin Springer Verlag*, volume 794, page 17. 2010. doi: 10.1007/978-3-540-76937-8_2.

V. Grinberg, N. Hell, K. Pottschmidt, M. Böck, M. A. Nowak, J. Rodriguez, A. Bodaghee, M. Cadolle Bel, G. L. Case, M. Hanke, M. Kühnel, S. B. Markoff, G. G. Pooley, R. E. Rothschild, J. A. Tomsick, C. A. Wilson-Hodge, and J. Wilms. Long term variability of Cygnus X-1. V. State definitions with all sky monitors. *A&A*, 554:A88, June 2013. doi: 10.1051/0004-6361/201321128.

V. Grinberg, K. Pottschmidt, M. Böck, C. Schmid, M. A. Nowak, P. Uttley, J. A. Tomsick, J. Rodriguez, N. Hell, A. Markowitz, A. Bodaghee, M. Cadolle Bel, R. E. Rothschild, and J. Wilms. Long term variability of Cygnus X-1. VI. Energy-resolved X-ray variability 1999-2011. *A&A*, 565:A1, May 2014. doi: 10.1051/0004-6361/201322969.

V. Grinberg, M. A. Leutenegger, N. Hell, K. Pottschmidt, M. Böck, J. A. García, M. Hanke, M. A. Nowak, J. O. Sundqvist, R. H. D. Townsend, and J. Wilms. Long term variability of Cygnus X-1. VII. Orbital variability of the focussed wind in Cyg X-1/HDE 226868 system. *A&A*, 576:A117, April 2015. doi: 10.1051/0004-6361/201425418.

V. Grinberg, P. Uttley, J. Wilms, J. Miller-Jones, K. Pottschmidt, S. Niu, M. Hirsch, and Chocbox Collaboration. Opening the CHOCBOX: clumpy stellar winds in Cyg X-1. In Jan-Uwe Ness and Simone Migliari, editors, *The X-ray Universe 2017*, page 90, October 2017.

V. Grinberg, M. A. Nowak, and N. Hell. Color-color diagrams as tools for assessment of the variable absorption in high mass X-ray binaries. *A&A*, 643:A109, November 2020. doi: 10.1051/0004-6361/202039183.

J. E. Grove, W. N. Johnson, R. A. Kroeger, K. McNaron-Brown, J. G. Skibo, and B. F. Phlips. Gamma-Ray Spectral States of Galactic Black Hole Candidates. *ApJ*, 500(2):899–908, June 1998. doi: 10.1086/305746.

M. Hanke, J. Wilms, M. A. Nowak, N. S. Schulz, K. Pottschmidt, J. Lee, and M. Boeck. Multi-Satellite Observations of Cygnus X-1. In *Microquasars and Beyond*, page 29, January 2008. doi: 10.22323/1.062.0029.

Manfred Hanke, Jörn Wilms, Michael A. Nowak, Katja Pottschmidt, Norbert S. Schulz, and Julia C. Lee. Chandra X-Ray Spectroscopy of the Focused Wind in the Cygnus X-1 System. I. The Nondip Spectrum in the Low/Hard State. *ApJ*, 690(1):330–346, January 2009. doi: 10.1088/0004-637X/690/1/330.

L. K. Härer, M. L. Parker, I. El Mellah, V. Grinberg, R. Ballhausen, Z. Igo, A. Joyce, and J. Wilms. Stellar-wind variability in Cygnus X-1 from high-resolution excess variance spectroscopy with Chandra. *A&A*, 680:A72, December 2023. doi: 10.1051/0004-6361/202346669.

G. Hasinger and M. van der Klis. Two patterns of correlated X-ray timing and spectral behaviour in low-mass X-ray binaries. *A&A*, 225:79–96, November 1989.

L. M. Heil, S. Vaughan, and P. Uttley. The ubiquity of the rms-flux relation in black hole X-ray binaries. *MNRAS*, 422(3):2620–2631, May 2012. doi: 10.1111/j.1365-2966.2012.20824.x.

L. M. Heil, P. Uttley, and M. Klein-Wolt. Power colours: simple X-ray binary variability comparison. *MNRAS*, 448(4):3339–3347, April 2015. doi: 10.1093/mnras/stv191.

A. Herrero, R. P. Kudritzki, R. Gabler, J. M. Vilchez, and A. Gabler. Fundamental parameters of galactic luminous OB stars. II. A spectroscopic analysis of HDE 226868 and the mass of Cygnus X-1. *A&A*, 297:556, May 1995.

HI4PI Collaboration, N. Ben Bekhti, L. Flöer, R. Keller, J. Kerp, D. Lenz, B. Winkel, J. Bailin, M. R. Calabretta, L. Dedes, H. A. Ford, B. K. Gibson, U. Haud, S. Janowiecki, P. M. W. Kalberla, F. J. Lockman, N. M. McClure-Griffiths, T. Murphy, H. Nakanishi, D. J. Pisano, and L. Staveley-Smith. HI4PI: A full-sky H I survey based on EBHIS and GASS. *A&A*, 594:A116, October 2016. doi: 10.1051/0004-6361/201629178.

Peter D. Hill. Kernel estimation of a distribution function. 14(3):605–620, 1985. ISSN 0361-0926 (print), 1532-415X (electronic). doi: https://doi.org/10.1080/03610928508828937.

Maria Hirsch, Natalie Hell, Victoria Grinberg, Ralf Ballhausen, Michael A. Nowak, Katja Pottschmidt, Norbert S. Schulz, Thomas Dauser, Manfred Hanke, Timothy R. Kallman, Gregory V. Brown, and Jörn Wilms. Chandra X-ray spectroscopy of the focused wind in the Cygnus X-1 system. III. Dipping in the low/hard state. *A&A*, 626:A64, June 2019. doi: 10.1051/0004-6361/201935074.

R. M. Hjellming and C. M. Wade. Radio Spectrum of Cygnus X-1. *Nature*, 234 (5325):138, November 1971. doi: 10.1038/234138a0.

Jeroen Homan and Tomaso Belloni. The Evolution of Black Hole States. *Ap&SS*, 300(1-3):107–117, November 2005. doi: 10.1007/s10509-005-1197-4.

Jeroen Homan, Joe Bright, Sara E. Motta, Diego Altamirano, Zaven Arzoumanian, Arkadip Basak, Tomaso M. Belloni, Edward M. Cackett, Rob Fender, Keith C. Gendreau, Erin Kara, Dheeraj R. Pasham, Ronald A. Remillard, James F. Steiner, Abigail L. Stevens, and Phil Uttley. A Rapid Change in X-Ray Variability and a Jet Ejection in the Black Hole Transient MAXI J1820+070. *ApJL*, 891(2):L29, March 2020. doi: 10.3847/2041-8213/ab7932.

J. C. Houck. ISIS: The Interactive Spectral Interpretation System. In G. Branduardi-Raymont, editor, *High Resolution X-ray Spectroscopy with XMM-Newton and Chandra*, page 17, December 2002.

J. C. Houck and L. A. Denicola. ISIS: An Interactive Spectral Interpretation System for High Resolution X-Ray Spectroscopy. In Nadine Manset, Christian Veillet, and Dennis Crabtree, editors, *Astronomical Data Analysis Software and Systems IX*, volume 216 of *Astronomical Society of the Pacific Conference Series*, page 591, January 2000.

F. Hoyle and R. A. Lyttleton. The effect of interstellar matter on climatic variation. *Proceedings of the Cambridge Philosophical Society*, 35(3):405, January 1939. doi: 10.1017/S0305004100021150.

John D. Hunter. Matplotlib: A 2d graphics environment. *Computing in Science Engineering*, 9(3):90–95, 2007. doi: 10.1109/MCSE.2007.55.

Daniela Huppenkothen, Matteo Bachetti, Abigail Stevens, Simone Migliari, Paul Balm, Omar Hammad, Usman Mahmood Khan, Himanshu Mishra, Haroon Rashid, Swapnil Sharma, Evandro Martinez Ribeiro, and Ricardo Valles Blanco. stingray: A modern python library for spectral timing. *Journal of Open Source Software*, 4(38):1393, 2019. doi: 10.21105/joss.01393. URL `https://doi.org/10.21105/joss.01393`.

Daniela Huppenkothen, Matteo Bachetti, Abigail L. Stevens, Simone Migliari, Paul Balm, Omar Hammad, Usman Mahmood Khan, Himanshu Mishra, Haroon Rashid, Swapnil Sharma, Evandro Martinez Ribeiro, and Ricardo Valles Blanco. Stingray: A Modern Python Library for Spectral Timing. *ApJ*, 881(1): 39, August 2019. doi: 10.3847/1538-4357/ab258d.

Adam Ingram. Error formulae for the energy-dependent cross-spectrum. *MNRAS*, 489(3):3927–3938, November 2019. doi: 10.1093/mnras/stz2409.

Adam Ingram and Michiel van der Klis. An exact analytic treatment of propagating mass accretion rate fluctuations in X-ray binaries. *MNRAS*, 434(2):1476–1485, September 2013. doi: 10.1093/mnras/stt1107.

Adam R. Ingram and Sara E. Motta. A review of quasi-periodic oscillations from black hole X-ray binaries: Observation and theory. *New Astron. Rev.*, 85:101524, September 2019. doi: 10.1016/j.newar.2020.101524.

Chichuan Jin, Gabriele Ponti, Frank Haberl, and Randall Smith. Probing the interstellar dust towards the Galactic Centre: dust-scattering halo around AX

J1745.6-2901. *MNRAS*, 468(3):2532–2551, July 2017. doi: 10.1093/mnras/stx653.

Chichuan Jin, Gabriele Ponti, Frank Haberl, Randall Smith, and Lynne Valencic. Effects of interstellar dust scattering on the X-ray eclipses of the LMXB AX J1745.6-2901 in the Galactic Centre. *MNRAS*, 477(3):3480–3506, July 2018. doi: 10.1093/mnras/sty869.

A. Joinet, E. Kalemci, and F. Senziani. Hard X-Ray Emission of the Microquasar GRO J1655-40 during the Rise of Its 2005 Outburst. *ApJ*, 679(1):655–663, May 2008. doi: 10.1086/533512.

A. Juráňová, E. Costantini, and P. Uttley. Spectral-timing of AGN ionized outflows with Athena. *MNRAS*, 510(3):4225–4235, March 2022. doi: 10.1093/mnras/stab3731.

J. S. Kaastra, R. G. Detmers, M. Mehdipour, N. Arav, E. Behar, S. Bianchi, G. Branduardi-Raymont, M. Cappi, E. Costantini, J. Ebrero, G. A. Kriss, S. Paltani, P. O. Petrucci, C. Pinto, G. Ponti, K. C. Steenbrugge, and C. P. de Vries. Multiwavelength campaign on Mrk 509. VIII. Location of the X-ray absorber. *A&A*, 539:A117, March 2012. doi: 10.1051/0004-6361/201118161.

T. R. Kallman, M. A. Bautista, Stephane Goriely, Claudio Mendoza, Jon M. Miller, Patrick Palmeri, Pascal Quinet, and John Raymond. Spectrum Synthesis Modeling of the X-Ray Spectrum of GRO J1655-40 Taken During the 2005 Outburst. *ApJ*, 701(2):865–884, August 2009. doi: 10.1088/0004-637X/701/2/865.

E. Kara, J. F. Steiner, A. C. Fabian, E. M. Cackett, P. Uttley, R. A. Remillard, K. C. Gendreau, Z. Arzoumanian, D. Altamirano, S. Eikenberry, T. Enoto, J. Homan, J. Neilsen, and A. L. Stevens. The corona contracts in a black-hole transient. *Nature*, 565(7738):198–201, January 2019. doi: 10.1038/s41586-018-0803-x.

A. R. King and H. Ritter. The light curves of soft X-ray transients. *MNRAS*, 293 (1):L42–L48, January 1998. doi: 10.1046/j.1365-8711.1998.01295.x.

M. Klein-Wolt and M. van der Klis. Identification of Black Hole Power Spectral Components across All Canonical States. *ApJ*, 675(2):1407–1423, March 2008. doi: 10.1086/525843.

Ole König, Guglielmo Mastroserio, Thomas Dauser, Mariano Méndez, Jingyi Wang, Javier A. García, James F. Steiner, Katja Pottschmidt, Ralf Ballhausen,

Riley M. Connors, Federico García, Victoria Grinberg, David Horn, Adam Ingram, Erin Kara, Timothy R. Kallman, Matteo Lucchini, Edward Nathan, Michael A. Nowak, Philipp Thalhammer, Michiel van der Klis, and Jörn Wilms. Long term variability of Cygnus X-1. VIII. A spectral-timing look at low energies with NICER. *arXiv e-prints*, art. arXiv:2405.07754, May 2024. doi: 10.48550/arXiv.2405.07754.

John Kormendy and Douglas Richstone. Inward Bound—The Search For Supermassive Black Holes In Galactic Nuclei. *AnnRevA&A*, 33:581, January 1995. doi: 10.1146/annurev.aa.33.090195.003053.

O. Kotov, E. Churazov, and M. Gilfanov. On the X-ray time-lags in the black hole candidates. *MNRAS*, 327(3):799–807, November 2001. doi: 10.1046/j.1365-8711.2001.04769.x.

Henric Krawczynski, Fabio Muleri, Michal Dovčiak, Alexandra Veledina, Nicole Rodriguez Cavero, Jiri Svoboda, Adam Ingram, Giorgio Matt, Javier A. Garcia, Vladislav Loktev, Michela Negro, Juri Poutanen, Takao Kitaguchi, Jakub Podgorný, John Rankin, Wenda Zhang, Andrei Berdyugin, Svetlana V. Berdyugina, Stefano Bianchi, Dmitry Blinov, Fiamma Capitanio, Niccolò Di Lalla, Paul Draghis, Sergio Fabiani, Masato Kagitani, Vadim Kravtsov, Sebastian Kiehlmann, Luca Latronico, Alexander A. Lutovinov, Nikos Mandarakas, Frédéric Marin, Andrea Marinucci, Jon M. Miller, Tsunefumi Mizuno, Sergey V. Molkov, Nicola Omodei, Pierre-Olivier Petrucci, Ajay Ratheesh, Takeshi Sakanoi, Andrei N. Semena, Raphael Skalidis, Paolo Soffitta, Allyn F. Tennant, Phillipp Thalhammer, Francesco Tombesi, Martin C. Weisskopf, Joern Wilms, Sixuan Zhang, Iván Agudo, Lucio A. Antonelli, Matteo Bachetti, Luca Baldini, Wayne H. Baumgartner, Ronaldo Bellazzini, Stephen D. Bongiorno, Raffaella Bonino, Alessandro Brez, Niccolò Bucciantini, Simone Castellano, Elisabetta Cavazzuti, Stefano Ciprini, Enrico Costa, Alessandra De Rosa, Ettore Del Monte, Laura Di Gesu, Alessandro Di Marco, Immacolata Donnarumma, Victor Doroshenko, Steven R. Ehlert, Teruaki Enoto, Yuri Evangelista, Riccardo Ferrazzoli, Shuichi Gunji, Kiyoshi Hayashida, Jeremy Heyl, Wataru Iwakiri, Svetlana G. Jorstad, Vladimir Karas, Jeffery J. Kolodziejczak, Fabio La Monaca, Ioannis Liodakis, Simone Maldera, Alberto Manfreda, Alan P. Marscher, Herman L. Marshall, Ikuyuki Mitsuishi, Chi-Yung Ng, Stephen L. O'Dell, Chiara Oppedisano, Alessandro Papitto, George G. Pavlov, Abel L. Peirson, Matteo Perri, Melissa Pesce-Rollins, Maura Pilia, Andrea Possenti, Simonetta Puccetti, Brian D. Ramsey, Roger W. Romani, Carmelo Sgrò, Patrick Slane, Gloria Spandre, Toru Tamagawa, Fabrizio Tavecchio, Roberto Taverna, Yuzuru Tawara, Nicholas E. Thomas, Alessio Trois, Sergey Tsygankov, Roberto Turolla, Jacco Vink, Kinwah Wu, Fei Xie, and Silvia Zane. Polarized x-rays constrain

the disk-jet geometry in the black hole x-ray binary Cygnus X-1. *Science*, 378 (6620):650–654, November 2022. doi: 10.1126/science.add5399.

Yair Krongold, Fabrizio Nicastro, Martin Elvis, Nancy Brickhouse, Luc Binette, Smita Mathur, and Elena Jiménez-Bailón. The Compact, Conical, Accretion-Disk Warm Absorber of the Seyfert 1 Galaxy NGC 4051 and Its Implications for IGM-Galaxy Feedback Processes. *ApJ*, 659(2):1022–1039, April 2007. doi: 10.1086/512476.

Aya Kubota, Kazuo Makishima, and Ken Ebisawa. Observational Evidence for Strong Disk Comptonization in GRO J1655-40. *ApJL*, 560(2):L147–L150, October 2001. doi: 10.1086/324377.

Ankur Kushwaha, V. K. Agrawal, and Anuj Nandi. AstroSat and MAXI view of Cygnus X-1: Signature of an 'extreme' soft nature. *MNRAS*, 507(2):2602–2613, October 2021. doi: 10.1093/mnras/stab2258.

Henny J. G. L. M. Lamers and Joseph P. Cassinelli. *Introduction to Stellar Winds*. 1999.

Pierre Simon Laplace. Beweis des Satzes, dass die anziehende Kraft bey einem Weltkörper so groß seyn könne, dass das Licht davon nicht ausströmen kann. *Allgemeine Geographische Ephemeriden*, 4(1):1–6, July 1799.

Jean-Pierre Lasota. The disc instability model of dwarf novae and low-mass X-ray binary transients. *New Astron. Rev.*, 45(7):449–508, June 2001. doi: 10.1016/S1387-6473(01)00112-9.

Fuk Kwok Li and G. W. Clark. Observation of an absorption dip in the X-ray intensity of Cygnus X-1. *ApJL*, 191:L27–L29, July 1974. doi: 10.1086/181538.

Zhixing Ling, Shuang Nan Zhang, Jingen Xiang, and Shichao Tang. A Study of the X-Ray Dust Scattering Halo of Cyg X-1 with a Cross-Correlation Method. *ApJ*, 690(1):224–230, January 2009. doi: 10.1088/0004-637X/690/1/224.

Q. Z. Liu, J. van Paradijs, and E. P. J. van den Heuvel. VizieR Online Data Catalog: Catalogue of Galactic high-mass X-ray binaries (Liu+, 2006). VizieR On-line Data Catalog: J/A+A/455/1165. Originally published in: 2006A&A...455.1165L, May 2006.

Q. Z. Liu, J. van Paradijs, and E. P. J. van den Heuvel. A catalogue of low-mass X-ray binaries in the Galaxy, LMC, and SMC (Fourth edition). *A&A*, 469(2):807–810, July 2007. doi: 10.1051/0004-6361:20077303.

M. Lomaeva, V. Grinberg, M. Guainazzi, N. Hell, S. Bianchi, M. Bissinger né Kühnel, F. Fürst, P. Kretschmar, M. Martínez-Chicharro, S. Martínez-Núñez, and J. M. Torrejón. High-resolution X-ray spectroscopy of the stellar wind in Vela X-1 during a flare. *A&A*, 641:A144, September 2020. doi: 10.1051/0004-6361/202037807.

L. B. Lucy and P. M. Solomon. Mass Loss by Hot Stars. *ApJ*, 159:879, March 1970. doi: 10.1086/150365.

Y. E. Lyubarskii. On the electric current distribution in Poynting-dominated outflows. *MNRAS*, 285(3):604–606, March 1997. doi: 10.1093/mnras/285.3.604.

Yoshitomo Maeda, Katsuji Koyama, Masaaki Sakano, Toshiaki Takeshima, and Shigeo Yamauchi. A New Eclipsing X-Ray Burster near the Galactic Center: A Quiescent State of the Old Transient A1742-289. *pasj*, 48:417–423, June 1996. doi: 10.1093/pasj/48.3.417.

Ra'ad D. Mahmoud and Chris Done. Modelling the energy dependence of black hole binary flows. *MNRAS*, 473(2):2084–2097, January 2018a. doi: 10.1093/mnras/stx2359.

Ra'ad D. Mahmoud and Chris Done. A physical model for the spectral-timing properties of accreting black holes. *MNRAS*, 480(3):4040–4059, November 2018b. doi: 10.1093/mnras/sty2133.

K. Makishima. Iron Lines from Galactic and Extragalactic X-ray Sources. In Keith O. Mason, Michael G. Watson, and Nicolas E. White, editors, *The Physics of Accretion onto Compact Objects*, volume 266, page 249. 1986. doi: 10.1007/3-540-17195-9_14.

I. Martí-Vidal. Observing black holes with mm-VLBI and the EHT. In M. Manteiga, L. Bellot, P. Benavidez, A. de Lorenzo-Cáceres, M. A. Fuente, M. J. Martínez, M. Vázquez Acosta, and C. Dafonte, editors, *Highlights on Spanish Astrophysics XI*, page 24, May 2023.

Silvia Martínez-Núñez, Peter Kretschmar, Enrico Bozzo, Lidia M. Oskinova, Joachim Puls, Lara Sidoli, Jon Olof Sundqvist, Pere Blay, Maurizio Falanga, Felix Fürst, Angel Gímenez-García, Ingo Kreykenbohm, Matthias Kühnel, Andreas Sander, José Miguel Torrejón, and Jörn Wilms. Towards a Unified View of Inhomogeneous Stellar Winds in Isolated Supergiant Stars and Supergiant High Mass X-Ray Binaries. *ssr*, 212(1-2):59–150, October 2017. doi: 10.1007/s11214-017-0340-1.

Guglielmo Mastroserio, Adam Ingram, Jingyi Wang, Javier A. García, Michiel van der Klis, Yuri Cavecchi, Riley Connors, Thomas Dauser, Fiona Harrison, Erin Kara, Ole König, and Matteo Lucchini. Modelling correlated variability in accreting black holes: the effect of high density and variable ionization on reverberation lags. *MNRAS*, 507(1):55–73, October 2021. doi: 10.1093/mnras/stab2056.

G. Matt. General Relativity effects and line emission. *Astronomische Nachrichten*, 327(10):949, December 2006. doi: 10.1002/asna.200610670.

M. L. McConnell, J. M. Ryan, W. Collmar, V. Schönfelder, H. Steinle, A. W. Strong, H. Bloemen, W. Hermsen, L. Kuiper, K. Bennett, B. F. Phlips, and J. C. Ling. A High-Sensitivity Measurement of the MeV Gamma-Ray Spectrum of Cygnus X-1. *ApJ*, 543(2):928–937, November 2000. doi: 10.1086/317128.

M. L. McConnell, A. A. Zdziarski, K. Bennett, H. Bloemen, W. Collmar, W. Hermsen, L. Kuiper, W. Paciesas, B. F. Phlips, J. Poutanen, J. M. Ryan, V. Schönfelder, H. Steinle, and A. W. Strong. The Soft Gamma-Ray Spectral Variability of Cygnus X-1. *ApJ*, 572(2):984–995, June 2002. doi: 10.1086/340436.

F. Meyer and E. Meyer-Hofmeister. On the elusive cause of cataclysmic variable outbursts. *A&A*, 104:L10–L12, January 1981.

John Michell. On the Means of Discovering the Distance, Magnitude, &c. of the Fixed Stars, in Consequence of the Diminution of the Velocity of Their Light, in Case Such a Diminution Should be Found to Take Place in any of Them, and Such Other Data Should be Procured from Observations, as Would be Farther Necessary for That Purpose. By the Rev. John Michell, B. D. F. R. S. In a Letter to Henry Cavendish, Esq. F. R. S. and A. S. *Philosophical Transactions of the Royal Society of London Series I*, 74:35–57, January 1784.

J. M. Miller, A. C. Fabian, R. Wijnands, R. A. Remillard, P. Wojdowski, N. S. Schulz, T. Di Matteo, H. L. Marshall, C. R. Canizares, D. Pooley, and W. H. G. Lewin. Resolving the Composite Fe K$\alpha$ Emission Line in the Galactic Black Hole Cygnus X-1 with Chandra. *ApJ*, 578(1):348–356, October 2002. doi: 10.1086/342466.

James C. A. Miller-Jones, Arash Bahramian, Jerome A. Orosz, Ilya Mandel, Lijun Gou, Thomas J. Maccarone, Coenraad J. Neijssel, Xueshan Zhao, Janusz Ziółkowski, Mark J. Reid, Phil Uttley, Xueying Zheng, Do-Young Byun, Richard Dodson, Victoria Grinberg, Taehyun Jung, Jeong-Sook Kim, Benito Marcote, Sera Markoff, María J. Rioja, Anthony P. Rushton, David M. Russell, Gregory R. Sivakoff, Alexandra J. Tetarenko, Valeriu Tudose, and Joern Wilms. Cygnus X-1 contains a 21-solar mass black hole—Implications

for massive star winds. *Science*, 371(6533):1046–1049, March 2021. doi: 10.1126/science.abb3363.

Ivica Miškovičová, Natalie Hell, Manfred Hanke, Michael A. Nowak, Katja Pottschmidt, Norbert S. Schulz, Victoria Grinberg, Refiz Duro, Oliwia K. Madej, Anne M. Lohfink, Jérôme Rodriguez, Marion Cadolle Bel, Arash Bodaghee, John A. Tomsick, Julia C. Lee, Gregory V. Brown, and Jörn Wilms. Chandra X-ray spectroscopy of focused wind in the Cygnus X-1 system. II. The non-dip spectrum in the low/hard state - modulations with orbital phase. *A&A*, 590: A114, May 2016. doi: 10.1051/0004-6361/201322490.

S. Miyamoto, M. Fujii, M. Matsuoka, J. Nishimura, M. Oda, Y. Ogawara, S. Ohta, and M. Wada. Measurement of the Location of the X-Ray Source Cygnus X-1. *ApJL*, 168:L11, August 1971. doi: 10.1086/180774.

S. Motta, T. Belloni, and J. Homan. The evolution of the high-energy cut-off in the X-ray spectrum of GX 339-4 across a hard-to-soft transition. *MNRAS*, 400 (3):1603–1612, December 2009. doi: 10.1111/j.1365-2966.2009.15566.x.

S. Motta, T. Muñoz-Darias, P. Casella, T. Belloni, and J. Homan. Low-frequency oscillations in black holes: a spectral-timing approach to the case of GX 339-4. *MNRAS*, 418(4):2292–2307, December 2011. doi: 10.1111/j.1365-2966.2011.19566.x.

S. E. Motta, P. Casella, M. Henze, T. Muñoz-Darias, A. Sanna, R. Fender, and T. Belloni. Geometrical constraints on the origin of timing signals from black holes. *MNRAS*, 447(2):2059–2072, February 2015. doi: 10.1093/mnras/stu2579.

T. Muñoz-Darias, S. Motta, and T. M. Belloni. Fast variability as a tracer of accretion regimes in black hole transients. *MNRAS*, 410(1):679–684, January 2011. doi: 10.1111/j.1365-2966.2010.17476.x.

Paul Murdin and B. Louise Webster. Optical Identification of Cygnus X-1. *Nature*, 233(5315):110, September 1971. doi: 10.1038/233110a0.

Alexander A. Mushtukov, Adam Ingram, and Michiel van der Klis. Propagating mass accretion rate fluctuations in X-ray binaries under the influence of viscous diffusion. *MNRAS*, 474(2):2259–2276, February 2018. doi: 10.1093/mnras/stx2872.

Coenraad J. Neijssel, Serena Vinciguerra, Alejandro Vigna-Gómez, Ryosuke Hirai, James C. A. Miller-Jones, Arash Bahramian, Thomas J. Maccarone, and Ilya Mandel. Wind Mass-loss Rates of Stripped Stars Inferred from Cygnus X-1. *ApJ*, 908(2):118, February 2021. doi: 10.3847/1538-4357/abde4a.

Marvin Neumann, Artur Avakyan, Victor Doroshenko, and Andrea Santangelo. XRBcats: Galactic High Mass X-ray Binary Catalogue. *arXiv e-prints*, art. arXiv:2303.16137, March 2023. doi: 10.48550/arXiv.2303.16137.

C. Ng, M. Díaz Trigo, M. Cadolle Bel, and S. Migliari. A systematic analysis of the broad iron K$\alpha$ line in neutron-star LMXBs with XMM-Newton. *A&A*, 522: A96, November 2010. doi: 10.1051/0004-6361/200913575.

Fabrizio Nicastro, Fabrizio Fiore, G. Cesare Perola, and Martin Elvis. Ionized Absorbers in Active Galactic Nuclei: The Role of Collisional Ionization and Time-evolving Photoionization. *ApJ*, 512(1):184–196, February 1999. doi: 10.1086/306736.

M. S. Noble and M. A. Nowak. Beyond XSPEC: Toward Highly Configurable Astrophysical Analysis. *pasp*, 120(869):821, July 2008. doi: 10.1086/590324.

M. A. Nowak. Are there three peaks in the power spectra of GX 339-4 and Cyg X-1? *MNRAS*, 318(2):361–367, October 2000. doi: 10.1046/j.1365-8711.2000.03668.x.

Michael A. Nowak, Brian A. Vaughan, Jörn Wilms, James B. Dove, and Mitchell C. Begelman. Rossi X-Ray Timing Explorer Observation of Cygnus X-1. II. Timing Analysis. *ApJ*, 510(2):874–891, January 1999. doi: 10.1086/306610.

Michael A. Nowak, Manfred Hanke, Sarah N. Trowbridge, Sera B. Markoff, Jörn Wilms, Katja Pottschmidt, Paolo Coppi, Dipankar Maitra, John E. Davis, and Frank Tramper. Corona, Jet, and Relativistic Line Models for Suzaku/RXTE/Chandra-HETG Observations of the Cygnus X-1 Hard State. *ApJ*, 728(1):13, February 2011. doi: 10.1088/0004-637X/728/1/13.

M. Oda. CygX-1/A candidate of the black hole. *ssr*, 20(6):757–813, November 1977. doi: 10.1007/BF02431835.

J. R. Oppenheimer and G. M. Volkoff. On Massive Neutron Cores. *Physical Review*, 55(4):374–381, February 1939. doi: 10.1103/PhysRev.55.374.

Jerome A. Orosz, Jeffrey E. McClintock, Ramesh Narayan, Charles D. Bailyn, Joel D. Hartman, Lucas Macri, Jiefeng Liu, Wolfgang Pietsch, Ronald A. Remillard, Avi Shporer, and Tsevi Mazeh. A 15.65-solar-mass black hole in an eclipsing binary in the nearby spiral galaxy M 33. *Nature*, 449(7164):872–875, October 2007. doi: 10.1038/nature06218.

L. M. Oskinova, A. Feldmeier, and P. Kretschmar. Clumped stellar winds in supergiant high-mass X-ray binaries: X-ray variability and photoionization. *MNRAS*, 421(4):2820–2831, April 2012. doi: 10.1111/j.1365-2966.2012.20507.x.

Stanley P. Owocki, John I. Castor, and George B. Rybicki. Time-dependent Models of Radiatively Driven Stellar Winds. I. Nonlinear Evolution of Instabilities for a Pure Absorption Model. *ApJ*, 335:914, December 1988. doi: 10.1086/166977.

B. Paczynski. Common Envelope Binaries. In Peter Eggleton, Simon Mitton, and John Whelan, editors, *Structure and Evolution of Close Binary Systems*, volume 73, page 75, January 1976.

Ishika Palit, Agnieszka Janiuk, and Bozena Czerny. Clumpy Wind Accretion in Cygnus X-1. *ApJ*, 904(1):21, November 2020. doi: 10.3847/1538-4357/abba1b.

K. Pottschmidt, J. Wilms, M. A. Nowak, W. A. Heindl, D. M. Smith, and R. Staubert. Temporal evolution of X-ray lags in Cygnus X-1. *A&A*, 357: L17–L20, May 2000. doi: 10.48550/arXiv.astro-ph/0004018.

K. Pottschmidt, J. Wilms, M. A. Nowak, G. G. Pooley, T. Gleissner, W. A. Heindl, D. M. Smith, R. Remillard, and R. Staubert. Long term variability of Cygnus X-1. I. X-ray spectral-temporal correlations in the hard state. *A&A*, 407:1039–1058, September 2003. doi: 10.1051/0004-6361:20030906.

Juri Poutanen, Julian H. Krolik, and Felix Ryde. The nature of spectral transitions in accreting black holes: the case of CYG X-1. *MNRAS*, 292(1):L21–L25, November 1997. doi: 10.1093/mnras/292.1.L21.

Juri Poutanen, Andrzej A. Zdziarski, and Askar Ibragimov. Superorbital variability of X-ray and radio emission of Cyg X-1 - II. Dependence of the orbital modulation and spectral hardness on the superorbital phase. *MNRAS*, 389(3): 1427–1438, September 2008. doi: 10.1111/j.1365-2966.2008.13666.x.

Juri Poutanen, Alexandra Veledina, and Andrzej A. Zdziarski. Doughnut strikes sandwich: the geometry of hot medium in accreting black hole X-ray binaries. *A&A*, 614:A79, June 2018. doi: 10.1051/0004-6361/201732345.

Juri Poutanen, Alexandra Veledina, and Andrei M. Beloborodov. Polarized X-rays from windy accretion in Cygnus X-1. *arXiv e-prints*, art. arXiv:2302.11674, February 2023. doi: 10.48550/arXiv.2302.11674.

P. Predehl and J. H. M. M. Schmitt. X-raying the interstellar medium: ROSAT observations of dust scattering halos. *A&A*, 500:459–475, January 1995.

Dimitrios Psaltis, Tomaso Belloni, and Michiel van der Klis. Correlations in Quasi-periodic Oscillation and Noise Frequencies among Neutron Star and Black Hole X-Ray Binaries. *ApJ*, 520(1):262–270, July 1999. doi: 10.1086/307436.

Joachim Puls, Jorick S. Vink, and Francisco Najarro. Mass loss from hot massive stars. *A&ARv*, 16(3-4):209–325, December 2008. doi: 10.1007/s00159-008-0015-8.

S. Rappaport, W. Zaumen, and R. Doxsey. On the Location of Cygnus X-1. *ApJL*, 168:L17, August 1971. doi: 10.1086/180776.

Pablo Reig. Be/X-ray binaries. *Ap&SS*, 332(1):1–29, March 2011. doi: 10.1007/s10509-010-0575-8.

H. Ritter and U. Kolb. Catalogue of cataclysmic binaries, low-mass X-ray binaries and related objects (Seventh edition). *A&A*, 404:301–303, June 2003. doi: 10.1051/0004-6361:20030330.

R. R. Ross and A. C. Fabian. A comprehensive range of X-ray ionized-reflection models. *MNRAS*, 358(1):211–216, March 2005. doi: 10.1111/j.1365-2966.2005.08797.x.

M. M. Rubio-Díez, J. O. Sundqvist, F. Najarro, A. Traficante, J. Puls, L. Calzoletti, and D. Figer. Upper mass-loss limits and clumping in the intermediate and outer wind regions of OB stars. *A&A*, 658:A61, February 2022. doi: 10.1051/0004-6361/202040116.

David M. Russell, Ahlam Al Qasim, Federico Bernardini, Richard M. Plotkin, Fraser Lewis, Karri I. I. Koljonen, and Yi-Jung Yang. Optical Precursors to Black Hole X-Ray Binary Outbursts: An Evolving Synchrotron Jet Spectrum in Swift J1357.2-0933. *ApJ*, 852(2):90, January 2018. doi: 10.3847/1538-4357/aa9d8c.

G. Sala, J. Greiner, J. Vink, F. Haberl, E. Kendziorra, and X. L. Zhang. The highly ionized disk wind of <ASTROBJ>GRO J1655-40</ASTROBJ>. *A&A*, 461(3):1049–1056, January 2007. doi: 10.1051/0004-6361:20065168.

M. I. Saladino, O. R. Pols, E. van der Helm, I. Pelupessy, and S. Portegies Zwart. Gone with the wind: the impact of wind mass transfer on the orbital evolution of AGB binary systems. *A&A*, 618:A50, October 2018. doi: 10.1051/0004-6361/201832967.

S. Scaringi, E. Körding, P. Uttley, C. Knigge, P. J. Groot, and M. Still. The universal nature of accretion-induced variability: the rms-flux relation in an accreting white dwarf. *MNRAS*, 421(4):2854–2860, April 2012. doi: 10.1111/j.1365-2966.2012.20512.x.

Karl Schwarzschild. Über das Gravitationsfeld eines Massenpunktes nach der Einsteinschen Theorie. *Sitzungsberichte der Königlich Preussischen Akademie der Wissenschaften*, pages 189–196, January 1916.

N. I. Shakura and R. A. Sunyaev. Black holes in binary systems. Observational appearance. *A&A*, 24:337–355, January 1973.

C. V. Silva, P. Uttley, and E. Costantini. Timing the warm absorber in NGC 4051. *A&A*, 596:A79, December 2016. doi: 10.1051/0004-6361/201628555.

Chris J. Skipper, Ian M. McHardy, and Thomas J. Maccarone. Very fast X-ray spectral variability in Cygnus X-1: origin of the hard- and soft-state emission components. *MNRAS*, 434(1):574–584, September 2013. doi: 10.1093/mnras/stt1044.

G. J. Sobczak, R. A. Remillard, M. Muno, and J. McClintock. Creating Order Out of Chaos-Characterizing the QPO behavior of the X-ray Nova XTE J1550-564. In T. E. Strohmayer, editor, *Rossi2000: Astrophysics with the Rossi X-ray Timing Explorer*, page 18, January 2000.

A. M. Stirling, R. E. Spencer, C. J. de la Force, M. A. Garrett, R. P. Fender, and R. N. Ogley. A relativistic jet from Cygnus X-1 in the low/hard X-ray state. *MNRAS*, 327(4):1273–1278, November 2001. doi: 10.1046/j.1365-8711.2001.04821.x.

L. Strüder, U. Briel, K. Dennerl, R. Hartmann, E. Kendziorra, N. Meidinger, E. Pfeffermann, C. Reppin, B. Aschenbach, W. Bornemann, H. Bräuninger, W. Burkert, M. Elender, M. Freyberg, F. Haberl, G. Hartner, F. Heuschmann, H. Hippmann, E. Kastelic, S. Kemmer, G. Kettenring, W. Kink, N. Krause, S. Müller, A. Oppitz, W. Pietsch, M. Popp, P. Predehl, A. Read, K. H. Stephan, D. Stötter, J. Trümper, P. Holl, J. Kemmer, H. Soltau, R. Stötter, U. Weber, U. Weichert, C. von Zanthier, D. Carathanassis, G. Lutz, R. H. Richter, P. Solc, H. Böttcher, M. Kuster, R. Staubert, A. Abbey, A. Holland, M. Turner, M. Balasini, G. F. Bignami, N. La Palombara, G. Villa, W. Buttler, F. Gianini, R. Lainé, D. Lumb, and P. Dhez. The European Photon Imaging Camera on XMM-Newton: The pn-CCD camera. *A&A*, 365:L18–L26, January 2001. doi: 10.1051/0004-6361:20000066.

J. O. Sundqvist and J. Puls. Atmospheric NLTE models for the spectroscopic analysis of blue stars with winds. IV. Porosity in physical and velocity space. *A&A*, 619:A59, November 2018. doi: 10.1051/0004-6361/201832993.

J. O. Sundqvist, S. P. Owocki, and J. Puls. 2D wind clumping in hot, massive stars from hydrodynamical line-driven instability simulations using a pseudo-planar approach. *A&A*, 611:A17, March 2018. doi: 10.1051/0004-6361/201731718.

Jon O. Sundqvist and Stanley P. Owocki. Clumping in the inner winds of hot, massive stars from hydrodynamical line-driven instability simulations. *MNRAS*, 428(2):1837–1844, January 2013. doi: 10.1093/mnras/sts165.

R. A. Sunyaev and L. G. Titarchuk. Comptonization of X-Rays in Plasma Clouds - Typical Radiation Spectra. *A&A*, 86:121, June 1980.

R. A. Sunyaev and J. Truemper. Hard X-ray spectrum of CYG X-1. *Nature*, 279: 506–508, June 1979. doi: 10.1038/279506a0.

H. Tananbaum, E. Kellogg, H. Gursky, S. Murray, E. Schreier, and R. Giacconi. Measurement of the Location of the X-Ray Sources Cygnus X-1 and Cygnus X-2 from UHURU. *ApJL*, 165:L37, April 1971. doi: 10.1086/180712.

H. Tananbaum, H. Gursky, E. Kellogg, R. Giacconi, and C. Jones. Observation of a Correlated X-Ray Transition in Cygnus X-1. *ApJL*, 177:L5, October 1972. doi: 10.1086/181042.

C. Bruce Tarter, Wallace H. Tucker, and Edwin E. Salpeter. The Interaction of X-Ray Sources with Optically Thin Environments. *ApJ*, 156:943, June 1969. doi: 10.1086/150026.

T. M. Tauris and E. P. J. van den Heuvel. Formation and evolution of compact stellar X-ray sources. In *Compact stellar X-ray sources*, volume 39, pages 623–665. 2006. doi: 10.48550/arXiv.astro-ph/0303456.

B. E. Tetarenko, G. R. Sivakoff, C. O. Heinke, and J. C. Gladstone. WATCHDOG: A Comprehensive All-sky Database of Galactic Black Hole X-ray Binaries. *ApJSupp*, 222(2):15, February 2016. doi: 10.3847/0067-0049/222/2/15.

Kip S. Thorne. Disk-Accretion onto a Black Hole. II. Evolution of the Hole. *ApJ*, 191:507–520, July 1974. doi: 10.1086/152991.

Richard C. Tolman. Static Solutions of Einstein's Field Equations for Spheres of Fluid. *Physical Review*, 55(4):364–373, February 1939. doi: 10.1103/PhysRev.55.364.

John A. Tomsick, Michael A. Nowak, Michael Parker, Jon M. Miller, Andy C. Fabian, Fiona A. Harrison, Matteo Bachetti, Didier Barret, Steven E. Boggs, Finn E. Christensen, William W. Craig, Karl Forster, Felix Fürst, Brian W.

Grefenstette, Charles J. Hailey, Ashley L. King, Kristin K. Madsen, Lorenzo Natalucci, Katja Pottschmidt, Randy R. Ross, Daniel Stern, Dominic J. Walton, Jörn Wilms, and William W. Zhang. The Reflection Component from Cygnus X-1 in the Soft State Measured by NuSTAR and Suzaku. *ApJ*, 780(1):78, January 2014. doi: 10.1088/0004-637X/780/1/78.

John A. Tomsick, Michael L. Parker, Javier A. García, Kazutaka Yamaoka, Didier Barret, Jeng-Lun Chiu, Maïca Clavel, Andrew Fabian, Felix Fürst, Poshak Gandhi, Victoria Grinberg, Jon M. Miller, Katja Pottschmidt, and Dominic J. Walton. Alternative Explanations for Extreme Supersolar Iron Abundances Inferred from the Energy Spectrum of Cygnus X-1. *ApJ*, 855(1):3, March 2018. doi: 10.3847/1538-4357/aaaab1.

P. Uttley. A deep stare into the abyss: spectral-timing an entire binary orbit of Cygnus X-1. In Jan-Uwe Ness and Simone Migliari, editors, *The X-ray Universe 2017*, page 230, October 2017.

P. Uttley, I. M. McHardy, and S. Vaughan. Non-linear X-ray variability in X-ray binaries and active galaxies. *MNRAS*, 359(1):345–362, May 2005. doi: 10.1111/j.1365-2966.2005.08886.x.

P. Uttley, T. Wilkinson, P. Cassatella, J. Wilms, K. Pottschmidt, M. Hanke, and M. Böck. The causal connection between disc and power-law variability in hard state black hole X-ray binaries. *MNRAS*, 414(1):L60–L64, June 2011. doi: 10.1111/j.1745-3933.2011.01056.x.

P. Uttley, E. M. Cackett, A. C. Fabian, E. Kara, and D. R. Wilkins. X-ray reverberation around accreting black holes. *A&ARv*, 22:72, August 2014. doi: 10.1007/s00159-014-0072-0.

M. van der Klis. Fourier techniques in X-ray timing. In H. Ögelman and E. P. J. van den Heuvel, editors, *Timing Neutron Stars*, volume 262 of *NATO Advanced Study Institute (ASI) Series C*, page 27, January 1989. doi: 10.1007/978-94-009-2273-0_3.

Stéfan van der Walt, S. Chris Colbert, and Gaël Varoquaux. The NumPy Array: A Structure for Efficient Numerical Computation. *Computing in Science and Engineering*, 13(2):22–30, March 2011. doi: 10.1109/MCSE.2011.37.

Brian A. Vaughan and Michael A. Nowak. X-Ray Variability Coherence: How to Compute It, What It Means, and How It Constrains Models of GX 339-4 and Cygnus X-1. *ApJL*, 474(1):L43–L46, January 1997. doi: 10.1086/310430.

S. Vaughan, R. Edelson, R. S. Warwick, and P. Uttley. On characterizing the variability properties of X-ray light curves from active galaxies. *MNRAS*, 345 (4):1271–1284, November 2003. doi: 10.1046/j.1365-2966.2003.07042.x.

Alexandra Veledina, Juri Poutanen, and Indrek Vurm. Hot accretion flow in black hole binaries: a link connecting X-rays to the infrared. *MNRAS*, 430(4):3196–3212, April 2013. doi: 10.1093/mnras/stt124.

D. A. Verner, G. J. Ferland, K. T. Korista, and D. G. Yakovlev. Atomic Data for Astrophysics. II. New Analytic FITS for Photoionization Cross Sections of Atoms and Ions. *ApJ*, 465:487, July 1996. doi: 10.1086/177435.

Pauli Virtanen, Ralf Gommers, Travis E. Oliphant, Matt Haberland, Tyler Reddy, David Cournapeau, Evgeni Burovski, Pearu Peterson, Warren Weckesser, Jonathan Bright, Stéfan J. van der Walt, Matthew Brett, Joshua Wilson, K. Jarrod Millman, Nikolay Mayorov, Andrew R. J. Nelson, Eric Jones, Robert Kern, Eric Larson, C J Carey, İlhan Polat, Yu Feng, Eric W. Moore, Jake VanderPlas, Denis Laxalde, Josef Perktold, Robert Cimrman, Ian Henriksen, E. A. Quintero, Charles R. Harris, Anne M. Archibald, Antônio H. Ribeiro, Fabian Pedregosa, Paul van Mulbregt, and SciPy 1.0 Contributors. SciPy 1.0: Fundamental Algorithms for Scientific Computing in Python. *Nature Methods*, 17:261–272, 2020. doi: 10.1038/s41592-019-0686-2.

Nolan R. Walborn. The Spectrum of HDE 226868 (=CYGNUS X-1). *ApJL*, 179: L123, February 1973. doi: 10.1086/181131.

D. J. Walton, J. A. Tomsick, K. K. Madsen, V. Grinberg, D. Barret, S. E. Boggs, F. E. Christensen, M. Clavel, W. W. Craig, A. C. Fabian, F. Fuerst, C. J. Hailey, F. A. Harrison, J. M. Miller, M. L. Parker, F. Rahoui, D. Stern, L. Tao, J. Wilms, and W. Zhang. The Soft State of Cygnus X-1 Observed with NuSTAR: A Variable Corona and a Stable Inner Disk. *ApJ*, 826(1):87, July 2016. doi: 10.3847/0004-637X/826/1/87.

Jingyi Wang, Erin Kara, James F. Steiner, Javier A. García, Jeroen Homan, Joseph Neilsen, Grégoire Marcel, Renee M. Ludlam, Francesco Tombesi, Edward M. Cackett, and Ron A. Remillard. Relativistic Reflection and Reverberation in GX 339-4 with NICER and NuSTAR. *ApJ*, 899(1):44, August 2020. doi: 10.3847/1538-4357/ab9ec3.

Grzegorz Wardziński, Andrzej A. Zdziarski, Marek Gierliński, J. Eric Grove, Keith Jahoda, and W. Neil Johnson. X-ray and $\gamma$-ray spectra and variability of the black hole candidate GX 339-4. *MNRAS*, 337(3):829–839, December 2002. doi: 10.1046/j.1365-8711.2002.05914.x.

Rudy Wijnands and Michiel van der Klis. The Broadband Power Spectra of X-Ray Binaries. *ApJ*, 514(2):939–944, April 1999. doi: 10.1086/306993.

Rudy Wijnands, Jeroen Homan, and Michiel van der Klis. The Complex Phase-Lag Behavior of the 3-12 HZ Quasi-Periodic Oscillations during the Very High State of XTE J1550-564. *ApJL*, 526(1):L33–L36, November 1999. doi: 10.1086/312365.

Tony Wilkinson and Philip Uttley. Accretion disc variability in the hard state of black hole X-ray binaries. *MNRAS*, 397(2):666–676, August 2009. doi: 10.1111/j.1365-2966.2009.15008.x.

J. Wilms, A. Allen, and R. McCray. On the Absorption of X-Rays in the Interstellar Medium. *ApJ*, 542(2):914–924, October 2000. doi: 10.1086/317016.

J. Wilms, M. A. Nowak, K. Pottschmidt, G. G. Pooley, and S. Fritz. Long term variability of Cygnus X-1. IV. Spectral evolution 1999-2004. *A&A*, 447(1):245–261, February 2006. doi: 10.1051/0004-6361:20053938.

Jingen Xiang, Julia C. Lee, Michael A. Nowak, and Jörn Wilms. Using the X-Ray Dust Scattering Halo of Cygnus X-1 to Determine Distance and Dust Distributions. *ApJ*, 738(1):78, September 2011. doi: 10.1088/0004-637X/738/1/78.

R. Zanin, A. Fernández-Barral, E. de Oña Wilhelmi, F. Aharonian, O. Blanch, V. Bosch-Ramon, and D. Galindo. Gamma rays detected from Cygnus X-1 with likely jet origin. *A&A*, 596:A55, November 2016. doi: 10.1051/0004-6361/201628917.

A. A. Zdziarski. Radiative Processes and Geometry of Spectral States of Black-hole Binaries. In P. C. H. Martens, S. Tsuruta, and M. A. Weber, editors, *Highly Energetic Physical Processes and Mechanisms for Emission from Astrophysical Plasmas*, volume 195, page 153, May 2000. doi: 10.48550/arXiv.astro-ph/0001078.

A. A. Zdziarski and M. Gierliński. Radiative Processes, Spectral States and Variability of Black-Hole Binaries. *Progress of Theoretical Physics Supplement*, 155:99–119, January 2004. doi: 10.1143/PTPS.155.99.

A. A. Zdziarski, W. N. Johnson, and P. Magdziarz. Broad-band $\gamma$-ray and X-ray spectra of NGC 4151 and their implications for physical processes and geometry. *MNRAS*, 283(1):193–206, November 1996. doi: 10.1093/mnras/283.1.193.

Andrzej A. Zdziarski. The structure of the jet in Cyg X-1 inferred from orbital modulation of the radio emission. *MNRAS*, 422(2):1750–1760, May 2012. doi: 10.1111/j.1365-2966.2012.20754.x.

Andrzej A. Zdziarski, Juri Poutanen, Joanna Mikolajewska, Marek Gierlinski, Ken Ebisawa, and W. Neil Johnson. Broad-band X-ray/gamma-ray spectra and binary parameters of GX 339-4 and their astrophysical implications. *MNRAS*, 301(2):435–450, December 1998. doi: 10.1046/j.1365-8711.1998.02021.x.

Andrzej A. Zdziarski, J. Eric Grove, Juri Poutanen, A. R. Rao, and S. V. Vadawale. OSSE and RXTE Observations of GRS 1915+105: Evidence for Nonthermal Comptonization. *ApJL*, 554(1):L45–L48, June 2001. doi: 10.1086/320932.

Andrzej A. Zdziarski, Juri Poutanen, William S. Paciesas, and Linqing Wen. Understanding the Long-Term Spectral Variability of Cygnus X-1 with Burst and Transient Source Experiment and All-Sky Monitor Observations. *ApJ*, 578(1): 357–373, October 2002. doi: 10.1086/342402.

Andrzej A. Zdziarski, Piotr Lubiński, Marat Gilfanov, and Mike Revnivtsev. Correlations between X-ray and radio spectral properties of accreting black holes. *MNRAS*, 342(2):355–372, June 2003. doi: 10.1046/j.1365-8711.2003.06556.x.

Andrzej A. Zdziarski, Ranjeev Misra, and Marek Gierliński. Compton scattering as the explanation of the peculiar X-ray properties of Cyg X-3. *MNRAS*, 402 (2):767–775, February 2010. doi: 10.1111/j.1365-2966.2009.15942.x.

Andrzej A. Zdziarski, Guy G. Pooley, and Gerald K. Skinner. The doubling of the superorbital period of Cyg X-1. *MNRAS*, 412(3):1985–1992, April 2011. doi: 10.1111/j.1365-2966.2010.18034.x.

Andrzej A. Zdziarski, Denys Malyshev, Maria Chernyakova, and Guy G. Pooley. High-energy gamma-rays from Cyg X-1. *MNRAS*, 471(3):3657–3667, November 2017. doi: 10.1093/mnras/stx1846.

Andrzej A. Zdziarski, Swadesh Chand, Srimanta Banerjee, Michal Szanecki, Agnieszka Janiuk, Piotr Lubinski, Andrzej Niedzwiecki, Gulab Dewangan, and Ranjeev Misra. What Is the Black Hole Spin in Cyg X-1? *arXiv e-prints*, art. arXiv:2402.12325, February 2024. doi: 10.48550/arXiv.2402.12325.

S. N. Zhang, W. Cui, B. A. Harmon, W. S. Paciesas, R. E. Remillard, and J. van Paradijs. The 1996 Soft State Transition of Cygnus X-1. *ApJL*, 477(2):L95–L98, March 1997. doi: 10.1086/310530.

Xueshan Zhao, Lijun Gou, Yanting Dong, Xueying Zheng, James F. Steiner, James C. A. Miller-Jones, Arash Bahramian, Jerome A. Orosz, and Ye Feng. Reestimating the Spin Parameter of the Black Hole in Cygnus X-1. *ApJ*, 908(2): 117, February 2021. doi: 10.3847/1538-4357/abbcd6.

M. Zhou, V. Grinberg, Q. C. Bu, A. Santangelo, F. Cangemi, C. M. Diez, O. König, L. Ji, M. A. Nowak, K. Pottschmidt, J. Rodriguez, J. Wilms, S. Zhang, J. L. Qu, and S. N. Zhang. The spectral-timing analysis of Cygnus X-1 with Insight-HXMT. *A&A*, 666:A172, October 2022. doi: 10.1051/0004-6361/202244240.

Piotr T. Życki, Chris Done, and David A. Smith. The 1989 May outburst of the soft X-ray transient GS 2023+338 (V404 Cyg). *MNRAS*, 309(3):561–575, November 1999. doi: 10.1046/j.1365-8711.1999.02885.x.